AD-A089 353 NATIONAL BUREAU OF STANDARDS BOULDER CO ELECTROMAGN--ETC F/G 9/1
JOSEPHSON A/D CONVERTER DEVELOPMENT.(U)
SEP 80 C A HAMILTON, R E HARRIS, R L KAUTZ N00014-80-F-0017
UNCLASSIFIED NBSSR-724-21-80 NL

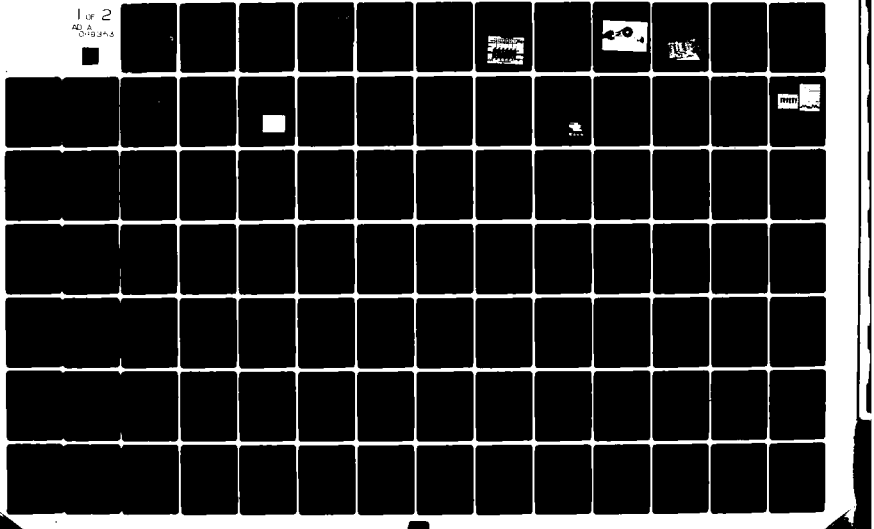

LEVEL II

12

AD A089353

DTIC
ELECTE
SEP 22 1980
S D
C

DDC FILE COPY

80 9 18 048

JOSEPHSON A/D CONVERTER DEVELOPMENT
ANNUAL TECHNICAL REPORT

to

Office of Naval Research, Code 427
Arlington, VA 22217

May 1, 1979 to April 30, 1980
Contract Number N00014-80-C-0017
Contract Authority NR 383-040

JOSEPHSON A/D CONVERTER DEVELOPMENT

ANNUAL TECHNICAL REPORT
to
Office of Naval Research, Code 427
Arlington, VA 22217

May 1, 1979 to April 30, 1980
Contract Number N00014-80-0017
Contract Authority NR 383-040

by

C. A. Hamilton, R. E. Harris, R. L. Kautz,
F. L. Lloyd and R. L. Peterson
(Report prepared by R. E. Harris and C. A. Hamilton)

Submitted by:

Electromagnetic Technology Division
Center for Electronics and Electrical Engineering
National Engineering Laboratory
National Bureau of Standards
Boulder, CO 80303
Cost Center No. 7240480

Report No. SR-724-21-80

June 1980

Reviewed and Approved by:

R. A. Kamper, Chief
Electromagnetic Technology Division

(14) NBSSR-724-21-80

(11) F62702

SECURITY CLASSIFICATION OF THIS PAGE (When Data Entered)

REPORT DOCUMENTATION PAGE

READ INSTRUCTIONS BEFORE COMPLETING FORM

1. REPORT NUMBER

2. GOVT ACCESSION NO. AD-A089353

3. RECIPIENT'S CATALOG NUMBER (rept.)

4. TITLE (and Subtitle) (1) (1)

JOSEPHSON A/D CONVERTER DEVELOPMENT (4)

5. TYPE OF REPORT & PERIOD COVERED

Annual Technical [redacted]
May [redacted] 1979 - [redacted] April [redacted] 1980

6. PERFORMING ORG. REPORT NUMBER

SR-724-21-80

7. AUTHOR(s) (10)

C. A. Hamilton, R. E. Harris, R. L. Kautz
F. L. Lloyd [redacted] R. L. Peterson

8. CONTRACT OR GRANT NUMBER(s) (15)

N00014-80-0017

9. PERFORMING ORGANIZATION NAME AND ADDRESS

Cryoelectronic Metrology Group
Electromagnetic Technology Division
National Bureau of Standards
Boulder, CO 80303

AREA & WORK UNIT NUMBERS (17)

PE 62762N
RF62 582 001
NR 383 040

11. CONTROLLING OFFICE NAME AND ADDRESS (11) (1)

Office of Naval Research, Code 427
Arlington, VA 22217

12. REPORT DATE

September 1980

13. NUMBER OF PAGES

97

14. MONITORING AGENCY NAME & ADDRESS (if different from Controlling Office) (12) 148

Same

15. SECURITY CLASS. (of this report)

Unclassified

15a. DECLASSIFICATION/DOWNGRADING SCHEDULE

16. DISTRIBUTION STATEMENT (of this Report)

Approved for public release, distribution unlimited.

17. DISTRIBUTION STATEMENT (of the abstract entered in Block 20, if different from Report)

18. SUPPLEMENTARY NOTES

ONR Scientific Officer
Telephone (202) 696-4218

19. KEY WORDS (Continue on reverse side if necessary and identify by block number)

A/D converter; high speed superconducting electronics;
Josephson junctions

20. ABSTRACT (Continue on reverse side if necessary and identify by block number)

This report describes the third year of an effort to demonstrate an ultra-high-speed analog-to-digital converter using superconducting electronics. A converter was fabricated and tested at a sample rate of 2×10^9 samples/second.

DD FORM 1 JAN 73 1473 EDITION OF 1 NOV 65 IS OBSOLETE
S/N 0102-LF-014-6601

Unclassified 370 211

SECURITY CLASSIFICATION OF THIS PAGE (When Data Entered)

JOSEPHSON A/D CONVERTER DEVELOPMENT

TABLE OF CONTENTS

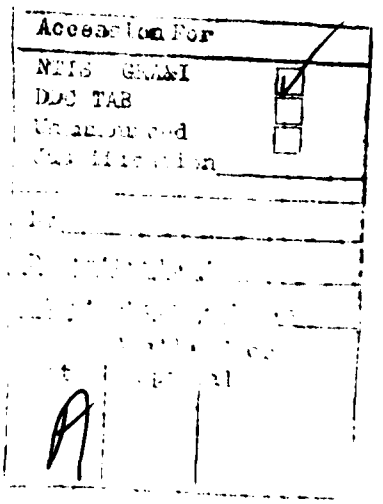

1.0 INTRODUCTION

This report describes the third year of work on Contract Number N00014-80-0017. The work has the following general goals:

> Demonstration of a superconducting 300 megasample per second A/D converter within the first three years.
>
> Demonstration of a superconducting A/D converter operating well into the gigasample per second region within five years.

During the second year the goal for the third year was completed. During the third year the goal for the fifth year was essentially accomplished and described in a publication in Electron Device Letters.

Future efforts under this contract will involve a continued effort to raise the sample rate and to accurately characterize the device at GHz sampling rates. In addition work will begin on efforts to incorporate the analog-to-digital converter into a transient event recorder. This entire device will be fabricated in superconducting integrated circuit technology.

2.0 A/D CONVERTER

2.1 2 GHz A/D Sample Rate

During the contract period the performance of the A/D converter has been improved from 4-bit accuracy at a 200 MHz sampling rate (see Appendix A1) to 6-bit accuracy at a 2 GHz sampling rate. This improvement has been made possible by a new design which allows a substantial size reduction and a new sample holder with reduced crosstalk. The new design is based on 2-junction interferometers which are smaller and have much more periodic threshold curves than the 3-junction devices used previously. The 2-junction interferometers also improve the operating margins and are less sensitive to trapped flux.

The sample holder has been modified to increase the number of contacts from 24 to 32 thus allowing a separate ground wire for each of the eight high speed contacts. The resulting reduction in crosstalk makes possible operation of the converter above 1 GHz. Even with this improvement, sample holder crosstalk is the limiting factor at the highest operating speeds. The new design and experimental results are described in detail in a publication reproduced in Appendix A2: "A Superconducting 6-Bit Analog-to-Digital Converter with Operation to 2 x 10^9 Samples/Second."

2.2 Direct Injection A/D Converter

An alternative to the magnetically-coupled signal line of previous designs is the direct injection of the signal current into the interferometer comparator. An A/D converter based on this idea has been designed and successfully tested. Its schematic is shown in Fig. 1A and a circuit photo is shown in Fig. 1B. A resistor ladder is used to divide the signal in a binary sequence. Each signal component is then injected through an interferometer

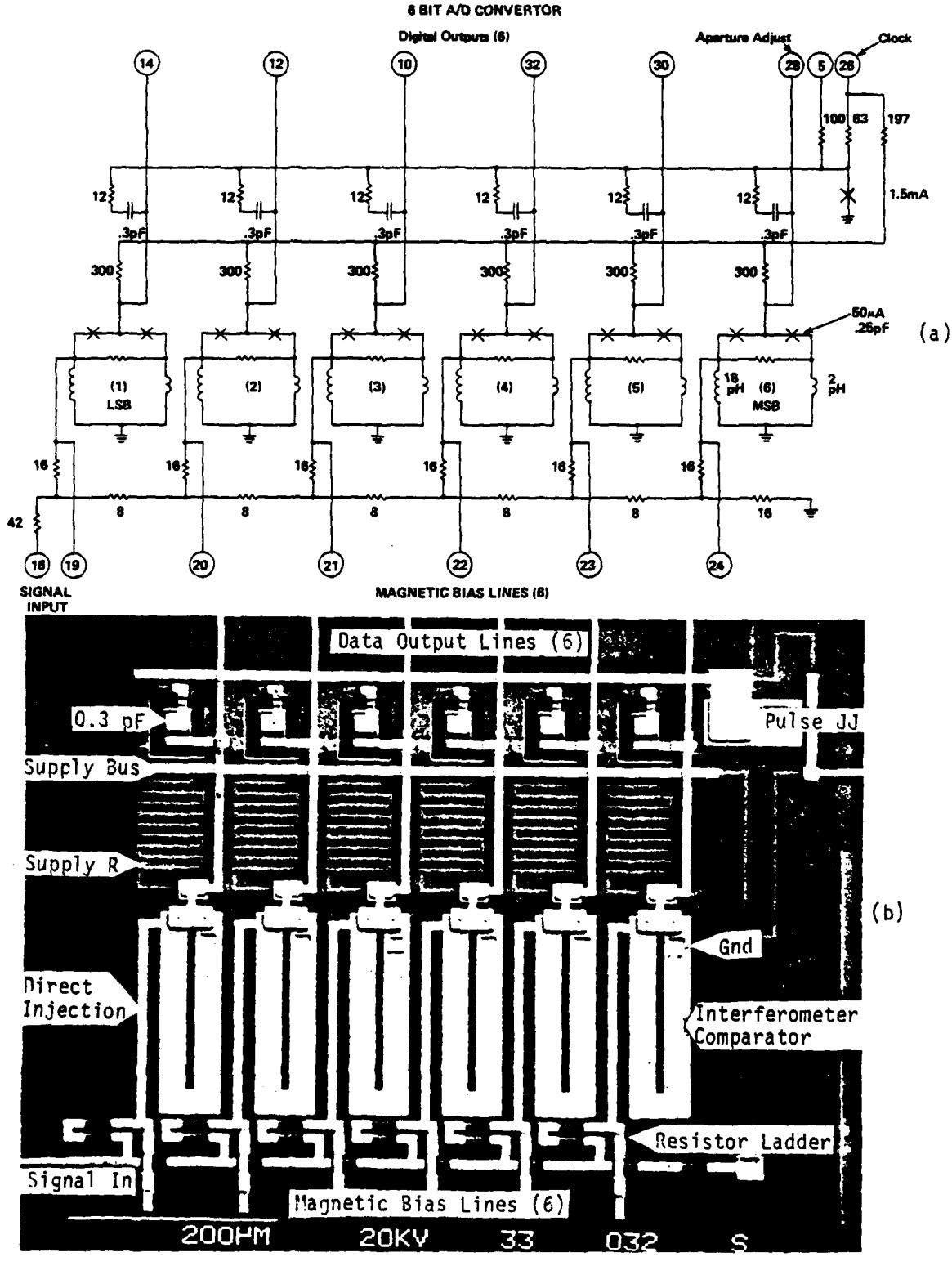

Figure 1. (a) Circuit diagram for the direct injection A/D converter and (b) a circuit photo of the device. The topology is nearly the same in the two cases.

inductance to ground. The use of identical interferometers and the symmetry of the resistor ladder assures the achievement of the desired binary coupling ratios--independent of processing parameters. The absence of insulated control lines and a reduced number of crossovers makes the circuit simpler to fabricate and more reliable. It is also expected that crosstalk between interferometers along the signal line will be greatly reduced. The principal disadvantage of this design is that the signal must be divided and applied to the comparators in parallel rather than the series technique used previously. This results in reduced sensitivity. Two changes in the interferometers have been made to help restore the sensitivity: (1) The ground point has been moved producing an asymmetric interferometer in which the injected current flows through about 90% (rather than 50%) of the total inductance, and (2) the interferometer inductance has been increased from 8 to 12 pH. This second change reduces the depth of modulation of the threshold curve with a slight reduction in operating margin. The present full-scale sensitivity for the direct injection design is 5.7 mA compared to 3.5 mA for the previous magnetic coupling design.

2.3 Sample Holder Improvements

Since crosstalk in the sample holder remains a limiting problem for high speed measurements, we are making continuing efforts to design a better sample holder. The difficulty of the crosstalk problem is illustrated by the fact that the present A/D converter operates at clock rates approximately three times the rate being used in prototype Josephson computers.

One of the causes of crosstalk is that metal parts in the sample holder cannot be solidly grounded to the chip ground plane. Stray capacitance between the signal lines and these metal parts provides a crosstalk path. The most recent sample holder approaches this problem by using plastic parts to reduce stray capacitance and by using ground-signal-ground coplanar strip lines to bring signals from coaxial cables to the chip. This results in a 38 pin chip with 14 slow lines, and 8 fast lines with two ground contacts each. A photo of the new sample holder is shown in Fig. 2. Evaluation of this device is currently in progress.

2.4 A/D Converter Test Apparatus

Performance measurements on the A/D converter have in the past been made with two different experimental arrangements. The first operates the converter at modest speed with a slowly varying signal. This mode of operation is appropriate for making the required bias adjustments and for observing the staircase function. For high speed measurements the converter must be connected to high frequency clock and signal generators and a sampling oscilloscope for observing the output data. During this reconnection process it is likely that the bias adjustments will drift thus rendering the output data inaccurate. Clearly, a method is required for quickly making and maintaining correct adjustment during high speed operation. An algorithm for automatic adjustment is described in Appendix A2. The implementation of this algorithm in an all-purpose test fixture is shown in the block diagram of Fig. 3 and photo of Fig. 4. The test fixture will (hopefully) make and maintain the bias adjustments, display the bit curves and staircase function and allow high speed operation at any time.

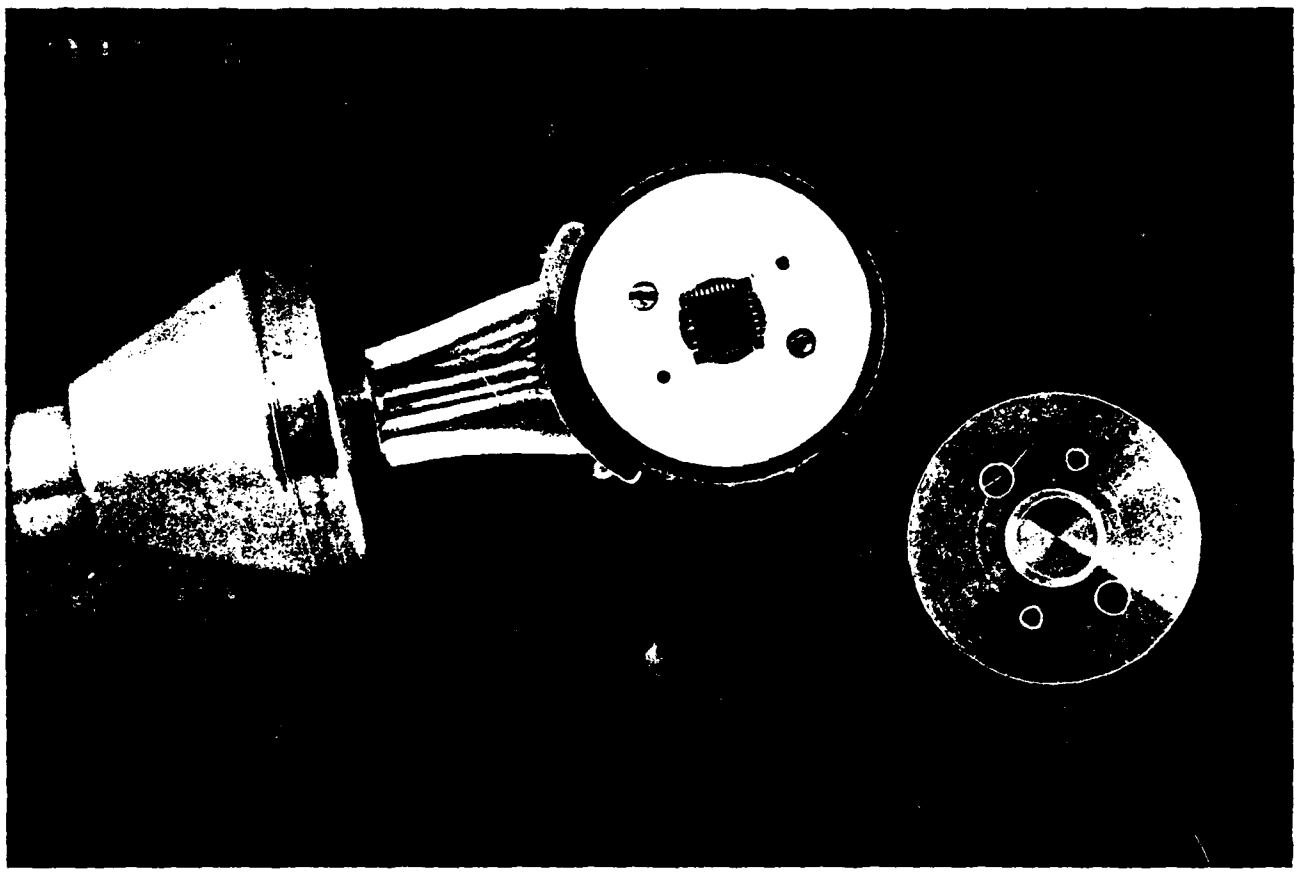

Figure 2. Photograph of a 38 pin sample holder for 6 mm square chips.

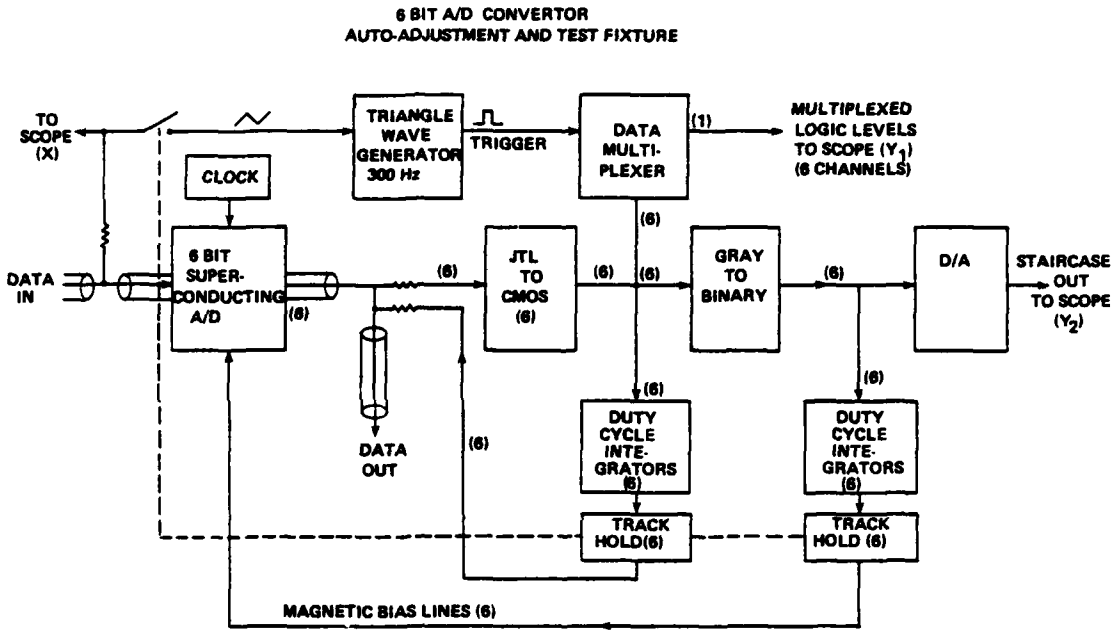

Figure 3. Block diagram of auto adjustment test fixture.

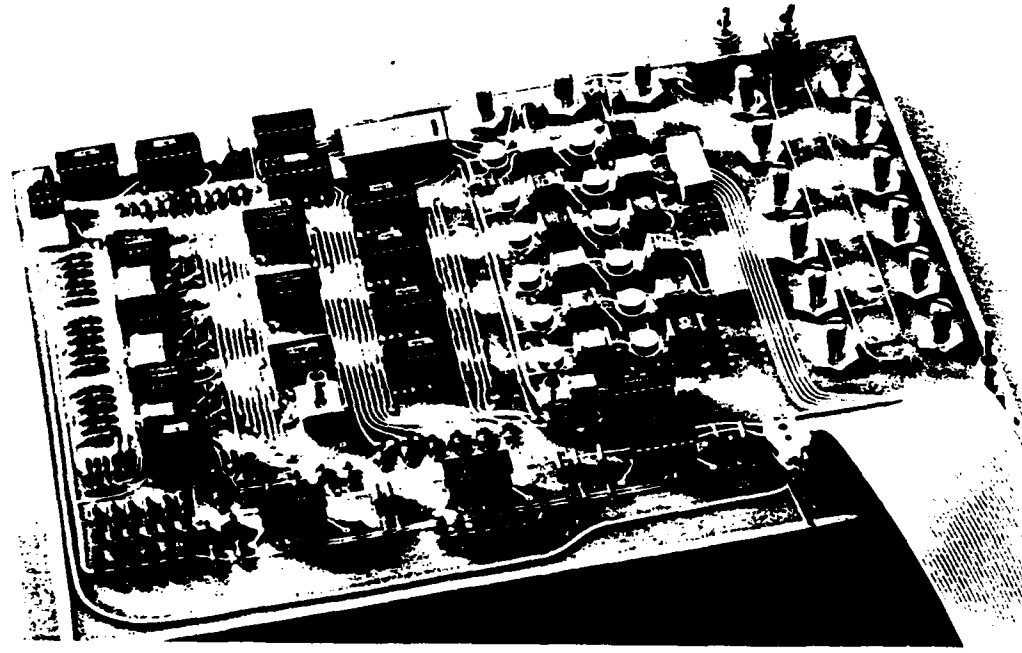

Figure 4. Photograph of auto adjustment test fixture.

This is accomplished by tapping the data transmission lines with small 1K resistors which allow the measurement and injection of low frequency signals without disturbing the high frequency signals. A nest of 12 interacting servo loops operates on these low frequency signals to make the required adjustments. A multiplexer and D/A converter provide scope displays which completely characterize the low-frequency behavior of the A/D converter.

2.5 Circuit Simulations

In the past most of our circuit simulations have been performed using the SUPER*SCEPTRE network analysis program. Because of the size of this program it requires a large computer, response is slow, and it is costly to run. Many cases can be solved using a much simpler approach which operates as follows: over small time increments, capacitors are assumed to be constant voltage sources, and inductors and junctions are assumed to be constant current sources. The resulting simplified circuit equations are then solved for the currents into capacitors and the voltages across inductors. A simple numerical integration then updates the capacitor voltages, and junction and inductor currents. Repeating this process for each time increment produces the complete time dependent behavior of the circuit.

A general version of the program (which we call micro*SCEPTRE) for a circuit with an arbitrary number of components requires only about 30 lines of BASIC or FORTRAN code. This program runs easily on any desktop computer and has duplicated SUPER*SCEPTRE results even on moderately complex circuits (15 elements). When programmed in BASIC, running times are in minutes to tens of minutes. In either case, results are usually obtained more quickly than when using SUPER*SCEPTRE. An example of an application for this program is described in the following section on aperture time.

One shortcoming of this approach is that the user must learn a procedure for generating equations to be used in programming the method. It thus lacks the topological input description of the circuit found in SUPER*SCEPTRE. It appears that a combination of approaches will be required to rapidly obtain circuit simulations. These involve changing the method of simulation from SUPER*SCEPTRE to another more efficient method and acquisition of a highly responsive time-sharing computer. Ideally, an engineer should be able to sit down at a computer terminal, enter the elements of the circuit, and see the simulated response of the circuit on his screen in seconds or minutes. With such highly responsive simulation, he should be able to adjust component values, or other circuit details, interactively, much in the way one develops a breadboard circuit with slower components.

3.0 APERTURE TIME

The sampling theorem demonstrates that a signal can be reconstructed from its values at a number of sampling instants if the length of time over which the sample is taken is infinitely short. In practice the length of time must be short enough that one makes an error in the value of the signal

of less than one least significant bit. This length of time is called the "aperture time". For a bipolar signal the maximum aperture time is given by the following:

$$t_a = \frac{1}{\pi f_s 2^{N-1}} \quad ,$$

where f_s is the sampling frequency and N is the number of bits. Thus for a 6-bit converter, with a 2 GHz sampling rate, the aperture time must be less than 5 ps and for a 4-bit converter, less than 20 ps. In this section we discuss several approaches to limiting the aperture time to such short intervals.

The reader should note that the sampling theorem also allows one to measure the integral of the signal over a longer interval whose end points are accurately known. Although this approach may prove useful in the future, it has not yet been considered for implementation in superconducting technology.

3.1 Pulsed Bias Supply

The required short aperture time can be provided by an additional circuit, or by building it intrinsically into the converter.

An approach to the latter is the use of self-gating "AND" comparators as proposed by Van Duzer's group at Berkeley. These comparators are sensitive to the signal only during the rising edge of the power supply waveform, thus yielding an aperture time equal to the supply rise time. This approach doubles the complexity of the circuit and may have rather small margins for error-free operation.

Another approach suggested by Dennis Herrell of IBM is to drive the interferometer comparators with a power supply pulse which makes a single very short excursion to the normal level for comparator operation (about 0.75 Ic) and then falls back to a point below the "floor" of the interferometer gain curve for the remainder of the cycle (see Fig. 5). In this way the signal is sampled only for a very short time at the beginning of the cycle. During the rest of the cycle the comparators are insensitive to signal changes but retain the digitized data for transfer to succeeding logic stages.

A method to generate the required pulse is to differentiate the switching transition of a single junction by using a set of small capacitors which couple the junction to each of the interferometers. The circuit (with only one comparator interferometer shown) is illustrated in Fig. 6.

It operates as follows: the sine wave power supply applies bias to the comparator interferometer (J2, J3) and to the pulse generating junction J1. Near the peak of the sine wave, J1 switches, thus delivering a pulse of

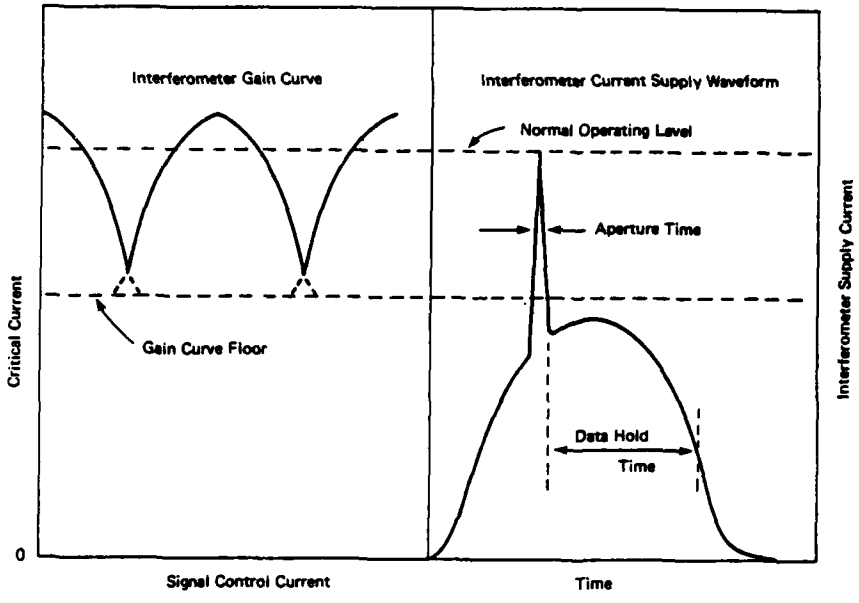

Figure 5. Diagram of a gain curve and current supply waveform shows how a short aperture time can be achieved by adding a spike to the supply waveform.

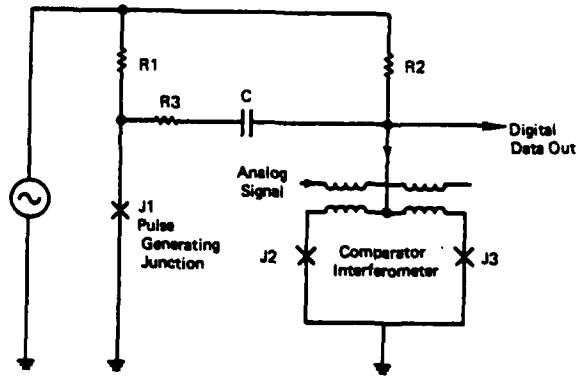

Figure 6. A circuit for producing the pulsed waveform of Figure 5.

current through capacitor C to the comparator. It will switch or not depending on the signal level. For the remainder of the cycle the comparator remains in the same state regardless of the signal level. R3 damps the principal resonance of the circuit. If the capacitance of J1 is large compared to C, the necessary isolation between comparators can be achieved.

This circuit was simulated using our micro*SCEPTRE analysis program. Figure 7 is a plot of the current I to the interferometer. The effective aperture time is the width of the spike which occurs near the peak of the sine wave.

This circuitry has been added to the latest version of our direct injection A/D converter and is shown at the top of Figs. 1A and 1B. The timing of the sampling pulse can be adjusted by applying a dc bias to the pulse generating junction via pin 5. The amplitude of the sampling pulse can be measured by observing the apparent decrease in the critical currents of the interferometers when the pulse is present. These measurements show the pulse amplitude to be about 30% less than the design value. When this defect is corrected in the next mask set it is expected that operation of the sample-and-hold can be demonstrated.

3.2 Persistent Current Sample-and-Hold

Another approach to achieving a short aperture time is to add a separate sample and hold circuit to the input of the A/D converter. This can be done by trapping a persistent current proportional to the signal in a superconducting loop as illustrated in Fig. 8. In this circuit a control current reduces the critical current in the junction J to a low value. As a result the junction switches into the voltage state and the current is transferred into the superconducting loop having inductance L. As long as the signal current remains above the reduced critical current of the junction, the signal current will flow predominantly in L. When a sample is to be taken the control current above J is reduced allowing the critical current to rise. The signal current is such that it always remains below the unreduced critical current of J. When the critical current of J is increased, the signal current is trapped in L, and any further changes in signal current flow through the junction, rather than L, because L has a much larger inductance than that of J.

Simulations of this device show that the current in L is indeed trapped when the critical current rises, and further changes in the signal flow through J. The loop L is used as the control current for the interferometers in the A/D converter. Thus with proper timing, the A/D always samples a static signal. The aperture time is just the time required to switch J into the superconducting state.

The simulations were done using a single junction with controllable critical current. The circuit looks a good deal less ideal when the single junction is replaced with a 2-junction interferometer. Several complications should now be discussed.

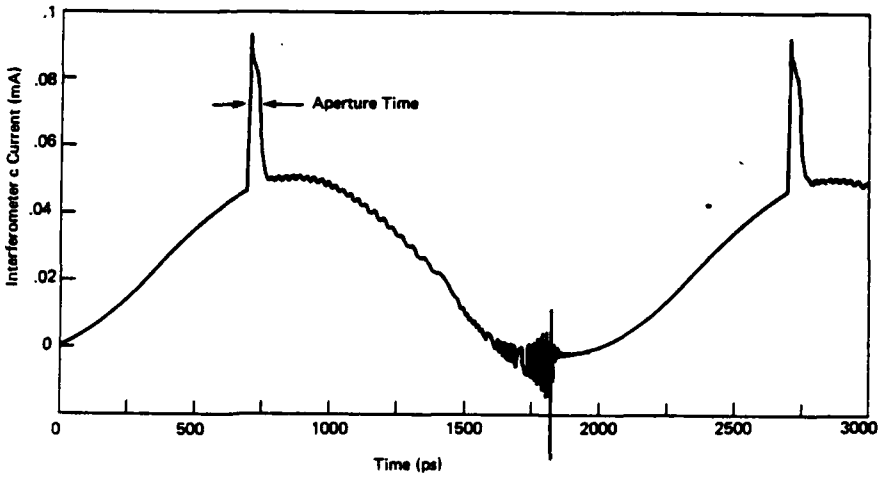

Figure 7. The results of a circuit simulation of Figure 5. The A/D aperture time is the width of the spike which occurs at the peak of the sine wave supply current.

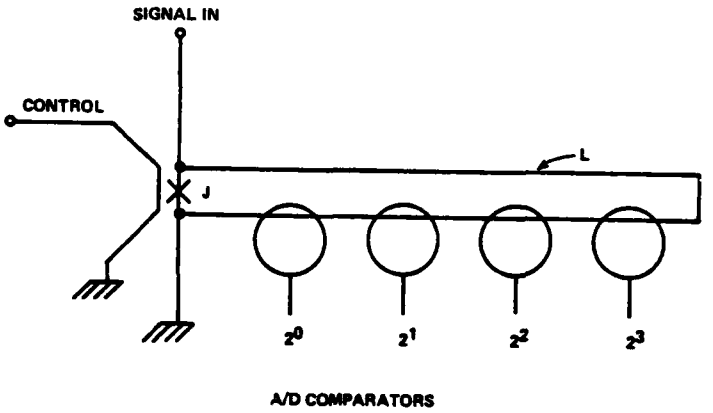

Figure 8. A schematic diagram for a persistent current sample and hold circuit.

1. The magnetic flux corresponding to the persistent current in inductance L is quantized. Thus L must be large enough that a number of flux quanta greater than the number of resolvable levels of the converter can be trapped. Thus

$$L > \frac{2^N \phi_o}{i_{max}} ,$$

where i_{max} is the current corresponding to the maximum digital output of the converter and $\phi_o = 2.07 \times 10^{-15}$ weber. Since i_{max} is 3.5 mA for our most sensitive converter, L must be at least 40 pH. This is not difficult and indeed L may be several hundred picohenries if the crossing inductances of the interferometers are included as they must be.

2. Unfortunately, it requires a large voltage to change the current in a large inductance quickly. In our case the voltage is limited to the gap voltage of the junction, about 2.9 mV. The response time of the loop is thus about 50 ps. This is a reasonable speed, since the sampling time of our present converters is 500 ps. Furthermore, if the sample-and-hold is operated in the tracking mode indicated above, this long response time is only evident after a sample when the signal current is again steered through the loop L.

3. Most difficult of all, however, is the necessity to reduce the critical current of the interferometer below the current corresponding to a least significant bit of signal current. This may impose a serious limitation on the dynamic range of this sample and hold circuit.

4.0 OVERALL SYSTEM CONCEPTS

Work on this contract has progressed to the point that thought is being given to the use of the A/D converter in a complete system. Not only is a complete system necessary for the practical use of the converter, it also appears to be imperative in order to test the device. Data is produced so fast by the device that no conventional method of storing it exists. Thus the initial system will include fast superconducting memory to store the data and later allow it to be read out more slowly into a conventional computer for analysis. The system will in fact be a transient event recorder.

One possibility for the system is illustrated in Fig. 9. One bit of the A/D converter is shown being driven from a gated sine wave supply together with a dc offset. The same supply is split into three phases by delay lines and operates a shift register consisting of a long string of AND gates. Thus a burst of M cycles from the sine wave supply converts and stores M samples of the input signal. The dc offset in the supply causes the data to be retained after shifting stops. A low frequency supply can then be used to shift the data out for further processing. Preliminary design is underway for such a shift register memory.

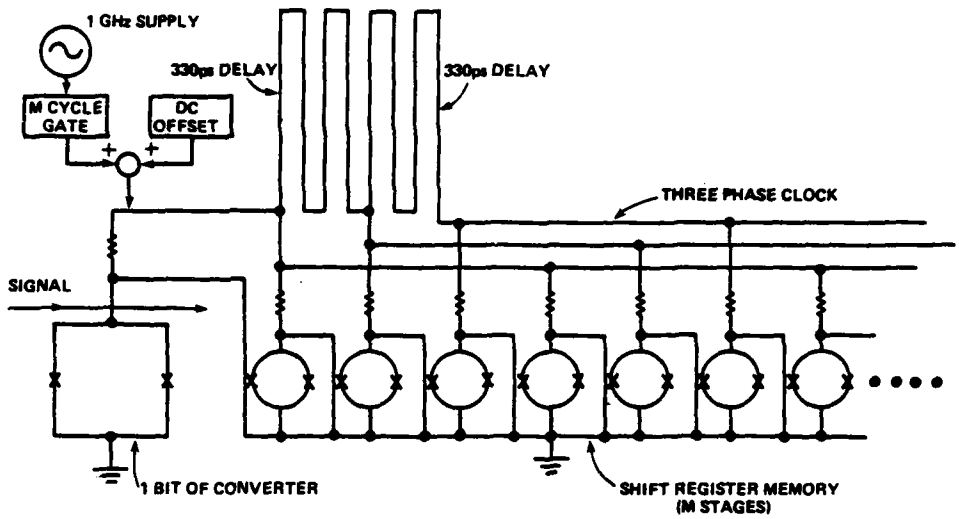

Figure 9. A schematic diagram for an A/D converter (only 1 bit shown) with shift register memory.

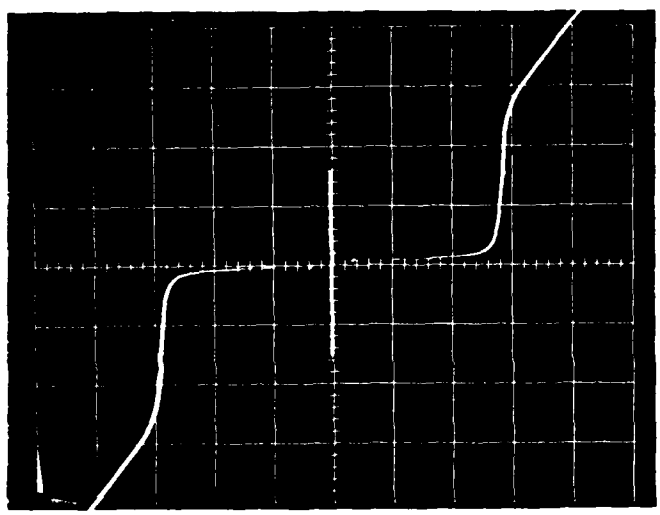

Figure 10. Typical I-V curve for a junction with a Pb-Bi upper electrode.

5.0 FABRICATION CHANGES

This section describes several changes which have been made in the fabrication process during the past year. In addition one anticipated improvement is discussed.

5.1 New Mask Aligner

A new Cobilt 2020H mask aligner is now in routine use. This contact printer may be the most sophisticated available and enables alignment to within about one micron. In addition to its improved optics and alignment capability, it also offers greatly improved exposure control, uniformity, and reliability.

5.2 Pb-Bi Upper Junction Electrodes

A Lead-Bismuth alloy is now used for junction upper electrodes. Junction electrical quality is extremely high and quite reproducible. An I-V curve from such a junction is shown in Fig. 10. A significant difficulty remains, however, with this alloy. Films have very large grain size (about one micron) and edge coverage is unreliable. Evidently this problem can be alleviated by cooling the substrate during deposition. See the section below on temperature control.

5.3 New Nb Deposition Capability

Early in this program niobium ground planes were deposited in an ultra-high vacuum system with an electron beam evaporator. A catastrophic failure of the evaporator later caused an outside company to be used for Nb deposition.

In the last two months, however, a new Nb deposition system has been installed. It consists of a small dc magnetron sputter gun installed in a conventional diffusion pumped, nitrogen trapped vacuum system. The source is only large enough to coat one wafer at a time, so a rotating sample holder was constructed to enable coating multiple wafers in one pumpdown. The system produces niobium films having essentially bulk transition temperature with thicknesses of a few thousand angstroms.

We have done intial experiments in which the Nb films are patterned using our usual liftoff technique. Edge quality has been satisfactory. The new deposition system has enabled us to begin making Nb-Pb alloy junctions which have future potential for a high reliability technology.

5.4 Future Need for Wide-Range Temperature Control of Substrates

At present the substrate temperature control in our deposition-oxidation system covers a range of about 10 to 50° Celsius. Two processes which we may wish to use in the future require the range to be extended. First, as mentioned above, Pb-Bi films exhibit very large grain size

which can be reduced by deposition onto 0^{o} Celsius substrates. Second, a new technique is about to appear in the literature for fabricating very fine grained lower electrodes. Again the grain size is reduced using a low temperature substrate, in this case 77 Kelvin.

Our present vacuum system is designed such that achieving this range of temperature will involve considerable work. This work will be done during the next year.

6.0 RELATED WORK

Additional work done by the Cryoelectronic Group of NBS adds to the total expertise which can be brought to bear on the A/D converter problem. In this section we discuss four such publications, some of which were supported by ONR under other contracts. The publications are included in this report as appendices.

6.1 Turn-On Delay in Junctions and Interferometers

R. L. Peterson has simplified previous results on turn-on delay and considerably extended their range of validity. His results are directly applicable to interferometers used in the A/D converter. They will play an important part in eventual estimates of the limiting speed of operation of the converter. The results for single junctions will appear in the Proceedings of IC SQUID, Berlin, May 1, 1980, (Appendix A3).

6.2 Review of Picosecond Response of Josephson Devices

A number of members of the Cryoelectronic Group have reviewed the expected limiting response of Josephson devices in a paper to appear in IEEE Transactions on Devices, October, 1980, (Appendix A4).

6.3 Microwave Mixers and Detectors

Collaborative work with Professor P. L. Richards and T. M. Shen has led to the experimental observation of conversion gain in SIS mixers. These mixers, produced at NBS, exhibit the best signal-to-noise ratios of any mixers ever tested at 36 GHz, (Appendix A5).

6.4 Analog Sampling

An analog sampling device has been constructed which has been used to observe the shortest transition time ever seen in an electric circuit, 9 ps. Further improvements in this device should lead to even better sampling times. An effort is now underway to couple the device to signals generated at room temperature, (Appendix A6).

7.0 INFORMATION EXCHANGE

Leadership

R. E. Harris served as vice chairman and local arrangements chairman of the Workshop on Josephson Digital Devices, Circuits, and Systems, Copper Mountain, Colorado.

C. A. Hamilton served on the organizing committee for the Workshop on High Speed A/D Conversion - 1980, Portland, Oregon.

Invited Talks

1. "Superconducting Electronics", seminar at Tektronix, Inc., Beaverton, Oregon, C. A. Hamilton, June 4, 1979.

2. "A High Speed Superconducting A/D Converter", 37th Annual Device Research Conference, Boulder, Colorado, C. A. Hamilton, June 25, 1979.

3. "Introduction to Josephson Devices", Workshop on Josephson Digital Devices, Circuits, and Systems", Copper Mountain, Colorado, R. E. Harris, August 21, 1979.

4. "Superconducting Striplines", Workshop on Josephson Digital Devices, Circuits, and Systems", Copper Mountain, Colorado, R. L. Kautz, August 21, 1979.

5. "An A/D Converter Based on Quantum Interference", Workshop on Josephson Digital Devices, Circuits, and Systems", Copper Mountain, Colorado, C. A. Hamilton, August 22, 1979.

6. "A/D Conversion Using Superconducting Quantum Interference", Workshop on High Speed A/D Conversion - 1980, Portland, Oregon, C. A. Hamilton, February 12, 1980.

7. Panel on "Competing Technologies for Gb Logic", International Solid-State Circuits Conference, San Francisco, California, R. E. Harris, with others, February 13, 1980.

APPENDICES

A1. "Multiple Quantum Interference Superconducting Analog-to-Digital Converter," Richard E. Harris, C. A. Hamilton, and Frances L. Lloyd, Appl. Phys. Lett. 35, 720 (1979).

A2. "A Superconducting 6-Bit Analog-to-Digital Converter with Operation to 2 x 10^9 Samples/Second," C. A. Hamilton and Frances L. Lloyd, IEEE Electron Device Lett. EDL-1, 92 (1980).

A3. "Turn-on Delays in Single Josephson Junction Devices," R. L. Peterson, Proceedings of IC SQUID, Berlin, May 1, 1980.

A4. "Picosecond Applications of Josephson Junctions," D. G. McDonald, R. L. Peterson, C. A. Hamilton, R. E. Harris, and R. L. Kautz, IEEE Trans. on Electron Devices, October 1980.

A5. "Conversion Gain in mm-Wave Quasiparticle Heterodyne Mixers," T. M. Shen, P. L. Richards, R. E. Harris, and F. L. Lloyd, Appl. Phys. Lett. 36, 777 (1980).

A6. "A Superconducting Sampler for Josephson Logic Circuits," C. A. Hamilton, F. L. Lloyd, R. L. Peterson, and J. R. Andrews, Appl. Phys. Lett. 35, 720 (1979).

Multiple-quantum interference superconducting analog-to-digital converter[a)]

Richard E. Harris, C. A. Hamilton, and Frances L. Lloyd
Electromagnetic Technology Division, National Bureau of Standards, Boulder, Colorado 80303

(Received 16 March 1979; accepted for publication 11 May 1979)

Multiple-quantum interference in a superconducting interferometer is used for analog-to-digital conversion. The simple fully parallel four-bit converter which is described is the first known use of this effect in a digital circuit. Sampling rates of 2×10^8 per second were achieved, and much higher rates appear possible.

PACS numbers: 06.60.Jn, 74.50. + r, 06.70.Dn, 06.70.Ep

This letter describes the first known use in a digital circuit of the multiple lobes of the threshold curve of a superconducting interferometer. Although digital applications of such interferometers have been known for several years,[1,2] only the first lobe has been used previously. An analog-to-digital (A/D) converter using multiple lobes has been proposed.[3,4] We demonstrate a realization of this concept in a four-bit A/D converter operating at a rate of 200 megasamples per second. An increase to rates well above one gigasample per second may be possible.

This experiment makes use of four current comparators, each consisting of a Josephson three-junction interferometer which has the junctions connected in parallel by superconducting loops.[5] A photograph of one of the interferometers is shown in Fig. 1 (a). The center junction has twice the critical current of each of the symmetrically arranged outer junctions. Such an interferometer has a current-voltage characteristic like that of a single junction. Its maximum 0-V current I_m (threshold current) is modulated by an applied magnetic field in a way determined by the junction critical currents and the loop inductances. The junctions are sufficiently small (about 4 μm square) that the magnetic fields used have negligible effect on them directly. By choosing $Li_0 \approx \frac{1}{4}\phi_0$, a threshold curve like that shown in Fig. 2(a) is obtained. Here L is the inductance of one of the superconducting loops, i_0 is the critical current of one of the outer junctions, and ϕ_0 is the flux quantum $h/2e$.

The periodicity of the threshold curve is a manifestation of quantum interference occurring in the interferometer. The net phase change of the wave function describing the superconducting loops in the interferometer increases in proportion to the amount of magnetic flux applied through the loops of the interferometer. A net phase change of 2π corresponds to one additional flux quantum penetrating the loop. The threshold curve repeats whenever two additional flux quanta are added. In a two-junction interferometer, the curve would repeat for each additional flux quantum.

To use this interferometer as a current comparator, a magnetic field is applied equally through both loops. The magnetic field results from passing a current I_c through a control line above the interferometer. Its effect is illustrated by the horizontal arrow in Fig. 2(a). The current through the interferometer I_g is then raised from zero to a predetermined level $I_{g,max}$ indicated by the vertical arrow. If $I_{g,max}$ is above the threshold curve $I_m(I_c)$, the interferometer switches to the voltage state; otherwise it does not.

A single interferometer is used to generate a single bit of the output of an A/D converter, by choosing $I_{g,max}$ so that the interferometer switches, or does not switch, for equal intervals of control current. By making the control current the analog signal to be digitized, the voltage output of the gate V_g is one bit of the digital value of the signal as illustrated in Fig. 2(b). To take repeated samples, I_g is cyclically varied between 0 and $I_{g,max}$.

The next most significant bit can be generated by expanding the bit pattern of the least significant bit by a factor of 2. The expansion is produced by reducing the coupling of a second interferometer to the control line by a factor of 2. Similarly, the third and fourth bits are generated by further expanding the bit patterns of third and fourth interferometers. Thus only four interferometers are required for A/D conversion of four-bit accuracy. Moreover, since these interferometers operate in parallel, maximum speed is achieved with all four bits being produced essentially simultaneously. In general, only N interferometers are required to digitize to N-bit accuracy, with little decrease in speed needed for additional bits.

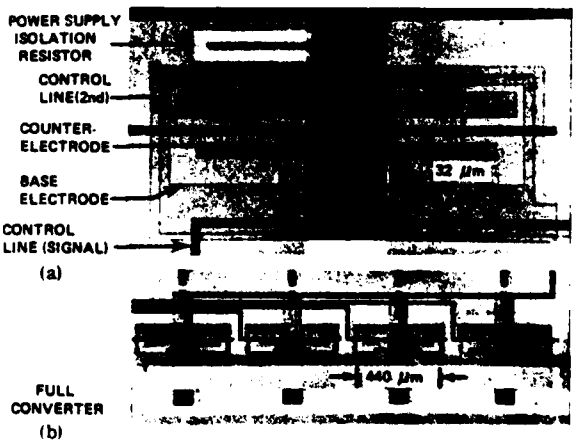

FIG. 1. (a) Photograph of one of the four interferometers in the A/D converter. (b) Photograph of a complete four-bit converter.

[a)]Work supported in part by the Office of Naval Research under contract number N00014-77-F-48.

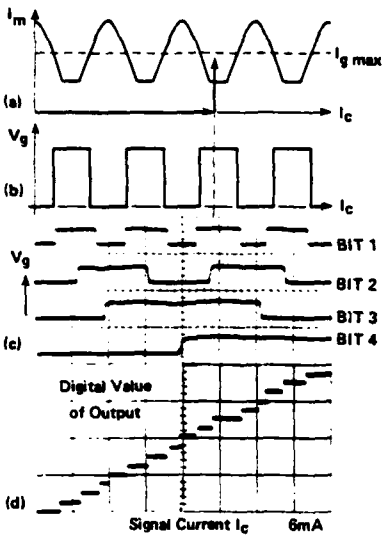

FIG. 2. (a) Threshold curve showing maximum zero voltage current I_m as a function of control current I_c. Ideal maximum curve current $I_{g,max}$ is shown by dashed line. (b) Output voltage for ideal $I_{g,max}$ as function of control current. (c) Actual bit pattern for the four-bit A/D converter. (d) Value of digital output of converter versus analog signal (traced).

Figure 1 (b) shows a complete four-bit converter. The observed bit patterns for this converter are shown in Fig. 2(c). This pattern is a Gray code representation of the analog signal. Gray code is frequently used in A/D conversion since only one bit changes as the signal crosses from one digital level to the next. Another significant feature of this A/D converter can be realized by adding a second control line to each interferometer. By applying a dc bias through one of these control lines, the bit pattern from that gate can be shifted to values of higher or lower current. Using this feature, a variety of unique codes can be produced.

Superconducting A/D converters of the type described have been fabricated with two converters on each 6.4-mm-square chip. The interferometers are much like those described in Ref. 5, although they are scaled up in linear size by a factor of 4 to make fabrication simpler. The circuits contain resistors for damping the interferometer resonances and for terminating transmission lines. The impedances of the striplines on the chip are chosen for proper matching to the interferometer impedances. The coupling of the signal to the interferometers is varied by adjusting the length of the control line above the interferometers in the ratios 1:2:4:8. As can be seen in Fig. 1, the control line is diverted around the portion of the wide counterelectrode passing over the interferometer. In this region the counterelectrode provides shielding which is not readily calculable. Furthermore, this control-line arrangement causes the coupling to each half of each interferometer to be insensitive to slight misalignment during fabrication.

The interferometers have been tested with a gate current having a frequency (i.e., sampling rate) of 200 MHz. Due to equipment limitations only two of the four bits were tested at this speed. They were found to produce outputs which repeat synchronously with a nominally 50-MHz signal. In this sense, the converter has been demonstrated to operate at 200 megasamples per second. Based on the observed switching times, we believe that the devices fabricated will operate properly at rates up to about 700 megasamples per second. Improving the ground plane contacts should allow the converter to operate at much higher rates. Reported switching times[5] of 42 ps for these devices suggest rates well above 1 gigasample per second.

To assess the accuracy of the full device, conventional circuitry was used to convert from Gray code back to an analog signal. The resulting output-vs-input curve [Fig. 2(d)] is monotonic with a maximum error in step width of 0.7 least significant bits. These measurements were performed at about 10 megasamples per second with the signal swept at a few hundred hertz.

The coupling of the signal to the interferometers was determined to be in the ratio 1:2:4:8 within about 1%, indicating that this design may be suitable for converters of 6 to 8 bits.

The initial tests of this A/D converter design suffer from variations in interferometer characteristics, trapped flux, and the general difficulties of high-speed testing. In addition the ultimate accuracy of the device may be limited by dynamic effects including subthreshold switching and signal line transients caused by switching. Nevertheless, the design appears to offer great promise for significantly higher speeds in the future.

It is a pleasure to acknowledge helpful conversations with T. Fulton, L. Geppert, D. Herrell, and H. Zappe. R. Peterson assisted with the understanding of the threshold curves, D. McDonald provided constant encouragement, and L. Mullen assisted with the fabrication.

[1]H.H. Zappe, Appl. Phys. Lett. 27, 432 (1975).
[2]A superconducting successive approximations A/D converter was reported by M. Klein, ISSCC 20, 202 (1977).
[3]H.H. Zappe, IBM Tech. Discl. Bull 17, 3053 (1975). Zappe's paper describes a related method of producing the various bits, but achieves the expansion of the patterns from one bit to the next by changing the inductances of the interferometers. The present approach of changing the coupling allows the use of optimally designed interferometers, each having identical response time, for each of the bits.
[4]An optical interference analog of the present converter is given by H.F. Taylor, Proc. IEEE 63, 1524 (1975); Appl. Phys. Lett. 32, 559 (1978).
[5]M. Klein, D.J. Herrell, and A. Davidson, ISSCC 21, 62 (1978); L.M. Geppert, J.H. Greiner, D.J. Herrell, and S. Klepner, IEEE Trans. Mag. MAG-15, 412 (1979).

A Superconducting 6-Bit Analog-to-Digital Converter with Operation to 2 × 10^9 Samples/Second†

C.A. HAMILTON, MEMBER, IEEE, AND FRANCES L. LLOYD

Abstract — **The design and performance of a 6-bit superconducting A/D converter are described. The converter is based on double junction interferometers used as current comparators. The unique periodic response of these comparators makes possible a fully parallel N-bit converter requiring only N comparators. Conversion rates up to 2 × 10^9 samples per second have been demonstrated.**

This letter describes a superconducting A/D converter with 6-bit accuracy and operating speeds up to 2 × 10^9 samples per second [1], [2]. The A/D converter is based on a set of superconducting interferometers [3] which operate as current comparators. Each of these interferometers consists of two or more Josephson junctions connected by superconducting loops. The circuit for an interferometer is shown in Fig. 1c and its I-V curve in Fig. 1a. For currents below the maximum threshold current, I_{mo}, the device has zero voltage drop. When I_{mo} is exceeded the interferometer switches very rapidly (10-30 ps depending on overdrive) along the load line to the energy gap voltage ($V_G \cong 2.9$ mV). As shown in Fig. 1b, the threshold current I_m has a maximum value I_{mo} and a periodic dependence on a control current I_c which is magnetically coupled to or directly injected into the interferometer. Thus, by applying a signal, I_c, to the control input and pulsing the interferometer current I_g to a predetermined level, (see Fig. 1b), the interferometer can be used as a comparator. As shown in Fig. 1d, this comparator has the unique property that its digital output, V, is a periodic function of the analog signal input, I_c. This is exactly the property required for an A/D converter since each output of an A/D converter is a periodic function of the signal input with the period changing by a factor of two from one bit to the next.

Figure 2a is the circuit diagram for a 6-bit converter using this idea. The required variation in periodicity is achieved by factor of two changes in the mutual inductance between the common signal line and each successive interferometer. When a conversion is to be made, a current pulse, I_g, is applied to the power supply line so that all interferometers are biased to the level shown in Fig. 1b. Each interferometer for which this bias level exceeds the threshold curve will switch to the voltage state producing a 2.9 mV pulse on its output line. These pulses are a digital representation of the analog signal. For continuous operation the supply line is driven by a pulse train, or at the highest speeds by an offset (monopolar) sine wave. This A/D converter operates in a fully parallel fashion and requires only one comparator for each bit of accuracy. Figure 2b is a photo of the circuit which was made using an eight level fabrication procedure described elsewhere [4].

Figure 3 shows the six bit patterns as a function of analog signal level. Note that the output is in Gray code so that perfect alignment of the threshold levels is not required. In Fig. 3b the Gray code is converted back to an analog signal. The monotonic staircase verifies that the accuracy of the converter is ± 1 LSB (least significant bit).

Crosstalk between the chip leads causes considerable difficulty in testing this device at very high speed. For this reason a mount has been designed in which the pads on the chip are pressed against the ends of 8 differential microstrip line pairs which are etched on a G-10 circuit board. Six millimeters away from the chip, each stripline pair converts to 50 Ω coax. The coax shields are tied together only at the superconducting ground plane on the chip.

Even with these measures, crosstalk from the high level ac power supply (30 mV) exceeds the output signal levels (2.9 mV) at sample rates above 2 × 10^9 per second. We are currently not able to fully verify the operation of the converter at this rate. However, by synchronizing a signal waveform with the 2 GHz power supply, it is possible to use a sampling oscilloscope to observe the digital data on the output lines. Figure 3c shows the data on one of the six output lines for eight successive samples of a 6 ns wide signal waveform. The crosstalk has been electronically subtracted from this data. It is clear that the full utilization of this A/D converter will require either a greatly improved sample holder and interface electronics or some data rate reduction on the chip. The ultimate speed achievable with this type of converter is determined by the turn-on-delay of the interferometers and the time required to reset them to the zero voltage state at the end of each cycle.

The first A/D converter of this type [1] used 3-junction interferometers similar to those developed for logic applications [5]. Small fabrication variations can cause these devices to have nonperiodic threshold curves. For this reason the new design uses 2-junction interferometers. The desired mutual inductance ratios of 1:2:4:8:16:32 are achieved by varying the length of signal line which passes over each interferometer. As shown in Fig. 2b, these lengths

Manuscript received Feb. 27, 1980; revised received April 1, 1980.
The authors are with Electromagnetic Technology Division, National Bureau of Standards, Boulder, CO 80303

0193-8576/80/0500-0092$00.75 ©1980 IEEE

vary from a small fraction of a turn (MSB) to 2 full turns (LSB).

In order to ensure large operating margins, it is desirable to have the depth of modulation of the threshold current (Fig. 1b) as large as possible. This modulation depth is given by:

$$I_m(\min)/I_{mo} \cong \frac{LI_{mo}}{\phi_o}, \frac{\phi_o}{L} > I_{mo},$$

where $\phi_o = 2.07 \times 10^{-15}$Wb = 2.07 pH mA. In order to drive 50 Ω output lines, I_{mo} has a minimum value of about 100 μA. There is thus a trade off between operating margin which improves for small L and sensitivity to the signal which improves for large L. We have chosen L = 6.5 pH which gives I_m (min)/I_{mo} ~ 0.3. The resulting full scale signal current is 3.5 mA.

Various types of on-chip crosstalk, signal reflections, and spurious resonances must be eliminated. For this reason the entire circuit is built on a superconducting ground plane and all lines are matched and terminated. The damping resistor R_D " 2 Ω minimizes a resonance between the interferometer inductance and the junction capacitance [6]. The power supply isolation resistor R must also be large enough to prevent a transition in one interferometer from significantly affecting its neighbors. The minimum value of R to prevent LSB errors is found to be

$$R \geq \frac{2^N V_G}{I_{mo}} \left\{ 1 + \sqrt{1 + V_G 2^{N+1}/NI_{mo}Z_s} \right\}^{-1}$$

where N is the number of bits and Z_s is the power supply source impedance. For I_{mo} = 100 μA, V_G = 2.9 mV, N = 6, and Z_s = 50 Ω, R ≥ 400 Ω. Since the interferometer bias levels are approximately 75% of I_{mo}, the peak supply voltage is 30 mV and the average supply dissipation is about 9 μW for the entire converter.

In order to achieve monotonic operation with 6-bit accuracy it has proven necessary to compensate for circuit variations by making adjustments to both the on-off ratio (signal range for which data = 1 divided by signal range for which data = 0) and "phase" of each of thee 6-bit curves (Fig. 3a). These 12 adjustable parameters can be automatically set by simple room temperature electronics as follows: With the signal line driven by a full scale triangle wave, the on-off ratio of each bit curve is measured by simple averaging. Any deviation from unity is used to control a dc current which is injected back into the output line. This changes the peak supply level for that bit (i.e., the intersection of the dashed line and the threshold curve, Fig. 1b) and thus corrects the bit curve on-off ratio. Six of these servo loops are used to achieve unity on-off ratio for each interferometer. It can be shown that when the Gray code output is converted to binary code a "phase" error in Gray code becomes an on-off ratio error in binary code. Thus, a similar set of averaging circuits on the binary code outputs can be used to drive dc currents into an additional bias control line (see Fig. 2) which overlaps each interferometer. The currents in these lines shift the bit curves to the right or left to achieve the proper phase. This automatic circuitry can make the 12 adjustments in a fraction of a second. The bias levels are then held constant while data conversion takes place. At present, DC drifts, temperature variations or changes in local magnetic field require the adjustment to be repeated several times per hour.

Acknowledgement

The authors acknowledge helpful discussions with R.E. Harris and H.H. Zappe and the financial support of the U.S. Office of Naval Research under Contract No. No. N00014-79-F-0020.

References

[1] Harris, R.E., Hamilton, C.A., Lloyd, F.L., "Multiple-Quantum Interference Superconducting Analog-to-Digital Converter," Appl. Phys. Lett., Vol. 35, pp. 720-721, 1979.

[2] Zappe, H.H., "Ultrasensitive Analog-to-Digital Converter Using Josephson Junctions," IBM Tech. Discl. Bull., Vol. 17, pp. 3053-3054, 1975.

[3] Zappe, H.H., "Quantum Interference Josephson Logic Devices," Appl. Phys. Lett., Vol. 27, pp. 432-434, 1975.

[4] Greiner, J.H., Basavaiah, S., Ames, I., "Fabrication of Experimental Josephson Tunneling Circuits," J. Vac. Sci. Technol., Vol. 11, pp. 81-84, 1974.

[5] Zappe, H.H., "Josephson Quantum Interference Computer Devices," IEEE Trans. Magn., Vol. 13, pp. 41-47, 1977.

[6] Zappe, H.H., Landman, B.S., "Analysis of Resonance Phenomena in Josephson Interference Devices," J. Appl. Phys., Vol. 49, pp. 344-350, 1978.

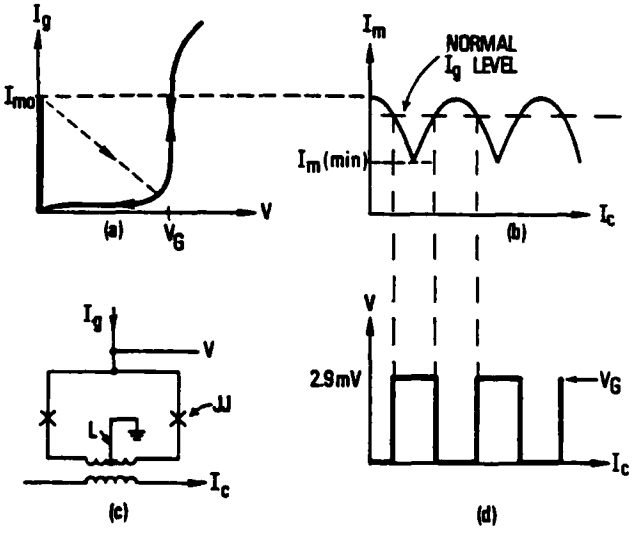

Fig. 1 (a) The I-V curve of a superconducting interferometer, (b) the dependence of the critical current I_m on a control current I_c, (c) the circuit diagram of a superconducting interferometer, and (d) the input-output characteristic of an interferometer comparator.

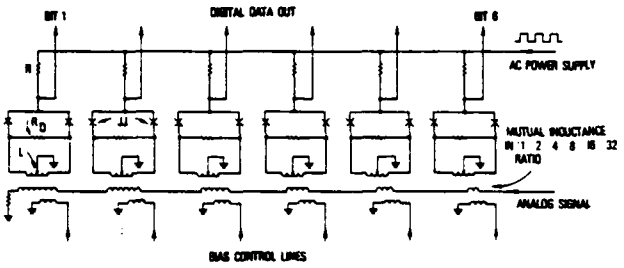

(a)

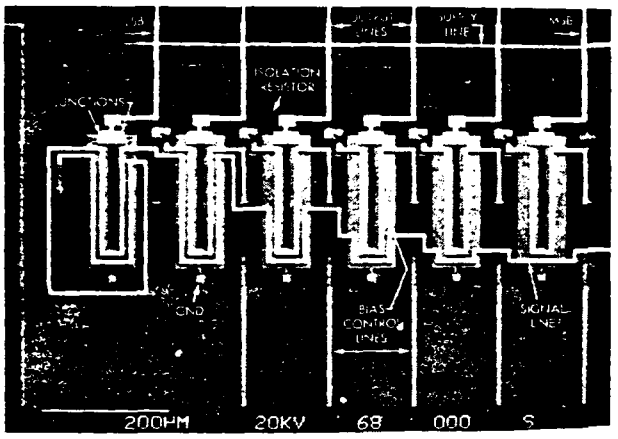

(b)

Fig. 2 (a) The circuit diagram for a superconducting A/D converter and (b) a photograph of the circuit.

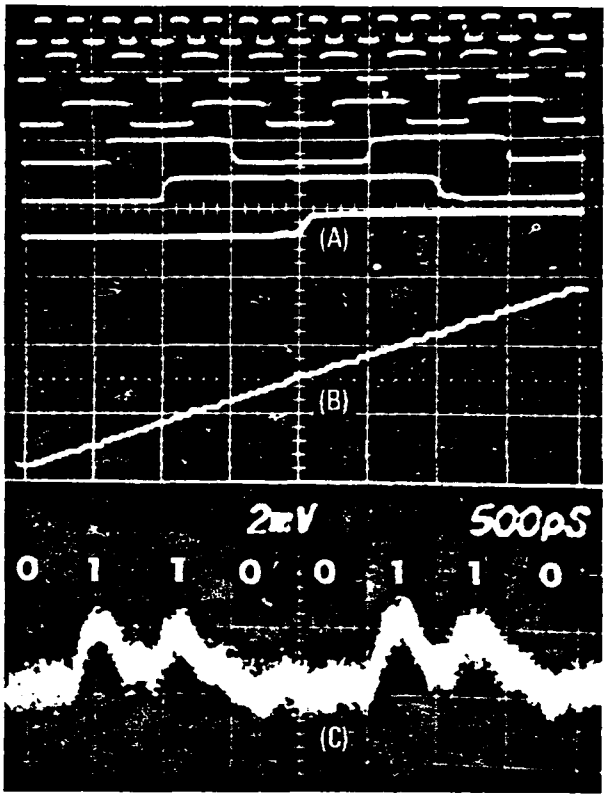

Fig. 3 The six digital outputs as a function of a signal output, (b) the digital value of the output as a function of signal level (staircase function) and (c) digital output data on one of the six output lines as a function of time. Eight successive samples are shown.

TURN-ON DELAYS IN SINGLE JOSEPHSON JUNCTION DEVICES

R. L. Peterson

Electromagnetic Technology Division
National Bureau of Standards
Boulder, Colorado 80303 U. S. A.

Introduction

When a current applied to a device containing one or more Josephson junctions exceeds the critical value for the development of a voltage, there is a characteristic delay before the onset of switching to the energy-gap voltage. This is called the turn-on delay, and was first studied theoretically by E. P. Harris (1). Figure 1 is a simulation illustrating a typical response of a single Josephson junction to a step increase of a bias current I_b through the junction critical current I_c. The risetime τ_R and turn-on delay τ_D are shown. Turn-on delay is an important consideration in the design of high-speed electronic circuits which are required to switch, as in A/D converters (2, 3).

Because the risetime is only of peripheral concern in this paper, we shall devote just a few comments to it here, and then turn our attention principally to turn-on delay in the remainder of the paper. If the bias current does not change appreciably during the switching, an expression for τ_R is easily obtained (4) from the recognition that, on average, all of the current is diverted from the junction supercurrent term $I_c \sin\phi$ to the junction capacitance C. The risetime is thus approximately the time required to charge the capacitance to the gap voltage V_g, and is about CV_g/I_c, which reduces to $4R_NC/\pi$ if the relation $V_g = 4I_cR_N/\pi$ for weak-coupling superconductors is used. Notice that it is the

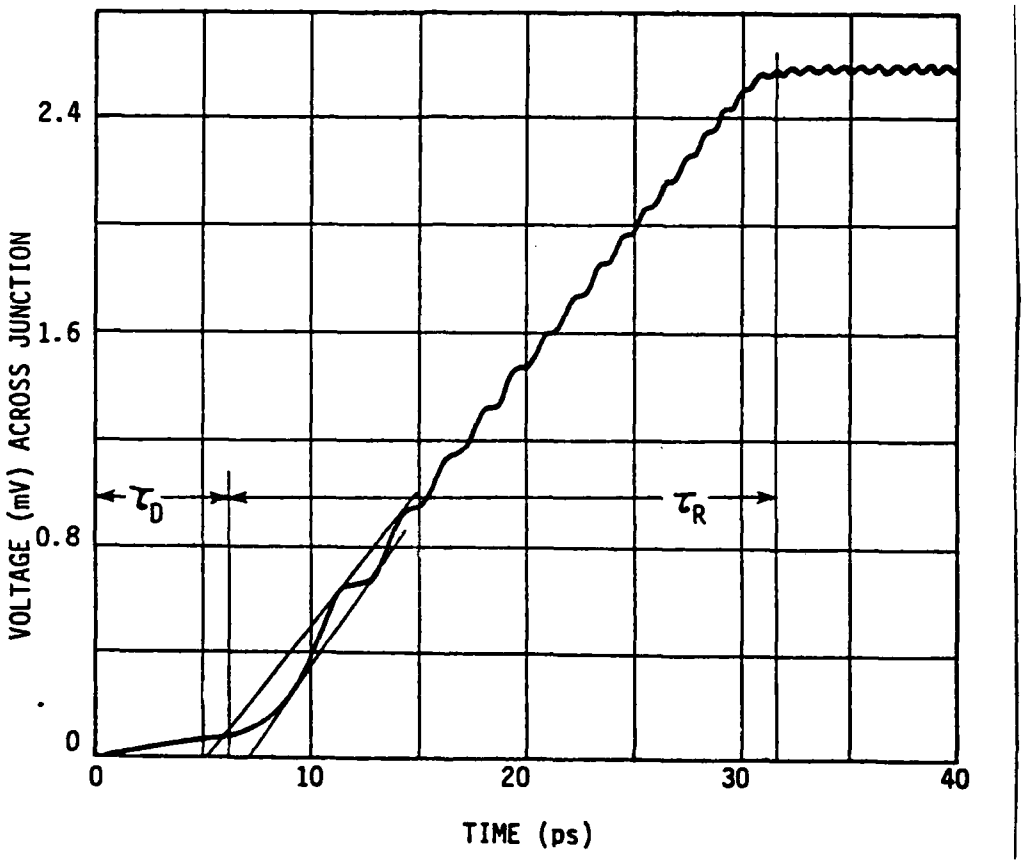

Fig. 1. Simulated response of a junction of the type shown in Fig. 2. I_c = 0.1 mA, R_J (subgap resistance) = 200 Ω, C = 1 pF, V_g = 2.5 mV. Bias current I_b stepped from 0.9 I_c to 1.1 I_c. The midline of the two tangent lines shown is the extrapolation defining the turn-on delay time τ_D. The risetime τ_R is measured from the τ_D point to the time at which the load line intersects the gap voltage leg of the quasiparticle curve.

normal state resistance R_N, rather than the actual resistance shunting the junction, which appears in this expression. The expression is valid for a constant $I_b \gtrsim I_c$. If I_b changes during the switching, the risetime will be affected. An expression for the ramp-rate dependence of τ_R will be given in the last section.

The turn-on delay time is defined here by extrapolating the rapidly rising portion of the switching curve back to the time axis; the time interval between this intersection and the time at which I_b crosses I_c defines τ_D. The extrapolation is not very precise because of the shape of the rising curve (see Fig. 1), and this makes the measured value of τ_D uncertain typically by several percent. Hence any expression for τ_D need not be very precise. This is true also because one is not ordinarily interested in a precise measurement of it, but only a good estimate. This is the spirit of the work described here.

In the following section, we analyze the turn-on delay resulting from abruptly stepping the bias current from below to above the critical current of the Josephson device. We consider both a "bare" junction, i.e., a resistively and capacitively shunted junction (the RCSJ model), and the RCSJ shunted by an inductor, i.e., a single-junction SQUID. Exact expressions for the turn-on delay time are derived in the limit of no damping, and compared to approximate formulas derived earlier (4). In the third section we develop approximate expressions for the ramp-rate dependence of both τ_D and τ_R. Since this case more closely approximates the actual operation of Josephson switching devices, the results should be of some practical importance.

A. Stepped Current

Figure 2a shows the circuits we consider. The indicated resistance R(V) may be the parallel combination of an external shunt resistance and the quasiparticle resistance illustrated in Fig. 2b. The latter figure also shows a load line intersecting the quasiparticle curve above the lower corner, the voltage at this corner being labelled V_g. If the resistance is so low that the load line intersects below V_g, the junction will not switch to the gap voltage. This case is not of concern to us here. For higher resistance, it turns out that the resistive term has relatively little effect on the turn-on delay time. This is because the resistive term is analogous to viscous drag, which is proportional to velocity. As long as the velocity (voltage) is sufficiently small, this force is relatively small. By definition, the voltage is small during the turn-on delay period, and thus the resistive term is not very important for turn-on delay.

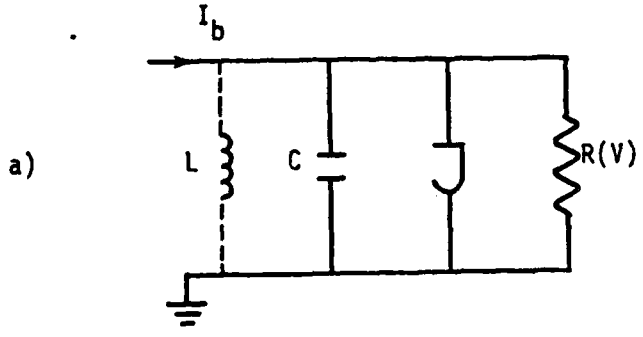

Fig. 2a. The two models considered are the resistively and capacitively shunted junction (RCSJ), and the RCSJ with an inductive shunt, forming a SQUID.

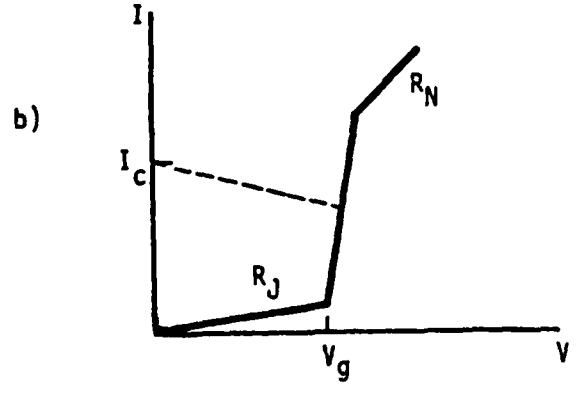

Fig. 2b. The quasiparticle I-V curve is approximated by the three legged model. A load line is shown intersecting the I-V curve in the region of the gap.

The equations describing the RCSJ model are

$$I_b = C\dot{V} + V/R + I_c \sin\phi, \tag{1}$$

$$V = \bar{\phi}_o \dot{\phi} , \tag{2}$$

where the dot means d/dt, and $\bar{\phi}_o = \Phi_o/2\pi = \hbar/2e$. Earlier, we (4) and Harris (1) used these full equations, approximated the $\sin\phi$ term, and solved the resulting equation for the time required for the phase to advance by a specified amount. We showed (4) that an advance of 1/2 radian beyond $\pi/2$ was generally an appropriate amount. Our result (4) for a bias current of $I_c(1-\delta_i)$ for $t < 0$, stepped to $I_c(1 + \delta_o)$ at $t = 0$ and thereafter held constant, was

$$\tau_D = \frac{1}{\omega_p}\left[\frac{1 + 2(\pi/2 - \phi_i)}{\delta_o + \delta_i}\right]^{1/2} , \tag{3}$$

where

$$\omega_p = \left[I_c/C\bar{\phi}_o\right]^{1/2} , \tag{4}$$

The initial value of the phase, ϕ_i, is related to the bias current at $t < 0$ by

$$\sin \phi_i = 1 - \delta_i . \tag{5}$$

Equation (3) was obtained after dropping all terms containing R, which are typically unimportant.

We have since realized that the V/R term in Eq. (1) can be dropped at the outset, and the resulting equation solved

exactly, provided I_b is constant. Thus, multiplying through by $\dot{\phi}$ allows us to write

$$\frac{d}{dt}\left[\frac{1}{2}\dot{\phi}^2 - \omega_p^2\cos\phi - \omega_p^2\frac{I_b}{I_c}\phi\right] = 0, \tag{6}$$

or, since $\dot{\phi}$ is initially zero for the stepped-current case,

$$\dot{\phi}^2 = 2\,\omega_p^2\left[f(\phi) - f(\phi_i)\right], \tag{7}$$

where

$$f(\phi) = \cos\phi + (1 + \delta_o)\phi \quad . \tag{8}$$

Hence

$$\omega_p t = \sqrt{2}\int_{\phi_i}^{\phi} d\phi'\left[f(\phi') - f(\phi_i)\right]^{-1/2} . \tag{9}$$

If, as in the earlier derivation of the approximate formula (3), we choose the phase at which the voltage begins accelerating significantly to be 1/2 radian beyond $\pi/2$, we get

$$\tau_D = \frac{2^{-1/2}}{\omega_p}\int_{\phi_i}^{\frac{\pi}{2}+\frac{1}{2}} d\phi'\left[f(\phi') - f(\phi_i)\right]^{-1/2} . \tag{10}$$

We have not found a way to evaluate the integral analytically. However, since it is independent of all junction parameters, it need be numerically evaluated only once for a given overdrive δ_o or "underdrive" δ_i. In Figure 3 we show τ_D as a function of δ_o for two values of δ_i, namely 0.0 and 0.1. The solid lines are the results of Eq. (10), and the dashed lines represent the approximate result of Eq. (3). The circles are taken from simulations as shown in Fig. 1 and discussed above. Agreement is generally excellent for the smaller overdrives. At the larger overdrives, the overestimate is probably because the final phase ϕ_f used to evaluate τ_D should not be a fixed quantity. However, the inaccuracies are not serious. The simple expression (3) is probably sufficient for all practical purposes. It can be obtained from Eq. (10) by replacing $\cos\phi$ by the first two terms of its Taylor expansion $\cos\phi_i - (\phi - \phi_i)\sin\phi_i$ over the entire region of integration.

Next we turn our attention to a single-junction SQUID, illustrated by the addition of the inductor shown in Fig. 2a. This SQUID is described by Eq. (1) with $\bar{\phi}_o\phi/L$ added to the right side. In its usual mode of operation such a SQUID does not switch to a finite voltage state. There will be, however, a turn-on delay before the entry of a flux quantum. An A/D converter based on this type of SQUID has been proposed (5, 6). This turn-on delay is easily evaluated along the same lines as above.

The "critical" value of the bias current before flux can enter the SQUID is not that of the junction, because of the shunting inductance, but rather

$$I_b^c = \frac{\bar{\phi}_o}{L}\left[\cos^{-1}(\beta^{-1}) + (\beta^2 - 1)^{1/2}\right], \qquad (11)$$

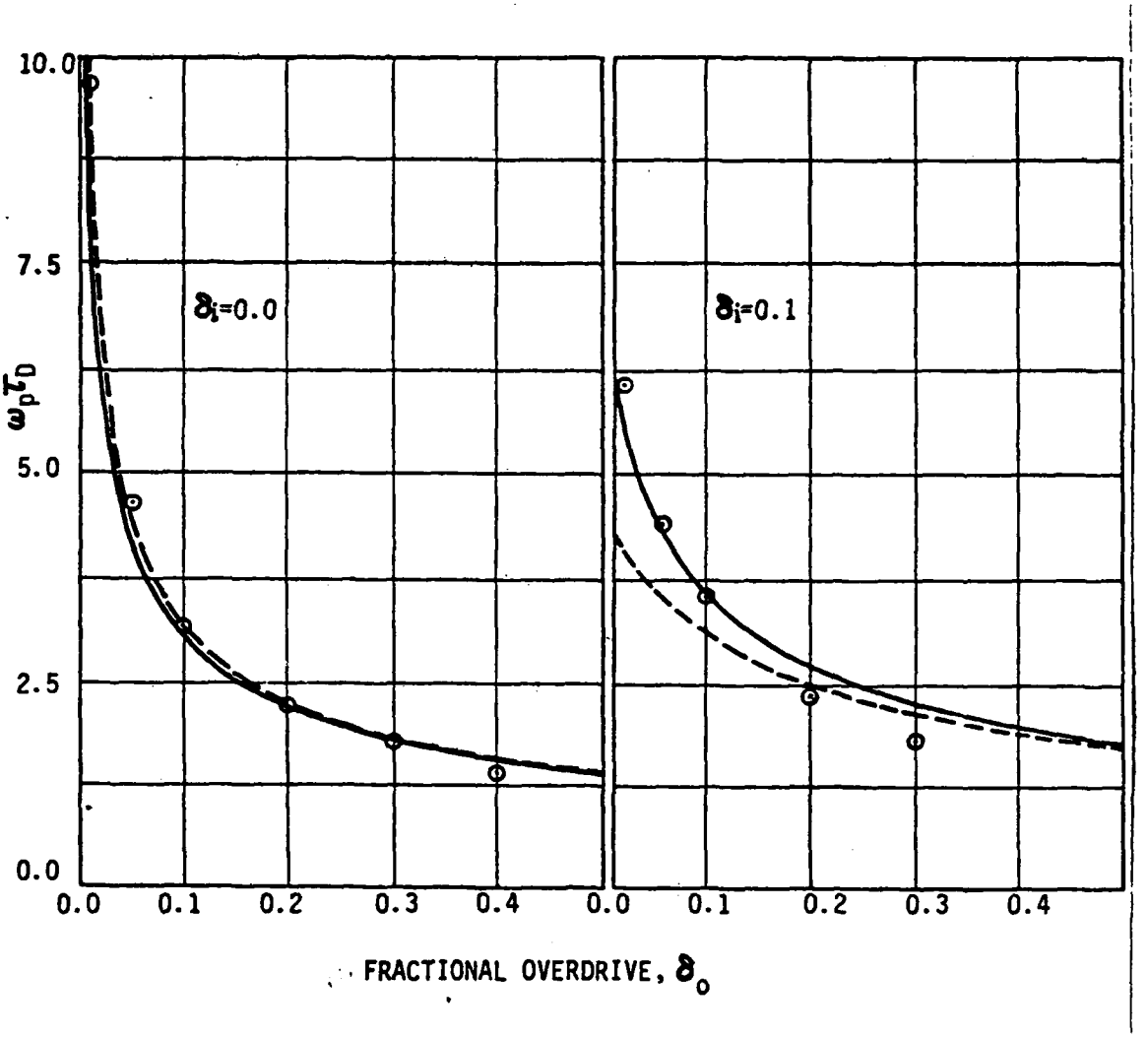

Fig. 3. Curves of $\omega_p\tau_D$ versus fractional overdrive δ_o for two values of the fractional underdrive δ_i, defined by $I_b = I_c(1-\delta_i)$. The solid curves are from Eq. (10), and the dashed curves are from the approximate Eq. (3). The circles are values of τ_D taken from simulations, as in Fig. 1.

where

$$\beta = LI_c/\bar{\phi}_o. \tag{12}$$

(Mathematical details may be found in ref. (7).) We assume that I_b is stepped from $I_b^c\ (1 - \delta_i)$ to $I_b^c\ (1 + \delta_o)$. Dropping V/R, we may cast Eq. (1) (with $\bar{\phi}_o\phi/L$ included) into the form

$$\frac{LC}{2}\dot{\phi}^2 = g(\phi) - g(\phi_i) \quad , \tag{13}$$

where

$$g(\phi) = \beta\cos\phi - \frac{1}{2}(\phi - \beta_b)^2 \ , \tag{14}$$

$$\beta_b = \frac{LI_b(t>0)}{\bar{\phi}_o} = \frac{LI_b^c\ (1 + \delta_o)}{\bar{\phi}_o} \ . \tag{15}$$

The turn-on delay is then given by

$$\tau_D = \left(\frac{LC}{2}\right)^{1/2} \int_{\phi_i}^{\phi f} d\phi \left[g(\phi) - g\ (\phi_i)\right]^{-1/2} \ , \tag{16}$$

where ϕ_f is yet to be specified. The initial phase ϕ_i is determined from

$$\phi_i + \beta\sin\phi_i = LI_b^c\ (1 - \delta_i)/\bar{\phi}_o. \tag{17}$$

To choose the final phase ϕ_f, we must decide first how to define τ_D for a SQUID. Figure 4 shows the response of a β = 20 SQUID to a bias current stepped from I_b^c to 1.01 I_b^c. The six small voltage oscillations in each large voltage excursion seen in the figure, corresponds to the entry (exit) of six fluxoids into (out of) the SQUID. The slight dampling seen is because of the 200 Ω subgap resistance assumed. Perhaps the only logical way to define τ_D is to choose it at the maximum voltage corresponding to the first flux quantum entry. Now, $dV/dt = 0$ implies $d\dot{\phi}/d\phi = 0$, which in turn requires $dg/d\phi = 0$ from Eq. (13). Thus, with Eq. (14), ϕ_f is the solution of

$$\phi_\beta + \beta \sin \phi_f = \frac{LI_b^c}{\phi_o}(1 + \delta_o) \quad . \tag{18}$$

As before, the integral in Eq. (16) cannot be determined analytically. But whereas the earlier integral was independent of junction parameters, this integral depends upon the SQUID β. Figure 5 shows the results of Eq. (16) for $\delta_i = 0$ and 0.1 for $\beta = 20$. Agreement with values of τ_D measured from simulations such as in Fig. 4 is now almost exact because the criterion for ϕ_f is fixed to a definite feature on the voltage curves. The result of neglecting the damping term in the formula for τ_D is not observable.

Analogously to the preceding case, we can extract an approximate expression from Eq. (16). By expanding $g(\phi)$, defined in Eq. (14), about its initial value, one obtains

$$\tau_D \approx \frac{1}{\omega_p} \left[\frac{2I_c(\phi_f - \phi_i)}{I_b^c (\delta_i + \delta_i)} \right]^{1/2} . \tag{19}$$

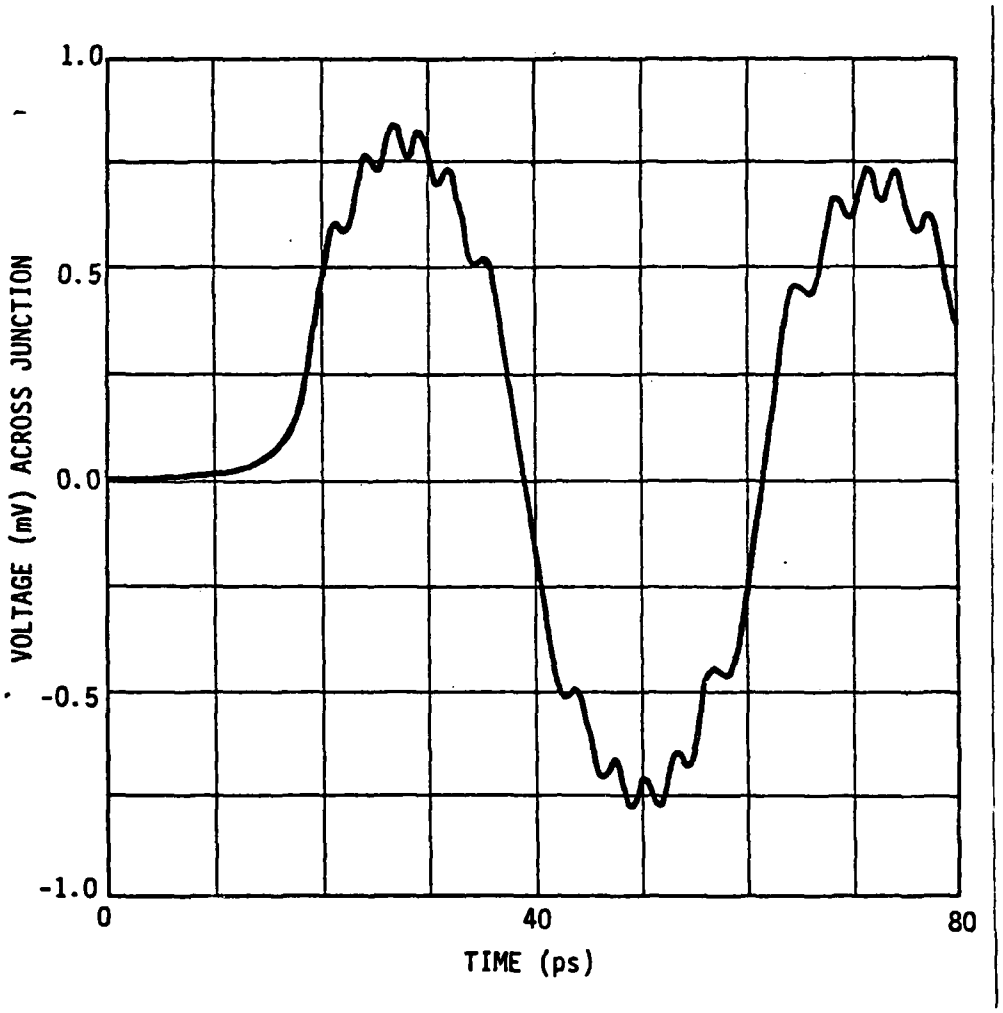

Fig. 4. Response of a single junction SQUID. The junction of Fig. 1 is placed in a superconducting loop of L_c = 19.75 pH, making $\beta = 20$. I_b is stepped from I_b^c to 1.01 I_b^c.

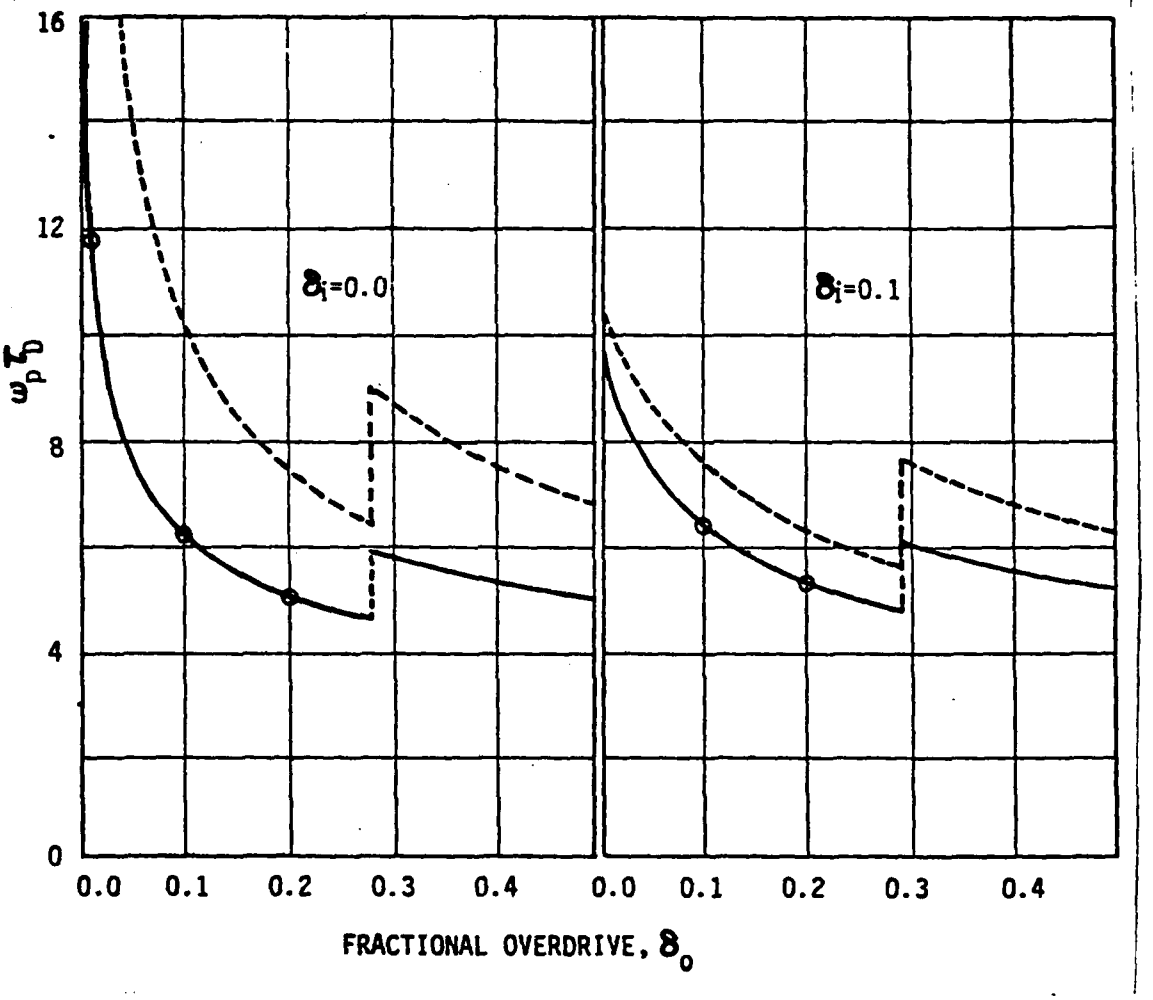

Fig. 5. Curves of $\omega_p\tau_D$ versus overdrive δ_o for δ_i = 0.0 and 0.1. The solid curves are from Eq. (16), and the dashed curves from the approximation, Eq. (19). The circles are the results of simulations. The discontinuities reflect the vanishing of the first local voltage maximum, its place being taken by the (until then) second local maximum. (An increasing overdrive distorts the potential energy curve in such a way that the earlier local maxima become less pronounced, eventually becoming only ripples on the envelope without being true maxima.)

B. Ramped Current

In the foregoing, we have assumed that the bias current was stepped instantaneously through the critical current. Although physically one can probably effectively achieve this (e.g., one should be able to develop a 1 mA current in a picosecond by a number of methods), there will be cases in which one would ordinarily be ramping more slowly. We now examine the dependence of turn-on delay upon the ramp rate of I_b.

Let I_b vary according to

$$I_b(t) = I_c(1 + \omega t), \tag{20}$$

so that $I_b = I_c$ at $t = 0$. We again omit the V/R term in Eq. (1). If $\phi(t=0)$ is near enough $\pi/2$ that $\sin\phi(0) \approx 1$, Eq. (1) may be written

$$\ddot{\phi} = \omega_p^2 \, \omega t \quad . \tag{21}$$

This is integrated twice to give

$$\phi(t) = \phi(0) + \dot{\phi}(0)t + \omega_p^2 \, \omega t^3/6 \quad . \tag{22}$$

When $\phi(0)$ and $\dot{\phi}(0)$ are known, and a suitable final phase ϕ_f for evaluating τ_D is picked, τ_D can be found by solving the cubic Eq. (22).

At this point we need to distinguish three cases. (1) The ramp-rate is suitably high. By this we mean that the intended overdrive has been reached before the system has sensibly responded. As will be seen below, or as may be surmised from Eq. (22), the criterion for this case is

$\omega >> \omega_p$. (2) The ramp-rate is suitably small. By this we mean not only $\omega << \omega_p$, but also that the switching is completed before the ramping stops. (3) The intermediate case, in which the ramp rate cannot be considered a step function, but in which the intended overdrive is reached before switching is finished.

For case (1), the formulas of the preceding section apply, and we proceed to case (2). Since here the ramp rate is small, we can expect $\phi(0) \simeq \Pi/2$, i.e., that $\sin\phi$ should track well with I_b/I_c. For $t < 0$, while ϕ is small, $\dot{\phi} \sim \omega$; as t approaches zero, ϕ increases but $\dot{\phi}(0)$ will still be of the order of ω. Thus Eq. (22) becomes

$$\omega t \left(\alpha + \frac{\omega_p^2}{6\omega^2}\omega^2 t^2\right) = \phi - \phi(0), \tag{23}$$

where α is somewhat larger than unity. Since $\omega_p >> \omega$ in the present case, it will be true that $\omega_p^2/6\omega^2 >> \alpha$, and the t^3 term dominates for $\phi - \phi(0) \lesssim 1$. Finally, if we pick $\phi_f = \frac{\Pi}{2} + \frac{1}{2}$, as the preceding section, as the phase at which to evaluate τ_D, we obtain

$$\tau_D \simeq \frac{1}{\omega_p}\left[\frac{3\omega_p}{\omega}\right]^{1/3}. \tag{24}$$

Equation (24) overestimates τ_D since the linear term in Eq. (23) was dropped. Keeping the linear term and setting $\alpha = 1$, one gets

$$\tau_D = \frac{1}{\omega_p} G^{1/3}\left[(S+1)^{1/3} - (S-1)^{1/3}\right], \tag{25}$$

where

$$G = 3\omega_p/2\omega \ , \tag{26}$$

$$S = (1 + 8/G^2)^{1/2} \ . \tag{27}$$

In Fig. 6 we compare Eqs. (24) and (25) with the results of simulations. Equation (25) is seen to be better, but the simple Eq. (24) is probably good enough for most purposes. The fact that the turn-on delays for the slowest ramp rates do not converge toward Eqs. (24) or (25) very well is probably a reflection of the fact that a fixed ϕ_f is not the best way for evaluating τ_D, as mentioned also in the preceding section.

To complete case (2), we examine the corresponding risetime τ_R. For $t > \tau_D$, $\sin\phi$ oscillates more and more rapidly, so that on average it should be negligible. Then Eq. (1) becomes

$$C\dot{V} = I_c(1 + \omega t) \ . \tag{28}$$

Integrating this for $t > \tau_D$, setting $V(\tau_D) = 0$, and defining τ_R by the time after τ_D at which V reaches V_g, we get

$$\tau_R = \frac{1 + \omega\tau_D}{\omega} \left[\left(1 + \frac{2\omega C V_g / I_c}{(1+\omega\tau_D)^2} \right)^{1/2} - 1 \right] \ . \tag{29}$$

This formula is found to be within 10% of the estimated τ_R from simulations over the ramp-rate range $\omega = 0.005\ \omega_p$ to $0.36\ \omega_p$.

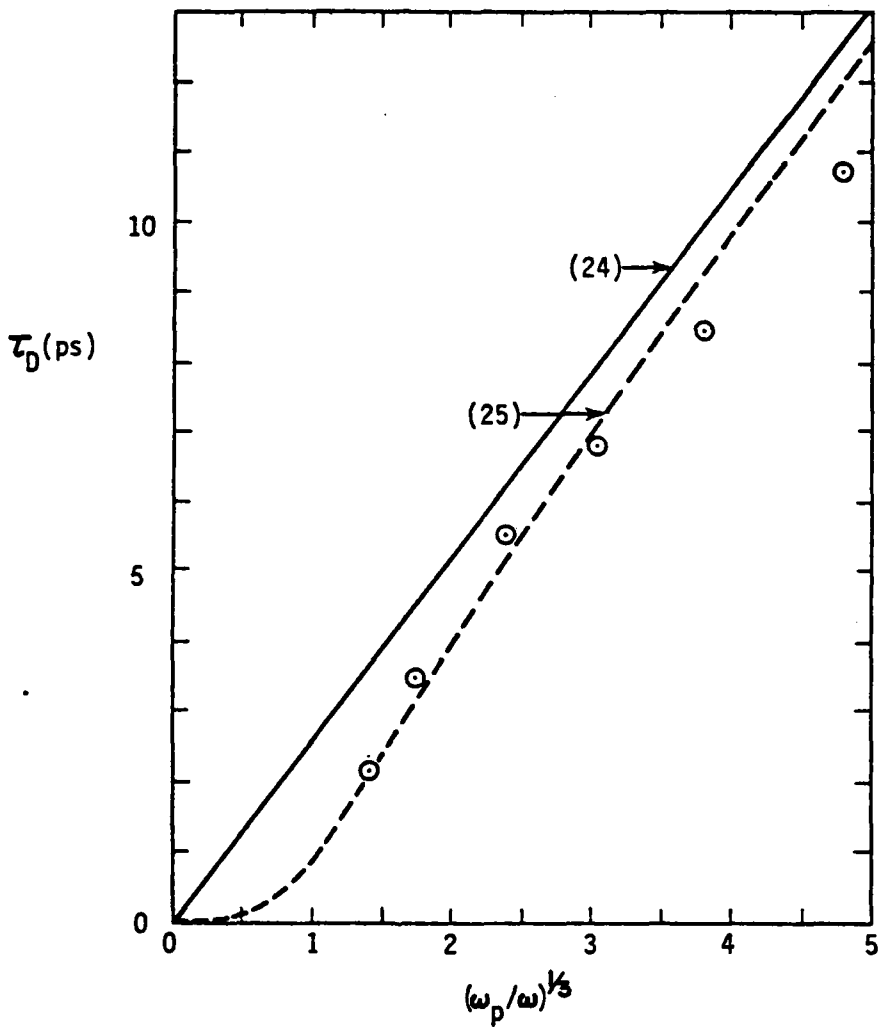

Fig. 6. Comparison of the turn-on delay time τ_D from Eqs. (24) and (25), with that estimated from simulations (circles), for current ramped up from zero at different rates. The junction is the same as that in Fig. 1. It is assumed that the overdrive is not reached before the completion of the turn-on delay period.

Case (3), the intermediate case, is not so easily evaluated, and probably not worth a detailed examination. This is the case in which the ramp rate is high enough that $\phi(0)$ in Eq. (22) is not well estimated by $\Pi/2$, nor $\dot{\phi}(0)$ by ω. Further this is the case in which, because the ramp rate is in the intermediate range, the intended overdrive is likely to be reached in the midst of the switching process. Formulas can indeed be worked out but they are not simple and each is applicable only for a narrow range of overdrives and ramp rates. Therefore we will not present any additional formulas. It is sufficient to observe that once the ramping has stopped, the system is no longer being "pushed", and the turn-on delay time, or risetime, whichever has been interupted by the halted ramping, will be lengthened over what the continuous ramp rate formulas would indicate. Since the simple ramping result of Eq. (24) is an overestimate, its use in the intermediate cases is usually satisfactory, as simulations show.

In summary, the τ_D and τ_R expressions of the stepped current section may be used for fast ramp rates, i.e., for $\omega >> \omega_p$. For slow rates, $\omega << \omega_p$, Eqs. (24) or (25), and (29) are good. In the intermediate cases, Eq. (24) will be satisfactory for τ_D, and Eq. (29) will overestimate τ_R by an acceptable amount.

References

1. Harris, E. P.: IEEE Trans. Mag., MAG-15, 562-565 (1979).
2. Harris, R. E., Hamilton, C. A., and Lloyd, F. L.: Appl. Phys. Lett. 35, 720-721 (1979).
3. Hamilton, C. A., and Lloyd, F. L.: IEEE Electron Device Lett. EDL-1, 92-93 (1980).
4. McDonald, D. G., Peterson, R. L., Hamilton, C. A., Harris, R. E., and Kautz, R. L.: IEEE Trans. Electron Devices, Oct. 1980.
5. Hurrell, J. P., and Silver, A. H.: AIP Conf. Proc. 44, 437-447 (1978).
6. Peterson, R. L.: J. Appl. Phys. 50, 4231-4239 (1979).

7. Peterson, R. L., and Gayley, R. I.: Phys. Rev. B18, 1198-1206 (1978).

Picosecond Applications of Josephson Junctions†

D. G. McDonald, R. L. Peterson, C. A. Hamilton, R. E. Harris, and R. L. Kautz, National Bureau of Standards, Boulder, CO 80303††

Abstract

The behavior of simple superconducting circuits in the picosecond regime is described in a comprehensive way, with primary emphasis being given to the step function and pulse responses of these circuits. Topics receiving detailed discussion include Josephson junction modeling with both the microscopic and shunted junction models. Limitations of the shunted junction model are explored by comparing it with experimental results and with the microscopic model. An approximate evaluation is given of the important dynamical properties of junctions made with the dominant fabrication technology (Pb alloy systems), as a function of tunneling barrier thickness. Rounding out the device aspects of the discussion, we describe in detail the properties of superconducting microstrip transmission lines, with an emphasis on their high speed behavior. Turning to simple circuits we review experimental results on the measurement of picosecond regime transient signals. The concept of turn-on delay is analyzed anew, providing simplified and extended results. Details of concepts for pulse height and pulse width measurements are explored, leading to the conclusion that the time resolution of superconducting circuits is limited to approximately the period of one plasma oscillation. With present Pb alloy fabrication technology this limit is 2 ps.

†Research partially supported by the Office of Naval Research, Contract No. N000-14-80-F-0012.

Picosecond Applications of Josephson Junctions

I. Introduction

Josephson junctions are now being used for the generation, detection, and measurement of pulses and switching transients with durations as short as about 10 ps. Our purpose here is to present a unified picture of the more basic developments in this area, including some new results. The earliest developments were the microscopic theories of superconducting tunnel junctions by Riedel (1) and Werthamer (2), which predicted essentially a flat spectral response out to the frequency of the energy gap, where a somewhat enhanced response was expected. At frequencies above the gap the superconducting response goes monotonically to zero, but with measureable effects extending out to several times the gap. Experimental investigations of the bandwidth of Josephson junctions were first carried out in the frequency domain, perhaps most importantly at 891 GHz (30% above the gap), where it was found that the response was indeed close to that at low frequencies. These experiments were done with point contact devices for which it was known, from of the analyses of Stewart (3) and McCumber (4), that the capacitance was quite small.

In the early years of the Josephson effect it was commonly thought that the response time of tunnel junctions would be severely limited by the capacitance associated with the exceedingly thin tunneling barrier. Basavaiah, Eldridge, and Matisoo (5) corrected this misconception by experimentally evaluating phenomenological tunneling theory and producing for the first time a clear picture of the relationship between tunneling barrier thickness and current density. From this it was only a small

step to relate current density to junction response time, from which it became clear that the picosecond regime should be accessible with tunnel junctions.

The evolving development of high quality superconducting integrated circuits, discussed in detail in this special issue, creates the possibility of practical utilization of nearly 1 THz of bandwidth in electronic systems. In the following we will more thoroughly examine the experimental and theoretical basis for the quantitative views expressed here. We will also present new results regarding turn-on delay, pulse detection, and pulse width measurement, with an emphasis on performance at the highest possible speeds. The order of discussion which follows is: II. EXPERIMENTAL RESULTS, III. THEORETICAL BASIS, IV. SWITCHING TIME, V. PULSE GENERATION, DETECTION, AND MEASUREMENT, VI. TRANSMISSION LINES, and VII. DISCUSSION. Our discussion emphasizes single junction devices rather than multijunction SQUIDs both because the former are simpler to analyze and to fabricate and because they probably give the fastest response, though the latter point has not been proven. We have also chosen to largely omit discussion of nonlatching devices [6] and of the resetting (or punchthrough) problems [7]. Finally, discussion of noise was omitted since fundamental physical noise will not ordinarily dominate the circuits of interest. More germane to the irregularities of practical circuits is the problem of reflections from impedance mismatches, which are nearly always present.

II. EXPERIMENTAL RESULTS

Although most of our discussion will be about the time domain response of superconducting circuits, it is appropriate to begin with a brief review of experiments in the frequency domain, both because they gave the first

experimental evidence of high frequency response and because time domain measurements are still limited to times greater than about 10 ps, whereas frequency domain measurements using far infrared lasers probe the sub-picosecond regime.

A. Bandwidth Measurements in the Frequency Domain

The most direct proof of the large bandwidth of Josephson junctions comes from a rather simple point of view. We take the low frequency description of the Josephson effect and ask at what frequency does it break down? Fortunately Josephson junctions have a special property which allows this to be done with little uncertainty.

The low frequency form of the Josephson equations relating current I to voltage V is:

$$I = I_o \sin \phi \ , \tag{1}$$

$$\dot{\phi} = \frac{2e}{\hbar} V \ , \tag{2}$$

where the dot means d/dt and e and $\hbar$ are the usual fundamental constants. These equations predict that if a superconducting junction is dc biased at voltage V_b, the phase ϕ will advance uniformly in time and the current I will oscillate with amplitude I_o at frequency

$$f_J = \frac{2e}{h} V_b \quad (\frac{2e}{h} = 484 \text{ GHz/mV}). \tag{3}$$

A more complete theory of junctions, which will be discussed later, makes it clear that it is the quantity I_o, the junction critical current,

which eventually begins to decrease with frequency. That is not at all surprising since one would not expect to be able to produce significant optical frequency current, for example, from a state of matter which has a binding energy of only a few mV.

The experimental problem then is to measure I_o as a function of frequency. Since the frequency range of interest exceeds 1 THz it is a difficult practical problem.

Brian Josephson, in his original paper on superconducting tunneling (8), suggested an indirect method for observing the supercurrent I_o at microwave frequencies. This method, first successfully used by Shapiro (9), is based on the simultaneous application to a junction of dc bias and microwave radiation. The basic idea is that for proper adjustment of V_b the frequency of the Josephson oscillation f_J will be equal to the frequency f_a of the applied radiation. Since the Josephson junction is a nonlinear device, it will produce a beat frequency current at the difference frequency $f_J - f_a$, which in this case is at zero frequency. The result is a current step on the I-V characteristic. This situation can be analyzed using Eqs. (1) and (2) with

$$V = V_b + V_1 \cos(2\pi f_a t + \theta_1). \tag{4}$$

From this analysis it is found that the induced dc is:

$$I_{dc}(f_J = f_a) = 2I_o J_1(2eV_1/hf_a), \tag{5}$$

where J_1 is the first order Bessel function of the first kind. Thus I_{dc}, considered as a function of V_1, has a maximum value of 1.16 I_0. The anaylsis given here omits the shunt capacitance and shunt resistance of real junctions. Simulations by Russer (10) and Kautz (11) have shown that the induced dc given by Eq. (5) is an upper bound which is closely approached in the right circumstances. The upper bound suffices for our purposes so we will not consider in detail the effects of the shunts.

Experiments of this type specifically designed to explore the bandwidth of the Josephson effect were reported several years ago by McDonald, et al., (12, 13) and more recently by Weitz, Skocpol, and Tinkham (14). Perhaps the most direct evidence for large amplitude Josephson oscillations at a frequency in the vicinity of the energy gap is illustrated (12) in Fig. 1. The experimental technique which was used for acquiring this data largely removed the background I-V curve from the data and emphasized the induced dc. This was an experiment in which a Josephson junction was simultaneously irradiated at 891 and 805 GHz. As the voltage across the junction was slowly increased, the frequency of the Josephson oscillation increased according to Eq. (3) until, at a voltage of 1.66 mV, this oscillation phase locked with the applied far infrared laser radiation at 805 GHz and produced a zero frequency beat current which is illustrated in the figure. As the voltage was increased further, the Josephson oscillation phase locked with the 891 GHz radiation at 1.84 mV and again produced a zero frequency beat, but this time of greater amplitude because of higher intensity radiation (larger V_1). In effect the junction acts as a spectrum analyzer of unusually large bandwidth. Our main interest however is in the result that the junction gives a large response at this extremely high frequency; in fact the magnitude of the response is

0.8 I_0. Considering this result, as well as other more extensive data (14), we conclude that the Josephson response is $\sim$ 70% of the upper bound of Eq. (5).

The principal frequency of this experiment, 891 GHz, is somewhat above the energy gap of 675 GHz of the superconductor (Nb) used in the experiment. Thus in an approximate way, considering the possible deleterious effects of shunt impedances, heating (15), and noise rounding (16, 15), we conclude that the Josephson effect operates at nearly full amplitude in the vicinity of the energy gap, a very high frequency for electronics. More generally it has been found experimentally that I_0 decreases above the gap frequency such that by approximately 12 times the gap it is no longer observable above the noise (12-14).

These high frequency experiments were done with point contact junctions to accommodate the far infrared radiation. Closely related experiments with tunnel junctions lead to the same conclusions (18,19).

Also consistent with the discussion given here is the study of self resonances in Josephson interferometers by Zappe and Landman (20). They conclude that the simple model of the Josephson effect is applicable up to frequencies at least as high as 300 GHz.

B. Time Domain Experiments

The early high frequency experiments with Josephson devices suggested their use as very fast logic switches. Matisoo (21) demonstrated this potential in the first important time domain experiment. This experiment placed an upper limit of 800 ps on the transition time of a Josephson tunnel junction for switching from the zero voltage state to the energy gap voltage. After many improvements in fabrication and testing, Jutzi (22) published data in 1972 which put an upper limit of 34 ps on the switching time of a small area junction with a critical current density of 1000 A/cm^2. The most recent published data for Josephson logic devices indicate switching times of about 7 ps and total logic delay of as little as 13 ps per gate (23).

The fact that Josephson devices can produce and detect these exceedingly fast signals gives them the potential for improving the state of the art in very fast waveform analysis. To understand how this might be done we can consider, as a first approximation, a Josephson junction to be a device which switches from zero voltage to the energy gap voltage V_g ($\sim$ 3 mV) at the instant its critical current is exceeded. This model is discussed more fully in Section IV. Since the transition is very rapid, a Josephson junction can act as a comparator to determine the <u>time</u> at which some threshold is crossed. Also, Josephson devices which operate in a latching mode can be used to detect and remember an extremely short excursion above an arbitrary threshold level. Both of these properties are used to measure the waveforms of repetitive analog signals.

Figure 2(a) shows one common way this is done (24-26). The unknown repetitive signal I_s, together with a bias current I_b, is applied to a tunnel junction J1. When the sum of these two currents exceeds the critical

current I_o of J1, it will switch causing a voltage transition to be transmitted to room temperature apparatus where its time of arrival is measured. Since the bias and the critical current of J1 are known, the signal level at the time the detector switches can be estimated. Thus, by measuring the delay in the J1 transition as a function of bias, rising edges on the signal may be mapped out. In practice this may be automated so that the unknown signal is traced out directly on an X-Y recorder. Hamilton, et al., (26) used this method to observe the risetime of a 4200 A/cm^2 junction adjacent to the sampler (see Fig. 2(b)). The two traces, recorded about one minute apart, are for increasing and decreasing bias. They are different because time drift in the room temperature electronics decreases the apparent risetime in one case and increases it in the other. Assuming constant time drift the correct risetime is the average or about 9 ps. This result represents the combination of the actual signal risetime and the time-jitter limited system response of about 7 ps. Simulations of this circuit show that there is a turn-on delay between the time that I_o is exceeded and the switching transition of J1. This turn-on delay depends on the degree of overdrive of J1, among other factors (see Section IV). When I_b is high, the overdrive is high and the turn-on delay is minimal. As I_b decreases the turn-on delay increases. The result is that signals observed with this technique are distorted, with the observed signal risetime being a few picoseconds greater than the actual risetime.

The character of the distortion of the signal is consistent with the theoretical turn-on delay formula Eq. (23). Whether the agreement is quantitatively accurate is impossible to say because of the amount of jitter present. In addition to the jitter problem this technique is further limited in that it can only observe rising edges of the signal.

Both of these limitations may be removed by another method (27, 28) depicted in Fig. 3. In this circuit the current through J1 is the sum of a dc bias I_{b1} and a fast ramp $I_r = \alpha t$. J1 will switch to the voltage state when $I_{b1} + I_r = I_{o1}$, producing a voltage transition at a time $T = (I_{o1}-I_{b1})/\alpha$. This voltage transition is differentiated by a capacitor C to produce a sampling pulse of maximum value I_{p1}. This pulse is applied to junction J2. J2 also receives current form the signal, $I_s(t)$, and a second bias source I_{b2}. The maximum values of I_s and I_{b2} are arranged so that I_{o2} can never be exceeded except at the instant of the sampling pulse. Thus if $I_{p1} + I_s(T) + I_{b2} > I_{o2}$, J2 will switch producing an output voltage $V_o = V_g$. If $I_{p1} + I_s(T) + I_{b2} < I_{o2}$ the output voltage is zero.

The output voltage, averaged over many repetitions of the signal, is compared with a value $V_g/2$ and the amplified difference is used to drive I_{b2}. This servo loop automatically adjusts I_{b2} to the threshold value where J2 is switching half the time and $I_{p1} + I_s(T) + I_{b2} = I_{o2}$. Since I_{p1}, I_{b2} and I_{o2} are known, the signal $I_s(T)$ is determined. The complete signal waveform may be recovered by sweeping I_{b1} and plotting the computed signal $(I_{o2} - I_{p1} - I_{b2})$ versus equivalent time $(I_{o1} - I_{b1})/\alpha$. Note that this circuit works in a repetitive mode where J1 and J2 are reset to the zero voltage state between each signal recurrence. The reset circuits are not shown in Fig. 3. In practice the sampling pulse may be created in several different ways and the detector junction J2 may be a Josephson interferometer. Faris (28) and Tuckerman (29) have used this principle in a general waveform sampling circuit with an estimated time resolution of 6 ps.

In order to produce an undistorted picture of the signal with this technique, the maximum value of $I_s(t) + I_{p1}$ must occur at the same time as the maximum of I_{p1}. Since I_{p1} is rounded on top, any variation of $I_s(t)$

across the rounded top of I_{p1} will cause the maxima not to coincide and thus lead to distortion in the observed signal. The magnitude of this distortion depends on the width of I_{p1} and the amplitude of $I_s(t)$ relative to I_{p1}. In practice this error can be reduced to a few picoseconds (28). A second source of distortion results from the finite response time of the detector junction J2. Discussion of this point will be left to Sections IV and V which consider in detail the dynamics of Josephson junctions used as latching detectors.

III. THEORETICAL BASIS

The design of circuits involving Josephson junctions is facilitated by the availability of accurate models for the junctions. The most commonly used model is a phenomenological description known as the RCSJ model, or resistively and capacitively shunted junction model first described by Stewart (3) and McCumber (4). Following a brief description of this model we discuss certain features of the more complex microscopic theory on which it is based. The microscopic theory is of practical importance because it provides a basis for testing the phenomenological model in areas that are experimentally difficult, such as the picosecond regime.

A. RCSJ Model

Stewart and McCumber used Eqs. (1) and (2) to describe supercurrent flow in a Josephson junction and added a resistive shunt to account for normal current at finite voltages. A capacitive shunt was also needed because of the physical nature of a tunnel junction. Their circuit model is illustrated in Fig. 4 (a). In order to encompass the idea of switching from the zero voltage state to the energy gap voltage V_g, the shunting resistance can be made voltage dependent, as illustrated in Fig. 4 (b). We designate this junction resistance as R_J.

If the RCSJ model is driven by a current souce I(t) the circuit equation for the case with no load conductance is:

$$I(t) = C_J\dot{V} + V R_J^{-1} + I_o \sin\phi \ . \qquad (6)$$

Much of the analysis to be discussed here will involve junction behavior at voltages below the energy gap, in which case $R_J = R_1$ (see Fig. 4 (b)). Restricting analysis to this region, one may write Eq. (6) in the form:

$$\frac{I(t)}{I_o} = \omega_p^2 (R_N C_J)^2 \frac{d^2\phi}{d\theta^2} + \frac{R_N}{R_1} \frac{d\phi}{d\theta} + \sin\phi, \qquad (7)$$

where R_N is the junction normal state resistance and ω_p is the plasma frequency (30):

$$\omega_p \equiv (I_o/C_J \bar{\phi}_o)^{1/2} , \qquad (8)$$

where $\bar{\phi}_o \equiv \hbar/2e$. The dimensionless time $\theta \equiv \frac{\pi}{2} \omega_g t$, $\omega_g = 2 I_o R_N/\pi\bar{\phi}_o$. Equation (7) contains the three time scales of a Josephson junction related to ω_p, $R_N C_J$, and to ω_g. We note incidentally that these time scales are not independent, in fact $\omega_p^2 R_N C_J = \omega_g$.

The ω_g time scale is based on the quantity $I_o R_N$. As will be seen later when discussing the microscopic theory of a Josephson junction, the quantity $I_o R_N = \pi\Delta/2e$ where Δ is the energy gap. Thus $I_o R_N$ is determined by a microscopic quantity and we shall therefore refer to θ as the microscopic time. On the other hand the quantities ω_p and $R_N C_J$ both depend on capacitance, or in other words, on the presence of a macroscopic dielectric layer, so we shall refer to the corresponding time scales as the macroscopic scales. These three time scales will be examined in more detail in the following two sections.

B. Microscopic Theory

Josephson, in his original work on superconducting tunneling (6), described the consequences of Eqs. (1) and (2). It remained for others to evaluate the theory for frequencies in the vicinity of the energy gap of the superconductors making up the junction. That was subsequently done by Riedel (1), and more completely by Werthamer (2), who were in turn followed by other significant contributors (31-34). Because the microscopic theory includes detailed effects which are not present in the phenomenological theory it is more complex and less straightforward to interpret. Here we will discuss only those aspects of the microscopic theory which are conceptually relevant to picosecond response. Further details are presented in Appendix A.

Initially the microscopic theory was presented in a frequency domain formulation. This theory describes only the tunneling current but the capacitive current can be added exactly as for the phenomenological model. The tunneling current is the sum of two currents: one of normal electrons called the quasiparticle current and described by $I_{qp}(\omega)$ and one of paired electrons called the supercurrent and described by $I_J(\omega)$. Although both I_{qp} and I_J have real and imaginary parts, which are all required for the complete theory, it is Im I_{qp} and Re I_J which provide the theoretical basis for the phenomenological theory. These functions are shown in Fig. 5. The junction critical current of the phenomenological model is the low frequency limit of Re I_J:

$$I_o = - \lim_{\omega \to 0} \text{Re } I_J(\omega) = \frac{\pi \Delta}{2eR_N} \quad , \tag{9}$$

The right hand equation is correct for superconductors with weak electron-phonon coupling but requires a correction factor for strongly coupled

materials (35, 36]. The frequency dependence of $I_J(\omega]$ is the frequency dependence of I_o, which was discussed in Section II. The peak in Re I_J at the energy gap describes an internal microscopic resonance called the Riedel peak which has been experimentally verified (18, 19].

The phenomenological resistive current VR_J^{-1} in Eq. (6) appears in the microscopic theory as Im $I_{qp}(\omega)$. When the full microscopic theory is used to calculate an I-V curve (37] the abrupt rise in Im $I_{qp}(\omega]$ of Fig. 5 occurs at a voltage $V = V_g \equiv 2\Delta/e$, the energy gap voltage. Thus the phenomenological resistive current is Im $I_{qp}(V)$. Indeed this function provides a highly accurate description of experimentally measured current-voltage characteristics (38).

In our later discussions the plasma frequency plays an important role. Physically this frequency represents the resonance between the junction capacitance C_J and the Josephson inductance which is derivable from Eqs. (1) and (2):

$$L_J \equiv \bar{\phi}_o/I_o \ . \tag{10}$$

In the context of the microscopic theory one should note first of all that the analog of I_o, i.e., $I_J(\omega]$, is frequency dependent so the inductance should also be frequency dependent. Secondly, $I_{qp}(\omega]$ has a reactive part which will affect the resonance. As will become especially clear when we discuss the theory of pulse detection, the plasma frequency is the natural frequency for small oscillations of junction voltage about the zero voltage state. Consequently we use small signal theory (34) to calculate the effective inductance in the microscopic model including the above effects, with the result:

$$\left[L_{eff}(\omega)\right]^{-1} = \frac{e}{\hbar} \text{ Re } \left\{ - [I_J(0) + I_J(\omega)] + [I_{qp}(0) - I_{qp}(\omega)] \right\} . \qquad (11)$$

In the limit as ω goes to zero the I_{qp} terms cancel and, using Eq. (9), L_{eff} becomes L_J of Eq. (10). If L_{eff} is evaluated at 0 K it is found that the singularity in Re $I_J(\omega)$ at the energy gap is canceled by a singularity in Re $I_{qp}(\omega)$ at the same frequency. L_{eff} increases monotonically from its minimum value L_J at $\omega = 0$, reaches a value of 1.57 L_J at the energy gap frequency, and asymptotically approaches a linear dependence on ω, $L_{eff} = L_J \hbar\omega/\Delta$. The increase of inductance with frequency simply means that the additional parallel resistive and capacitive current paths dominate the circuit at high frequencies.

Including high frequency effects the plasma frequency is given by $(L_{eff}C)^{-1/2}$. Therefore as C is reduced so as to make ω_p approach the energy gap frequency ω_g, one sees that L_{eff}, which is always $\geq L_J$, makes ω_p smaller than expected without high frequency corrections. This result has implications for the later discussion in Section V where it is found that the plasma frequency is directly related to the time resolution of superconducting circuits.

Returning to the general subject of the microscopic theory, we note that only a few evaluations of it have been made. These include detailed evaluations of (a) I-V curves as a function of $R_N C_J$ (37,39,40), (b) a proposed technique for producing picosecond pulses (41), and (c) the impulse response of a Josephson junction (42). Since the last reveals the microscopic limitations of the pulse response of junctions most clearly, we confine our attention to it here.

A Josephson junction, or any physical system for that matter, does not respond instantaneously to an applied stimulus. Delays arise from the interactions of electrons within the superconducting electrodes of a junction. These microscopic delays represent a fundamental limitation to device response.

To illustrate the intrinsic delay in a Josephson junction, R. E. Harris (42) has calculated the idealized impulse response of a hypothetical junction which has no capacitance. The calculation was based on a reformulation of the microscopic theory in the time domain which is discussed further in Appendix A. In this calculation the stimulus is a voltage pulse described as a delta function. The amplitude of the pulse is adjusted to produce a phase shift of $\pi/2$ in ϕ. The resulting current in the junction is illustrated in Fig. 6. The calculation reveals three significant aspects of the response. First the instantaneous response at time zero is linearly related to the driving voltage and is a result of the resistive nature of the I-V curve for large bias voltages. Second, after this response comes a rapid rise, on a time scale of $\hbar/2\Delta$ which is about 0.23 ps for the Pb alloy junctions we will discuss in the next section. This rise reveals the intrinsic response time of the junction. It is a very fast response, about a factor of 25 faster than any observed to date. As shown in Appendix A this delay arises from both the supercurrent I_J and the quasiparticle current I_{qp}. Third, at later times the current oscillates at the gap frequency $2\Delta/h$. This is just the appearance in the time domain of the previously-mentioned internal resonance named after Riedel. An important question is now apparent: how close can real devices, which suffer from macroscopic limitations, come to this limiting response time?

C. Macroscopic Junction Properties

Several intrinsic macroscopic parameters are needed for evaluating the behavior of real Josephson junctions. We will summarize the general formulas for these quantities and evaluate them for Pb alloy technology. Following that we return to a discussion of the macroscopic time scale suggested by the differential Eq. (7) of the RCSJ model.

The macroscopic properties of interest are the response time $R_N C_J$, the plasma frequency ω_p, the critical current density j_c, and the Josephson penetration depth λ_J, all of which are interrelated. These quantities are independent of junction area except for the plasma frequency, which is proportional to $(I_0/C_J)^{1/2}$, according to Eq. (8). This ratio is independent of area if the current density is uniform. Another point of interest, which we discuss in due course, is that the plasma frequency is maximized, for a given capacitance, if the current density is uniform. The Josephson penetration depth is a measure of the maximum size a junction can have and still retain uniform current density (43). Consequently we use Eq. (8) combined with Eq. (12) below to compute the plasma frequency with the priviso that the junction size not exceed λ_J by λ_J.

Basavaiah, Eldridge, and Matisoo (5) empirically related critical current density to tunneling barrier thickness d using the following relationship:

$$j_c = \frac{c_1}{d} \exp(-c_2 d), \tag{12}$$

where c_1 and c_2 are constants to be determined.

The next relationship of interest is between j_c and the junction normal state resistance R_N. For a junction using electrodes of identical superconductors at zero temperature we have

$$R_N = \frac{c_3}{A} \frac{\pi}{4} \frac{2\Delta}{j_c e} , \qquad (13)$$

where A is the junction area. This formula is similar to Eq. (9) but includes the strong coupling (29, 30) correction c_3. If $T > 0$, c_3 also includes a minor temperature correction. For dissimilar electrode materials we use an approximate expression obtained by replacing 2Δ with $\Delta_1 + \Delta_2$, rather than the exact but more complicated result of Ambegaokar and Baratoff (44).

Combining Eq. (13) with the usual expression for capacitance, $C = \varepsilon_r \varepsilon_o A/d$, the expression for $R_N C_J$ is obtained:

$$R_N C_J = \varepsilon_r \varepsilon_o c_3 \frac{\pi}{4e} \frac{2\Delta}{j_c d} . \qquad (14)$$

The Josephson penetration depth is given by:

$$\lambda_J^2 = \frac{\bar{\phi}_o}{\mu_o(\lambda_1 + \lambda_2 + d) j_c} , \qquad (15)$$

where μ_o is the magnetic permeability of vacuum, and λ_1 and λ_2 are the magnetic penetration depths of the base and upper superconducting electrodes of the Josephson junction.

For evaluation of the foregoing formulas, the constants c_1, c_2, c_3, Δ, ε_r, λ_1 and λ_2 must be determined. In general one would expect these constants to depend on the alloy composition of the base and upper electrodes of the junction and the details of the procedure for producing the tunneling barrier. Recent work of Greiner, Kircher, and Ames (45), and of Baker, Kircher, and Matthews (46) has begun to clarify what factors are important in the fabrication procedure. Unfortunately not all

of the material constants we need have been determined for the alloys of greatest interest (45) so we are forced to assume typical values taken from several different sources.

We begin with the constants in the relationship between j_c and d of Eq. (12). For this we use tunneling barrier data from the work of Eldridge and Matisoo (47) which used Pb-In alloy for the base electrode and Pb for the upper electrode. In this work the barrier is described in terms of various fractional concentrations of In and Pb in the oxide and we somewhat arbitrarily choose the data for 6.5% In and 93.5% Pb. Equation (12) has been fitted by a least squares procedure to this data to yield $c_1 = 2.207 \times 10^5$, $c_2 = 1.57872$ for d and j_c in units of nm and A/cm^2, respectively. With these constants Eq. (12) gives j_c to within 5% of the experimental data (40) over the range from 1 A/cm^2 to 1000 A/cm^2.

The dielectric constant of the tunneling barrier can be evaluated from the recent data of Gheewala (48). He reports a critical current of 50 μA for a junction with 2.5 μm diameter and 0.2 pF capacitance. Using the corresponding j_c of 1019 A/cm^2, the barrier thickness is evaluated from Eq. (12), and the dielectric constant $\epsilon_r = 12.7$ comes immediately from the standard capacitance formula. (Note that this value of ϵ_r is obtained by combining data for two different alloy systems and consequently has considerable, but unknown, uncertainty associated with it.) A working rule of thumb for capacitance is 4 pF per mA of critical current at 1000 A/cm^2.

An I-V curve for the most recent alloy system of Greiner, et al. (45) allows the evaluation of additional constants. From the voltage of the

steep rise of the quasiparticle current, our own data gives $2\Delta/e = 2.9$ mV. For a critical current of 0.177 mA we measure a normal state resistance $R_N = 8.0\ \Omega$, which from Eq. (14) gives a value of $c_3 = 0.62$. Values of the magnetic penetration depths are taken from ref. (45): $\lambda_1 = 137$ nm, $\lambda_2 = 202$ nm.

These constants allow computation of the graphs shown in Fig. 7. It should be understood that these graphs are only approximate since they are based on data from more than one alloy system. Nevertheless we take them to be representative of the properties of Pb alloy junctions and find them to be useful for design analysis.

Most of the detailed analysis in subsequent sections involves junction behavior at voltages below the steep rise of the quasiparticle current at the energy gap. For this case the appropriate RC time is not $R_N C_J$ but rather $R_1 C_J$, where R_1 is the resistance below the energy gap of Fig. 4 (b). Thus to obtain the physical RC time the graphical data for $R_N C_J$ of Fig. 7 must be multiplied by R_1/R_N, a number which depends on the fabrication process. For example, in our laboratory R_1/R_N was typically 5 when a PbAu upper electrode was used but a PbBi upper electrode at the present time gives a representative value of 17.

Using data from Fig. 7 one can readily establish that the quantity $\omega_p R_1 C_J >> 1$ for the entire range of the figure. That means that junctions operating in the subgap resistance region have plasma oscillations that are only lightly damped, a fact that has significant consequences in the study of pulse coincidences in a detector in Section V.

We observe from Fig. 7 that $R_N C_J$ and ω_p refer to substantially different numerical time scales. Consequently we must consider which is physically more important.

In the RCSJ model, Fig. 4 (a), there are three parallel current paths, namely those through R_1, C_J, and the Josephson inductance L_J given by Eq. (10). For effective high speed action of a Josephson junction in a switching circuit L_J must not be heavily shunted by R_1 or C_J. The plasma frequency, by definition, is the frequency above which the impedance of C_J is less than that of L_J. Using the graphical data of Fig. 7 it can readily be determined that at the plasma frequency the capacitance heavily shunts R_1. Thus R_1 plays only a small role in the high speed dynamics. From these considerations it becomes clear that ω_p and not $R_N C_J$ should be the basis for the physically more important time scale for Josephson junctions without external shunts of low impedance.

Earlier we found the microscopic response time of a Pb alloy junction to be $\hbar/2\Delta = 0.23$ ps. The corresponding limiting macroscopic time is approximately $\tau_p \equiv 2\pi/\omega_p$. In order to have the macroscopic and microscopic response times approximately equal, we find that the plasma frequency must be approximately equal to the energy gap frequency $\omega_g \equiv 2\Delta/\hbar$. In this regime the RCSJ model has inaccuracies of about 30% which we will largely ignore. More importantly we note that the current density required for such a high ω_p would be well in excess of 10^5 A/cm^2 for Pb alloy technology. Such high j_c means that nonequilibrium and self heating effects would be significant. Even though current densities in excess of 10^5 A/cm^2 have been achieved (49), little is known about the dynamical properties of such junctions. Consequently, it must be left as an open question whether or not the macroscopic and microscopic speeds can be made comparable.

An example of what <u>is</u> achieveable comes from the work of Broom, Jutzi, and Mohr who used junctions with current densities of 28000

A/cm^2 in a memory cell (50). Heating effects were sufficiently large in this case that the I-V curve was traced by a pulsed method to reduce errors from self heating of the junction. Taking this example as a rough estimate of the maximum j_c that is practical without using extra thick electrodes or special substrates (51), Fig. 7 gives the corresponding $\omega_p = 3 \times 10^{+12}\ s^{-1}$. This is a factor of ten below the plasma frequency needed to make the macroscopic and microscopic response times equal.

IV. Switching Time

The switching time of a junction from the zero voltage state to the energy gap voltage divides roughly into two parts, a turn-on delay time during which the voltage remains small, and a rise time during which the voltage is rapidly increasing, as illustrated in Fig. 9. The analysis of these given here is based on the RCSJ model. For the period during which the voltage remains below the gap voltage, one may use Eq. (6) with R_J replaced by R where R is the parallel combination of the subgap resistance R_1 and a possible load resistance R_L. Setting $I(t) = I_b(t)$ in Eq. (6), we note that if $I_b(t)$ changes sufficiently slowly then Eq. (6) can be written in the form of an energy equation

$$\frac{d}{dt}(T + V) = -\frac{\dot{\phi}^2}{RC_J}, \tag{16}$$

where the kinetic and potential energies, T and V, are respectively $T = \frac{1}{2}\dot{\phi}^2$ and

$$V = -\omega_p^2 (\cos\phi + (I_b/I_o)\,\phi) . \tag{17}$$

These equations suggest the helpful analogy of a particle of unit mass subject to a viscous retarding force, sliding down a potential energy "washboard'. Figure 8 illustrates the potential energy as a function of ϕ and I_b. Clearly there is no stable position for the particle if $I_b > I_o$. Consideration of the washboard picture helps one to understand qualitatively many features of the RCSJ model, including the switching behavior of a junction. For example, the particle initially moves slowly

until the downward curvature of the potential is reached. This corresponds to the turn-on delay period, which was first discussed by E. P. Harris (52). Subsequently the particle accelerates until either its terminal velocity is reached, corresponding to a voltage I_bR, or the velocity corresponding to the gap voltage is reached. This defines the rise time of the switching process. Figure 9 shows a simulation which illustrates this behavior. We will develop formulas for the turn-on delay τ_D and the rise time τ_R for lightly and moderately loaded circuits. The sum of these is the approximate switching time.

A. Turn-on Delay of a Josephson Junction

Suppose that the current $I_b(t)$ is increased slowly from zero so that the junction phase ϕ will be about $\pi/2$ when I_b reaches I_o. At that point I_b is then abruptly stepped to $I_o(1 + \delta_o)$ where δ_o is the fractional overdrive. This is a bit artificial in that in practice I_b typically ramps up through I_o at a finite rate. One technique which approximates this case is that in which a junction is biased at a constant current below I_o, and then triggered by a current pulse resulting from the switching of another junction, as discussed in Section II.B. We will shortly generalize to the case where the initial I_b is below I_o. The effects of a finite ramp rate will, however, not be taken up here.

In Eq. (6) we thus use $I_b = I_o\ (1 + \delta_o)$ for $t > 0$, and have $\phi(0)=\pi/2$. We set $\sin\phi$ equal to unity and consider the evolution of V until ϕ advances by one-half radian. The supercurrent term is in error by just 12% at the end of this period, so that the estimated time for ϕ to get to $\pi/2 + 1/2$ is quite accurate. Fortunately, $\phi = \pi/2 + 1/2$ is also about the place where $\dot{\phi}$ begins increasing significantly, as simulations show. We thus take this time as an estimation to τ_D. From Eq. (6) we then easily obtain, provided $\tau_D << RC_J$,

$$\tau_D = \omega_p^{-1} \delta_o^{-1/2}, \qquad (18)$$

where ω_p is given in Eq. (8).

E. P. Harris (52) has published an expression for the turn-on delay time for this case. He approximated $\sin\phi$ by the first two terms in its Taylor expansion, integrated the resulting expression exactly in terms of elliptic integrals, and approximated the latter by simpler functions. From this result he calculated the time required for the phase to advance to $3\pi/2$. He subtracted from this the time required for the phase to advance the same amount if only the junction capacitance were being charged. His result, again for $\tau_D << RC_J$, is

$$\tau_D = \frac{1}{\omega_p} \left[\frac{2.61}{\delta_o^{1/4}} \tan^{-1} \left(\frac{1.13}{\delta_o^{1/4}} \right) - \left(\frac{2\pi}{1+\delta_o} \right)^{1/2} \right]. \qquad (19)$$

Figure 10 compares Eqs. (18) and (19). Also shown are values of τ_D taken from numerical simulations. The latter have been determined by extrapolating the rise time portion of the curve down to the time axis. Typically there is a few-percent uncertainty in this, both because of the superimposed Josephson oscillations, and because the rising portion is not a straight line even with the oscillations removed. The points shown in Fig. 10 were determined from the midpoint of two straight lines drawn tangent to the first two maxima and minima, as shown in Fig. 9.

As is seen in Fig. 10, Eq. (18) is more accurate than Eq. (19) in the region of about 1-50% overdrive. Outside this region, Harris' expression is more accurate. Thus, from 1-50% overdrive, Eq. (18) would

be preferred for reasons of both accuracy and simplicity. Below 1%, turn-on delay becomes a more serious problem, and one may prefer to use Eq. (19); the simple formula overestimates τ_D there. Above about 50%, τ_D is typically very small compared to the risetime and therefore of decreased significance.

Now we remove the restriction that I_b is initally at I_o. Let $I_b(t < 0) \equiv I_{bi} \leq I_o$, and $\phi(0) \equiv \phi_i = \sin^{-1}(I_{bi}/I_o)$. There are two new effects to consider now. One is that the particle in the washboard model must travel a longer distance if the same "final" position is used to define the delay time. The other is that the initial potential energy is now greater, giving the particle more velocity after the step, thus decreasing the delay time. This is illustrated in Fig. 8 (b). The latter effect usually dominates.

We write $I_{bi} = I_o\ (1 - \delta_i)$ and $I_b\ (t > 0) = I_o\ (1 + \delta_o)$ where $\delta_i \geq 0$ and $\delta_o > 0$. Our procedure is, in effect, to approximate $\sin\phi$ by its initial value and to drop the damping term V/R from Eq. (16), which thus gives a constant acceleration to the system particle and an easy determination of τ_D. Lest this seem too crude, we shall show that the same result is obtained by expanding $\sin\phi$ through the term linear term in $\phi - \phi_i$, followed by some usually excellent approximations and the assumption that $\tau_D << RC_J$ as in the preceding case. When $\sin\phi$ is thus expanded, the potential energy of Eq. (17) is changed to a typically shallow parabola. Equation (6) then describes a damped harmonic oscillator:

$$I_o(1+\delta_o) = C_J\dot{V} + V/R + I_o\sin\phi_i + (\phi - \phi_i)I_o\cos\phi_i. \qquad (20)$$

This has the solution

$$\phi(t>0) = \phi_i + \frac{\delta_o + \delta_i}{\cos\phi_i}\left[1-e^{-t/2RC_J}(\cos\omega t + (2\omega RC_J)^{-1}\sin\omega t)\right], \quad (21)$$

where

$$\omega = (4R^2C_J^2\omega_p^2\cos\phi_i - 1)^{1/2}/2RC_J = \omega_p(\cos\phi_i)^{1/2}. \quad (22)$$

Thus ω is essentially the phase-dependent plasma frequency. The approximate equality in Eq. (22) is quite typically valid: If we take V_g/I_o as a minimum value for R (to ensure switching to the gap), the condition for the validity of the approximate equality is $\cos\phi_i >> \bar{\phi}_o I_o/4C_J V_g^2$. For the junction of Fig. 9 this becomes $\cos\phi_i >> 10^{-3}$, or $\delta_i >> 10^{-6}$. Clearly, R may be considerably less than V_g/I_o, as in high speed latching logic, without practically invalidating the approximation of Eq. (22).

The coefficient of sin ωt in Eq. (21) is very small under the same condition. Thus the initial motion of ϕ results principally from the cos ωt term. Expanding cos $\omega t = 1 - (\omega t)^2/2$, and defining τ_D as the time at which ϕ reaches $\pi/2 + 1/2$, as before, we find

$$\tau_D = \frac{1}{\omega_p}\left[\frac{1 + 2(\pi/2 - \phi_i)}{\delta_o + \delta_i}\right]^{1/2}. \quad (23)$$

This is a simple generalization of Eq. (18) to which it reduces as I_{bi} goes to I_o. Unless ϕ_i is far from $\pi/2$, the numerator is not very sensitive to the precise value of δ_i, but the denominator can be very sensitive to δ_i, confirming our earlier remarks concerning the relative effects of the initial position and potential energy.

Equation (23) underestimates the delay time for small overdrives, as determined from simulations. The reason is that the approximations

used in the above analysis are equivalent to taking the acceleration of ϕ as unchanged from its initial value during the motion. For $\delta_f = 0.1$, the result of Eq. (23) for the junction of Fig. 9 is about 30% low for $\delta_o = 0.01$, correct for δ_o about 0.2, and progressively too high beyond that. It is not difficult to refine the approximation at the expense of a more complicated formula. However, since different methods for defining τ_D can give values differing by several percent, and since one is ordinarily only interested in estimating τ_D, the estimate of Eq. (23) is surely adequate for most purposes.

Thus, in summary, the total size of the step rather than just the amount of overdrive is the important quantity in the turn-on delay resulting from a step increase in I_b. Further, τ_D is modified by the initial phase.

Discussions of the turn-on delays in single-junction and two-junction SQUIDs are given in Appendices B and C.

B. Rise Time

The rise time τ_R refers to the time duration of the rapidly rising portion of the switching transition illustrated in Fig. 9. We shall show that the rise time of the RCSJ model is approximately $R_N C_J$ where R_N is the normal state resistance of the junction. Although this result is widely known, it is often misquoted. It needs to be emphasized that the resistance here, R_N, is <u>not</u> the actual resistance R shunting the junction.

During the steep rise of the transition the $\sin\phi$ term of Eq. (6) is rapidly oscillating so that the current $I_o \sin\phi$ averages nearly to zero. Equation (6) with the $\sin\phi$ term neglected describes the charging of the junction capacitance. The solution to this equation is

$$V(t) = I_b R[1-\exp(-t/RC_J)], \tag{24}$$

if the bias current has the value I_b which does not change significantly during the rapid rise. We choose $t = 0$ as the time when the significant acceleration begins. If $I_b R$ is less than the gap voltage V_g, the voltage rises only to $I_b R$ with time constant RC_J. However, if V_g is less than $I_b R$, the risetime τ_R at which the gap is reached is

$$\tau_R = -RC_J \ln(1-V_g/I_b R). \tag{25}$$

If, moreover, $V_g << I_b R$ we see that

$$\tau_R = \frac{C_J V_g}{I_b} = \frac{4}{\pi} R_N C_J \frac{I_o}{I_b}, \tag{26}$$

where we have used the relation $V_g = 4I_o R_N/\pi$ from Eq. (9). Thus

if $I_b \sim I_o$ and $V_g << \mathbb{O}_o R$, the 10-90% risetime will be close to $R_N C_J$. This may be verified in Fig. 9. For strong coupling superconductors, the 10-90% risetime will be somewhat longer than $R_N C_J$.

V. Pulse Generation, Detection, and Measurement

In this section we adopt the primitive view that pulses have only two characteristics of interest, a height and a width. As a reasonable approximation to practical pulses we use the Gaussian pulse shape for most of the analysis. The main problem of interest is to develop the concepts needed for measurements of pulses that are available on a repeating basis.

A. Pulse Generators

Probably the simplest means of producing pulses in superconducting electronics is the circuit of Fig. 2 (a). The junction J1 is assumed to be initially in the zero voltage state with $I_s(t) + I_b < I_o$. The switching transition of the hysteretic junction J1 occurs very shortly after $I_s(t)$ exceeds $I_o - I_b$. The resulting increased impedance of J1 diverts the bias current down the transmission line producing the rising edge of the pulse. If the shunt impedance across the junction is low enough (53) the junction will not stay in the switched position, i.e., it will not latch, but will go back to the zero voltage state producing the trailing edge of the pulse.

A related technique for producing especially narrow pulses is to pass the rising edge of the switching transition through a differentiating network, as indicated for example as part of Fig. 3.

Faris (28) and Tuckerman (29) have recently demonstrated a pulse generator, based on a SQUID interacting with another junction, which produced 12 ps wide pulses.

Several years ago Peterson and McDonald (54) proposed a conceptually different form of pulse generator based on a Josephson junction driven only by a microwave current source and loaded by a shunt resistor. In this circuit the junction may be either hysteretic or nonhysteretic without changing the qualitative behavior of the circuit. A train of alternating positive and negative pulses is produced when the drive current amplitude just exceeds I_o and encounters a strong nonlinearity. One cycle of the pulse train is shown in Fig. 11. This design is notable in part because it has been analyzed using the microscopic theory of junctions (35) to calculate the resulting pulse widths. A comparison of the waveforms calculated using the microscopic theory and the RCSJ model is one of the few benchmark comparisons between the two theories. The differences between the waveforms are approximately 15% for pulse widths of 4.7 ps and about 35% for the narrowest pulse widths of 0.8 ps.

The original analysis did not consider the details of pulse detection and measurement. The need to understand these processes provided the primary motivation for the analysis which follows. In all of the simulations which follow, the affects that would arise in practice from parasitic inductance and finite source and load impedances are neglected. The goal is to describe the main qualitative features of pulse interactions with detectors.

B. Pulse Detectors

The elementary problem considered here is represented in Fig. 13 (a), in which a current source $I_p(t)$ provides a single pulse to a Josephson junction detector, and a current source I_b provides dc bias. We then ask under what circumstances does the junction voltage V switch from zero to the energy gap voltage. The basis for our analysis is Eq. (6) with the driving current $I(t) = I_p(t) + I_b$.

If the pulse risetime is slow enough, the detector will switch as soon as $I_p(t) + I_b = I_o$, assuming

$I_b < I_o$. However, if the pulse risetime is too fast or if the pulse width is too narrow, large deviations from this limiting case are suggested by the qualitative ideas of the washboard model. The emphasis in the present discussion will be on determining the minimum value of I_b for which switching occurs, i.e., the threshold condition, with a particular pulse amplitude and pulse width. In a subsequent section the measurement of pulse width is explored.

Initially we consider simulations in which the applied pulse has a Gaussian shape described as:

$$i_p(t) = i_{pl} \exp\left\{-(4\ell n2)\left(\frac{t-t_o}{W}\right)^2\right\}, \qquad (27)$$

where $i_p(t) \equiv I_p(t)/I_o$, $i_{pl} \equiv I_{pl}/I_o$, t_o is the time of arrival of the center of the pulse at the detector, and W is the full width of the pulse at a current level of $\frac{1}{2}\, i_{pl}$.

Figure 12 is a composite illustration of the calculated responses of a detector junction to pulses of four different widths. The driving pulses are shown in the first row of illustrations. The junction properties and the pulse amplitudes, $i_{pl} = 0.5$, are the same for all cases. Various junction responses are shown for biases i_b just below and just above threshold for switching. Although both bias levels are very close to threshold, the corresponding graphs qualitatively represent the general behavior for any values of i_b below and above threshold, respectively.

In the second row of illustrations it is seen that for i_b below threshold the voltage stays near zero and undergoes damped plasma oscillations after excitation by the applied current pulse. For i_b

above threshold the voltage rises rapidly from zero to the energy gap value V_g. Josephson oscillations driven by V_g are evident after the junctions switch in all cases, but the time scale is too coarse for their resolution in the two left-most illustrations of this group. These figures clearly illustrate why a Josephson junction is useful as a pulse detector: The device permanently changes its voltage state after the passage of a brief transient event if the pulse height, pulse width, and bias have the proper relationship. Of course this is much the same as the operation of a Josephson latching logic gate.

In the third row of Fig. 12 the time dependence of the phase ϕ of the junction is shown for each of the four driving pulse widths. For the curves corresponding to bias values below threshold, the phase is driven to some maximum positive value by the applied pulse and then undergoes damped plasma oscillations in returning to its equilibrium position. The plasma oscillations, which seem like an unimportant detail, assume major importance when we consider the detection of pulse coincidences in a later section. An extensive numerical study of the phase supports the general idea that a junction will switch if the phase reaches a certain universal critical value. Thus if one could watch the evolution of the phase in time using this critical phase idea, one would know well in advance whether or not the voltage was committed to a trajectory to V_g. The critical phase is $\pi-\phi_b$, where ϕ_b is the phase due to the steady bias:

$$\phi_b = \sin^{-1} i_b. \tag{28}$$

This idea is central to the detailed models that will be used to analyze threshold switching conditions. Zappe has used a similar argument when analyzing response to a current step (53). We note that the critical phase idea originates from considerations with ideal pulses. If a pulse is complex, i.e., if it goes alternately both positive and negative for example, the critical phase idea may not apply. This is only to say that the direction of motion of a pendulum can always be reversed regardless of its position relative to a critical angle.

The switching process for pulse detectors involves a turn-on delay and a rise time which are qualitatively the same as discussed in Section IV. These delays are particularly evident for the switching transition of Fig. 12 (k), the simulation with the narrowest driving pulse. The formulas given in Section IV for the turn-on delay are derived for the case in which the applied current remains at a constant level above the critical current, thus continually feeding energy into the system and shortening the turn-on delay. Turn-on delay expressions for the pulsed case can be derived. However, they are not simple and we will not present them here.

In summary Fig. 12 illustrates the behavior of the detector biased near threshold for a variety of pulse widths. The relationship between pulse height, pulse width, threshold bias, and the properties of the detector junction will now be analyzed by considering three different cases: (1) Static Limit, (2) Impulse Approximation, and (3) Square Pulse Approximation.

1. Static Limit

This limit applies to very broad pulses, broad in comparison with a junction plasma period $\tau_p \equiv 2\pi/\omega_p$. With the pulse current rising

sufficiently slowly it is obvious that the junction will switch very soon after $i_p(t) + i_b$ exceeds unity. The pendulum analog (55) provides a simple interpretation for this case. This analog is based on the observation that the differential equation for the angle of deflection of a simple pendulum is similar to Eq. (7) for the phase of a Josephson junction if one makes a suitable identification of the analogous variables. The torque τ_b, analogous to the

driving current, is balanced by gravitational torque so that the bias angle ϕ_b in the analogous cases is:

$$\phi_b = \sin^{-1}\left(\frac{\tau_b}{mg\ell}\right) = \sin^{-1} i_b. \qquad (29)$$

where mg is the gravitational force on the pendulum of length ℓ. Since the torque required to hold the pendulum statically at angle ϕ_b is proportional to $\sin\phi_b$, it is clear that the torque increases for angles from zero up to $\pi/2$ and then decreases for larger angles. Thus for any torque $\tau_b < mg\ell$ there are two angular positions where that torque can hold the pendulum: ϕ_b and $\pi-\phi_b$. However the upper position is unstable and random fluctuations in position will cause the pendulum to go "over the top". Thus our hypothesis is that if the pendulum can ever reach $\pi - \phi_b$, the mirror image position of ϕ_b for reflection in a horizontal plane, then continuous rotation of the pendulum will be initiated (assuming no damping), which is analogous to switching to the energy gap in a Josephson junction.

In the static limit the V and $\dot{V}$ terms (which are equivalent to $\dot{\phi}$ and $\ddot{\phi}$ terms) in Eq. (6) are negligible. An examination of this equation leads to the conclusion that in the static limit the critical angle idea has a special twist. It becomes obvious that in order for a slow pulse to carry the pendulum to the mirror position with the lowest possible (threshold) bias level, the pendulum must reach $\phi = \pi/2$ in coincidence with the pulse maximum.

The simulations in the first column of Fig. 12, with a pulse width of 324 ps, are close to the static limit. Threshold bias is between the two

illustrated bias levels of 0.500214 and 0.500215. Thus we see immediately that the threshold bias $i_b(Th)$ is very near the simple relation $i_b(Th) + i_{pl} = 1$, since $i_{pl} = 0.5$.

2. Impulse Approximation

Another limiting case which can be evaluated in detail is for extremely narrow pulses, the impulse approximation. In this case the current very rapidly rises and falls back to i_b before the junction can respond. All of the charge q_p in the impulse goes onto the capacitor, charging it to voltage V_m and providing an amount of energy $\frac{1}{2}C_J V_m^2$ for driving the system.

$$q_p = \int_{-\infty}^{\infty} I_p(t)dt = C_J V_m. \qquad (30)$$

In the pendulum analog an impulse of torque is applied but it is over before the pendulum has time to move. In the limiting case the pendulum undergoes a step-function change in angular velocity. Based on our previous discussion of the analog, which ignores dissipation, we see that the system will go into a state of steady rotation if the impulse causes the pendulum to reach the mirror image position.

Another source of energy is the bias supply. To calculate this energy, it is appropriate to integrate from the initial phase ϕ_b to the phase of the image position $\pi - \phi_b$:

$$\int_{\phi_b}^{\pi-\phi_b} I_b \; V(t)\, dt = \bar{\phi}_o I_b \int_{\phi_b}^{\pi-\phi_b} d\phi = \bar{\phi}_o \, I_b(\pi - 2\phi_b). \quad (31)$$

The only other energy in the system is the analog of the potential energy of the pendulum (42), which is given by: $-\bar{\phi}_o \, I_o \cos\phi$. As the pendulum is raised the potential energy continuously increases. The change in potential energy between ϕ_b and $\pi-\phi_b$ is $2\bar{\phi}_o I_o \cos\phi_b$.

Ignoring dissipation, conservation of energy requires that the energy in the impulse plus the energy supplied by the bias equals the change in potential energy:

$$\frac{1}{2} \frac{q_p^2}{C_J} + \bar{\phi}_o \, I_b(Th)\{\pi - 2\phi_b(Th)\} = 2\bar{\phi}_o \; I_o \cos\phi_b(Th), \quad (32)$$

at threshold.

For a Gaussian pulse described by Eq. (27):

$$q_p = 1.064\ i_{pl} W \tag{33}$$

Combining (32) and (33) and changing to reduced variables gives:

$$i_{pl}^2 = \frac{1.767}{\omega_p^2 W^2} \left\{ 2\cos\phi_b(Th) - i_b(Th)\left[\pi - 2\phi_b(Th)\right] \right\} . \tag{34}$$

This is the desired relationship between pulse height i_{pl} and bias at threshold $i_b(Th)$ for a narrow pulse of width W. A clearer idea of what "narrow" pulse means will be obtained by comparing this formula with detailed simulations.

Figures 12 (j) - (ℓ) illustrate an example calculation for which the impulse approximation is reasonably accurate. For this case the pulse width $W = 0.063\ \tau_p = 0.324$ ps, and the pulse height $i_{pl} = 0.5$. Figure 12 (k) illustrates the time dependence of the detector voltage for biases of 0.95527 and 0.95528, which are just below and just above threshold.

Setting $i_b(Th) = 0.95528$, the value for i_{pl} at threshold can be calculated from the impulse approximation formula, Eq. (34). The result is $i_{pl} = 0.4505$, which is about 10% off the simulation value of 0.5.

This simulation differs from the static limit in that the sum $i_b(Th) + i_{pl} = 1.455$ instead of simply 1. Greater variations of the sum $(i_b + i_{pl})_{Th}$ are found if i_b is held fixed and the threshold pulse height is evaluated. The required pulse height diverges as W^{-1}, according to Eq. (34).

A physically more interesting difference from the static limit is illustrated in Fig. 12 (a) where the time development of the phase is shown. For i_b just barely below threshold, ϕ advances to a maximum of 1.865 radians and then falls back and undergoes damped plasma oscillations. The maximum advance of the phase is very close to the image position $\pi - \phi_b$ = 1.872 radians, validating the physical significance of that position.

The plasma oscillations are much more evident below threshold in the impulse limit than in the static limit, Fig. 12 (c). This behavior is readily understood from a Fourier analysis of the two different input pulses. The bandwidth of the pulses (defined as the frequency at which the frequency distribution has fallen to 1/2 its maximum value) is:

$$f_{1/2} = \frac{2\ell n 2}{\pi W} . \tag{35}$$

In approximating the static limit we had W = 324 ps, implying $f_{1/2}$ = 1.36 GHz. The pulse used in the impulse limit has W = 0.324 ps, and $f_{1/2}$ = 1360 GHz. For both of these simulations, which differ only in the applied pulse width, the plasma frequency is 194 GHz. Comparing the two values of $f_{1/2}$ with the plasma frequency it is obvious that the wide pulse has very little energy available for exciting plasma oscillations, whereas, in the narrow pulse case the plasma frequency is well inside the bandwidth of the pulse so substantial energy is available. Excitation of plasma oscillations takes on much greater importance when we deal with pulse width measurements in the next section, so it is important to understand what produces them.

3. Square Pulse Approximation

The static limit and the impulse approximation leave the intermediate cases unevaluated on a quantitative basis. To obtain workable formulas for these cases it is necessary to relinquish the Gaussian description of the pulse in favor of a simpler pulse shape. Dhong and Van Duzer (56) have shown that analytical results for threshold conditions with arbitrary pulse widths can be obtained if the driving pulse has vertical sides and square corners. For describing this pulse we use the same notation as for the Gaussian pulse, i.e., it has a maximum current, normalized to I_o, of i_{pl} and a width W. In this calculation the system is initially assumed to be dissipationless but a correction is made for that later. Using the washboard model, described earlier, and energy conservation, the phase ϕ_W which must be reached by the end of the square pulse in order to have continuing movement down the washboard is:

$$\phi_W = \frac{-\pi i_b + (2i_b + i_{pi})\phi_b + 2\cos\phi_b}{i_{pl}} . \qquad (36)$$

Using a linearized $\sin\phi$ term, expanded about ϕ_b, the differential equation (6), with $I(t) = I_p(t) + I_b$, can be solved for the time dependence of the phase during the pulse:

$$\phi = -\left(\frac{i_{pl}}{\cos\phi_b}\right) \cos\omega_p' t + \left(\frac{i_{pl}}{\cos\phi_b} + \phi_b\right), \quad 0 < t \leq W , \quad (37)$$

where $\omega_p' \equiv \omega \sqrt{\cos\phi_b}$. ($\omega_p'$ is a generalization of the plasma frequency ω_p explicitly includes the phase dependence of the effective inductance of a Josephson junction). Solving Eq. (37) for t and then setting $t = W$ so that $\phi = \phi_W$ yields:

$$W = \frac{2}{\omega_p'} \sin^{-1} \sqrt{\frac{(\phi_W - \phi_b)}{2i_{pl}} \cos\phi_b} , \qquad (38)$$

Combining the threshold relationship Eq. (36) with Eq. (38) allows the calculation of the pulse width W at threshold for a given bias and pulse height, assuming no damping.

Including a correction for damping, Dhong and Van Duzer [56] obtained the following expression for the pulse width at threshold:

$$W' = W + \frac{\bar{\phi}_o(\phi_W - \phi_b)}{I_o R_1(-i_b + \sin\phi_W)} \cdot \tag{39}$$

This relationship has been evaluated for a number of values of pulse width with fixed pulse height $i_{p1} = 0.5$. The results are displayed in Fig. 13 along with several data points from an evaluation of the impulse approximation formula, Eq. (34). In the figure these points are to be compared with the results of circuit simulations represented by the solid line.

The square pulse approximation predicts the threshold current to an accuracy of 10% or better, as compared with the simulations, over the pulse width range $0.09\ \tau_g < W < 0.5\ \tau_g$. This approximation diverges from the simulations for small pulse widths because the correction term for dissipation becomes comparable to W. For large pulse widths it diverges from the simulations because the linearization of $\sin\phi$ becomes inaccurate. The impulse approximation is comparably accurate for $W < .25\ \tau_g$. One caution that should be observed is that the RCSJ model is not expected to be very accurate for pulse widths of the order of 1 ps or less, the regime where the microscopic frequency dependence of the superconducting response becomes significant. In a related problem [41] for which comparisons with the microscopic model were made for an 0.8 ps pulse width, the differences between the models were about 35%.

The most important general conclusion from Fig. 13 is the observation that the static limit is a good approximation for pulse widths greater than

or equal to one plasma period, i.e., for $W \geq \tau_p \equiv 2\pi/\omega_p$ In this region the Josephson pulse detector is linear, by which we mean that at threshold a change in i_{pl} can be compensated for by an equal but opposite change in i_b following the relationship $(i_b + i_{pl})_{Th} = 1$. In the next section we argue that τ_p, and therefore the minimum pulse width for linear detection, can be as small as 2.1 ps. For narrower pulses nonlinear threshold conditions apply as described by Eq. (39) for intermediate pulse widths and Eq. (34) for the narrowest pulses.

B. Pulse Width Determination

The Josephson pulse detector described in the preceding section is a very simple device. Given such a device one can measure its critical current density and from that infer its $R_N C_J$ and ω_p from Fig. 7. However, if this detector is used to detect pulses of unknown width and amplitude, what can be learned about the pulses? About all one can measure is the bias threshold for detection of the pulses, but that tells very little about them since the switching may be due to wide pulses of relatively low amplitude or from narrower pulses of higher amplitude. Knowledge of the detector response time does not change the situation. However if the pulse width could be measured, the pulse amplitude could be inferred.

Before describing a technique for pulse width measurement, it is instructive to consider a hypothetical situation in which two triangular shaped current pulses are applied to an ideal threshold detector. For simplicity the widths W and the amplitudes I_{pl} of the two pulses are equal. Figure 14 (a) is a plot of current in the detector as a function of time for a particular delay τ between the centers of the pulses. The idealized detector is a device which instantly switches the state of its output terminals (and remains switched) if an adjustable current level I_d is exceeded at its input terminals. Consider the input to the detector to be repeatable and the detector to be resettable so that one can experimentally determine, for a given τ, the maximum value of I_d for which threshold is crossed by the input signal.

The result of such an idealized experiment is shown in Fig. 14 (b). If the pulses are well separated in time the maximum value of I_d for detection, $I_d(Th)$, is equal to I_{pl}. As τ is decreased the pulses begin to overlap but $I_d(Th)$ does not change until one pulse begins to overlap the center of the other pulse. The maximum value of $I_d(Th)$ is $2I_{pl}$ and occurs for $\tau = 0$. The result of this idealized experiment is an image of one of the pulses in the $I_d(Th)$ vs. τ plot. The image pulse has an offset baseline but the pulse shape is unchanged.

The scheme for using Josephson junctions for pulse width measurements is similar to the idealized case just described but there are significant differences. The idealized device is linear in that a change in the bias I_d produces an exactly equal change in the current required to reach threshold. For a Josephson junction, that is true only in the static limit. In both the square pulse approximation Eq. (39) and the impulse approximation Eq. (34) the relationships between I_b and I_{pl} at threshold are nonlinear. With the idealized detector the fidelity of the image of the driving pulse is a result of the linearity of the detector. With a nonlinear detector distortion in the pulse image can be expected.

Our investigations of this procedure are limited to a circuit like the pulse detection circuit of Fig. 13 with the addition of a second Gaussian pulse source. We confine our attention to calculating the switching threshold of the detector as a function of time delay between two pulses for delays of up to a few times the pulse width. In essence this is a study of the interference pattern of two pulses applied in coincidence, or near coincidence, to a nonlinear detector. This is a special case of the waveform measurement technique shown in Fig. 3 in which the signal is identical to the sampling pulse.

For simplicity the two Gaussian pulses have the same amplitudes, $i_{p1} = i_{p2} = 0.33$, and the same widths $W_1 = W_2 = W$. Our first simulations of this type of experiment, Fig. 15 (b), produced a surprisingly broadly-structured interference pattern. In this plot of $I_b(Th)$ versus delay time between first and second pulses, the image of the pulse is a negatively directed peak at zero delay. Only the pattern for positive delay times is displayed since the pattern is symmetric about zero delay. This case is for $W = 4.72$ ps, $\tau_p = 11.5$ ps, and $R_1 C_J = 243$ ps. Note that the width of the central minimum in Fig. 15 (b) is $W_o = 9.6$ ps. For the present we ignore the broad structure and ask how does W_o change as the width of the applied current pulses is changed? In Fig. 15 (c) W has been approximately doubled to 9.54 ps and it is found that the central minimum did increase in width but only by about 38% instead of the anticipated factor of 2. Thus it is clear that the detector is not responding in a simple way, and that the broad structure in the interference pattern cannot be ignored.

Evidently this structure is due to plasma oscillations. These oscillations are less damped here than in Fig. 12 since R_1 is now larger. In Fig. 15 (a) the time dependence of ϕ is shown with only the first of the two pulses applied. It is immediately obvious that the ringing behavior is present for the time delays of Fig. 15 (b), and is of the correct frequency to cause the observed structure. Thus our conclusion is that the plasma oscillations are so strong, particularly in Fig. 15 (b), that the system is not very sensitive to the applied pulse width.

In Fig. 15 (d) the width of the pulse is increased to 19.02 ps and the plasma oscillations are clearly less important than in the preceding two figures. It is revealing to calculate the bandwidth of this pulse. Using Eq. (27) the result is $f_{1/2}$ = 23 GHz. This is low compared with the plasma frequency of the detector which is about 87 GHz. Consequently there is very little energy available to excite the plasma oscillations. Thus it becomes clear why the extended structure in Fig. 15 (b) diminishes as wider pulse widths are used.

The oscillatory behavior of the interference pattern for large delay times is much reduced in Fig. 15 (d) as compared with the graph immediately above it. At the same time we note that W_o changes essentially by a factor of 2 between these two figures. Thus the width of the pulse image now changes in proportion to changes in the driving pulse width, which is the desirable result. This behavior is correlated with the pulse width W becoming comparable to and greater than the period of a plasma oscillation τ_p.

To further substantiate this point of view additional simulations were done for the narrow pulse width, 4.72 ps, used for Fig. 15 (b) but now applied to a junction with a shorter plasma period, τ_p = 4.76 ps. The result is the considerably lower level of plasma oscillations evident in the interference pattern Fig. 15 (e) as compared with Fig. 15 (b). Furthermore it is now found that when the applied pulse width is increased by a factor of 2, to 9.43 ps, the width of the pulse image also increases by a factor of 2, as is seen by comparing Figs. 15 (e) and (f).

Thus the interference pattern provides a sensitive means of measuring pulse width if $W \geq \tau_p$. We note in passing that our empirically derived criterion for sensitive pulse width measurements can also be expressed in the frequency domain. Using Eq. (38) we obtain for Gaussian pulses, $f_p/f_{1/2} \geq 2.27$, where f_p is the plasma frequency in Hz. This result is similar to our earlier observation that if the plasma frequency is well above the spectrum of the applied pulse, then the plasma oscillations are not highly excited and simple behavior results. However the width of the pulse image W_o is not necessarily numerically equal to the pulse width W. The widths of the interference

patterns in Figs. 15 (d) and (f) are about 1.3 times the driving pulse widths. It is expected that for larger pulse widths the pulse image will more nearly approximate the driving pulse. Without further theoretical development, detailed simulations are required to determine the driving pulse width from the interference pattern. An experiment of this type has been done by Faris in which a pulse width of 26 ps was measured with little distortion (28).

We are now in a position to consider the minimum measureable pulse width for Josephson detectors driven by current sources. The previously discussed maximum current density of 28,000 A/cm^2 corresponds, in Fig. 7, to a plasma period of 2.1 ps. Therefore the minimum measureable pulse width is also 2.1 ps if the change in the width of the pulse image must be proportional to the change in the width of the pulse. Narrower pulses can be measured if a less sensitive relationship between image width and pulse width is acceptable. Whether or not that might be the case depends on the experimental signal-to-noise ratio which is beyond the scope of the present article.

VI. Superconducting Striplines at High Frequencies

In previous sections we have detailed the speed limitations of the Josephson junction in various applications. A limitation which remains to be considered is that imposed by the interconnections between junctions in circuits.

As was realized early on (57), the operation of Josephson circuits at high speeds requires that the junctions be interconnected using transmission lines with matched loads. This arrangement prevents multiple

reflections of the signals and, assuming an ideal transmission line, allows full utilization of the devices' switching speed. Swihart has shown (58) that at frequencies well below the superconducting energy-gap frequency the striplines used to interconnect superconducting microcircuits are nearly ideal, having low loss and low dispersion. However, at frequencies approaching the energy gap, both attenuation and dispersion can be significant for striplines having lengths typical of microcircuit dimensions (59).

The speed limitations imposed by superconducting striplines were explored theoretically by Kautz (59) using the theory of Mattis and Bardeen for the conductivity of a superconductor. Figure 16 shows the attenuation and phase velocity of an example stripline chosen to be typical of those used in superconducting microcircuits. Results are shown for temperatures of 4.2 K at which the line is superconducting and 9.2 K at which the line is normal. Above the energy gap frequencies of the Nb and Pb-alloy conductors, 720 and 610 GHz respectively at 4.2 K, the attenuation and phase velocity are nearly the same for the superconducting and normal states. Well below the gap frequency, the superconducting line shows its superiority, having an attenuation orders of magnitude lower than the normal-state line and virtually no dispersion. Below about 10 GHz the attenuation and dispersion of the superconducting line are low enough that lines 1 cm or less in length can be considered ideal. At frequencies approaching the gap, however, both attenuation and dispersion become significant even for a 1 cm length of line.

AD-A089 353 NATIONAL BUREAU OF STANDARDS BOULDER CO ELECTROMAGN--ETC F/G 9/1
JOSEPHSON A/D CONVERTER DEVELOPMENT.(U)
SEP 80 C A HAMILTON, R E HARRIS, R L KAUTZ N00014-80-F-0017
UNCLASSIFIED NBSSR-724-21-80 NL

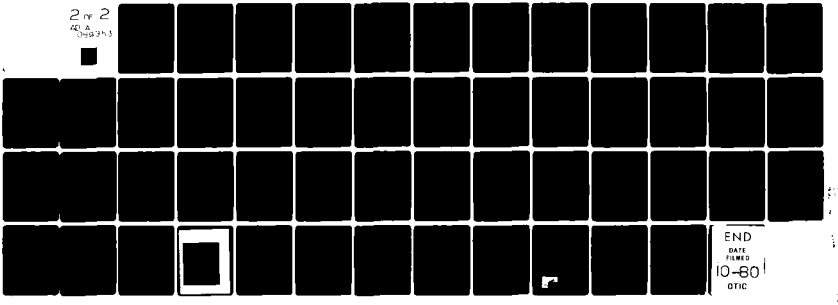

The effects of attenuation and dispersion at these high frequencies on pulses is shown in Fig. 17. Here we see the evolution of two pulses which are initially Gaussian, with widths W = 2.4 and 1.2 ps, as they propagate along the example stripline. For these pulses, virtually all of the energy is contained in frequency components below the energy gap, 99% of the energy being below 290 and 580 GHz for the 2.4 and 1.2 ps pulses, respectively. As Fig. 17 shows, the 2.4 ps pulse can travel no further than about 0.1 cm without significant distortion, while the limit for the 1.2 ps pulse is about 0.01 cm. Thus, for microcircuit applications, the quality of the example line is excellent for pulse widths down to a few picoseconds but for shorter pulses becomes rapidly unsatisfactory.

Finally, we examine the extent to which the high-frequency limit of the example stripline can be increased by changing its materials, temperature, or dimensions. Use of a superconductor with a larger energy gap, for example, leads to a direct increase in the high frequency limit. Unfortunately, such large-gap superconductors are refractory and difficult to work with. Lowering the operating temperature leads to a dramatic decrease in attenuation below the gap frequency but reduces the dispersion only slightly. If the example stripline is operated at 1.0 K then the sub-gap attenuation does not exceed 10^{-2} dB/m but dispersion at frequencies just below the gap still prevents propagation of sub-picosecond pulses over significant distances (59). Finally, because both the attenuation and the frequency dependent terms of the phase velocity are inversely proportional to the dielectric thickness, use of a thicker dielectric yields an overall improvement in pulse propagation (60). Increasing the

dielectric thickness by a factor of 10, for example, provides a 10-fold increase in the distance a given pulse can propagate before it becomes severly distorted. However, for the level of miniaturization required in a complex microcircuit, the dielectric can probably be no thicker than 1 μm and sub-picosecond pulses will propagate no more than a cm without distortion. Thus, the energy gap frequency represents a firm upper limit for pulse propagation in superconducting microcircuits.

VII. Discussion

The behavior of superconducting circuits in the picosecond regime has been studied in only a few expeiments. Consequently, in assessing picosecond applications of these circuits, we must rely heavily on circuit simulations. There are two models available for simulating the active part of the circuit: the RCSJ model and the microscopic model.

The RCSJ model is a simplification of the microscopic model and is used almost exclusively in the work reported here, partly because it requires much less computer time, but also because it is technically adequate. To establish its adequacy we compared it with frequency domain experiments in Section II.A., and we compared it with the microscopic model in two areas: the evaluation of the Josephson inductance in Section III.B and the calculation of picosecond waveforms in Section V.A. We summarize these results as follows: for electrical responses that occur in time intervals of a few picoseconds or longer, the RCSJ model is adequate for practical purposes. However, as shorter time periods are considered it should be recognized that the RCSJ model is increasingly inaccurate, with waveform errors as large as approximately 35% at 0.8 ps. Consequently we conclude that all of the time-domain experiments that we discussed are justifably analyzed with the RCSJ model.

Within the limitations of the RCSJ model we examined the step function response of a junction and derived a simplified formula for the turn-on delay τ_D associated with switching from the zero voltage state to the energy gap voltage. The theory of turn-on delay was also

extended to include arbitrary initial bias levels instead of only the single case of initial bias equal to the critical current. It was shown that the total step height of the bias current, rather than simply the amount of overdrive, is important in determining τ_D. A simple expression for the delay until the first appearance of a voltage pulse in a single junction SQUID was also developed.

Detailed consideration was then given to the theory for measurements of the height and width of pulses using a latching Josephson detector. Formulas were derived for the switching threshold condition for three ranges of pulse widths. We found the threshold condition to be especially simple for pulse widths $W \geq \tau_p$, where τ_p is the period of a plasma oscillation. The simple threshold condition is a linear relationship, $(i_b + i_{pl})_{Th} = 1$. With the RCSJ model any width of pulse will switch the detector if it has sufficient amplitude but the threshold conditions are nonlinear for $W < \tau_p$. The transmission lines limit the minimum pulse width to about 1 ps.

Simulations show that pulse width measurements can be made by studying the detector response for pulses arriving in near coincidence at the detector. It was found that this technique gives a sensitive measure of pulse width as long as $W \geq \tau_p$, the same criterion as for the detector to be linear.

For pulse widths less than τ_p the technique no longer proportionately measures the width of the pulse and becomes increasingly insensitive to pulse width as the width is decreased.

These results suggest a model in which the detector junction is an ideal instantaneously responding device in series with a low-pass filter which is resonant at the plasma frequency. The Q of the filter is determined by the loading across the junction. Thus most of the ringing reflected in Fig. 15 (b) can be suppressed by adding a resistor, but frequencies above ω_p cannot be readily observed.

Thus we conclude that the plasma period τ_p is an approximate measure of the highest time resolution that can be achieved in time-domain measurements. (Obviously a more complete understanding must include consideration of signal-to-noise ratio.) Because of self-heating effects τ_p cannot be made smaller than about 2 ps with present fabrication procedures.

Appendix A.

Time Domain Formulation of the Microscopic Theory

The microscopic theory seems to be not well known in detail, probably because the phenomenological model has consistently produced accurate descriptions of experimental circuits. Two things may chnage this situation in the future. First the theory has been recast into a time domain formulation which makes numerical computation simpler (61). Second, the increasing speed of practical circuits may require simulations of circuits for which the phenomenological model is too inaccurate. For these reasons we include in this Appendix a brief description of the microscopic theory.

The time domain formulation of the microscopic theory carries present and past information about the junction voltage in a function U(t):

$$U(t) = \exp\,(i\phi_s(t))$$

$$= \exp\,(-i\frac{e}{\hbar}\int_{-\infty}^{t} V(t')dt'). \qquad (A.1)$$

The function U(t) is very much like a single-particle wave function. It is a solution of the time-dependent Schroedinger equation having Hamiltonian -eV where V is the voltage across the junction.

The theory describes the junction current in terms of U(t):

$$I(t) = \frac{1}{2\pi}\,\mathrm{Im}\left\{U^{*}(t)\int_{-\infty}^{t} I_{qp}(t-t')\,U(t')\,dt'\right.$$

$$\left. + U(t)\int_{-\infty}^{t} I_{J}(t-t')\,U(t')\,dt'\right\}. \qquad (A.2)$$

Here the kernels $I_{qp}(t)$ and $I_J(t)$ produce the details of the time-dependent response of the junction. The U^* denotes the complex conjugate of U.

We now examine the form of the two kernels which are plotted in Fig. 18. First I_J which describes the supercurrent reveals a logarithmic singularity (negative) just after time zero. This integrable singularity represents a very fast but not instantaneous response. If the time scale were compressed, by letting the energy gap 2Δ become large, the singularity, combined with Eq. (A.2), transforms into the instantaneous current $I_o \sin\phi$ of the phenomenological model. Somewhat after time zero, I_J reveals oscillations at the energy gap frequency $2\Delta/h$. These correspond to the resonance known as the Riedel peak shown in Fig. 5.

It is also interesting to observe that the second term of Eq. (A.2) involving I_J includes a product of the form $U(t)U(t')$. This form tends to double the phase ϕ_s making it into the pair phase of Eq. (2). In contrast the first term of Eq. (A.2) contains the product $U^*(t)U(t')$ which does not double the phase ϕ_s. Thus the second term corresponds to the flow of paired electrons (the supercurrent), while the first term describes the flow of single (normal or quasiparticle) electrons.

The kernel I_{qp} is slightly more involved. This kernel contains all the information found in the current-voltage characteristic of Fig. 5. First we note that the characteristic becomes a linear resistance R_N for voltages above the energy gap. Since a pure resistance describes an instantaneous response, is appears in I_{qp} as a delta function. To simplify I_{qp} we therefore separate out the instantaneous response.

$$I_{qp}(t) = -2\,(\hbar/eR_N)\,\delta'(t) + I_{qpO}(t)\ . \qquad (A.3)$$

The portion of the kernel I_{qp0} is shown in Fig. 18. It also contains a peak just past time 0. This peak, however, is not as sharp as that in I_J and thus corresponds to a somewhat slower response. The oscillations at the gap frequency in I_J also appear in I_{qp0}, and correspond to the abrupt rise in current of the voltage-dependent resistance at the energy gap.

Although the time-domain formulation of the microscopic theory is conceptually equivalent to that in the frequency-domain, it is particularly useful in numerical simulations [61]. As devices are fabricated which are faster than those commonly used today, simulating them may necessarily involve this formulation of the theory.

The time-domain formulation could be significantly improved in one respect. The energy gap frequency oscillations in both I_J and I_{qp0} maintain significant amplitude to quite long times. This is a result of the sharp gap structure seen in the current-voltage characteristics. In practice, this structure is smeared over a range of voltages. As a result the kernels I_J and I_{qp0} for practical junctions should correspondingly exhibit a faster fall off in the amplitude of the energy gap oscillations. The development of a physical model for this fall-off would make it possible to truncate the integrals of Eq. (4) after a suitable time. This would speed numerical computations and reduce memory requirements.

Appendix B.

Turn-On Delay in a Single-Junction SQUID

Although not at the moment of apparent practical importance, turn-on delay in a single-junction SQUID is interesting in its own right. We shall sketch briefly how one can estimate τ_D for this case. Many mathematical details for flux entry into a SQUID may be found in reference 62. Consider the case in which the junction of Fig. 4 is shunted by a superconducting loop of inductance L. This circuit is described by Eq. (6) if we add $\bar{\phi}_o\phi/L$ to the right side. The washboard potential is now given a positive net curvature, becoming a parabola with ripples. The potential energy describing this case is

$$V = -\omega_p^2 \cos\phi + \frac{1}{2LC}(\phi-\beta_b)^2, \qquad (B.1)$$

where $\beta_k = LI_k/\bar{\phi}_o$. Apart from an unimportant constant, Eq. (B.1) goes to Eq. (17) as $L \to \infty$. It is clear that this SQUID will have less of a chance for switching to V_g because of the curvature of the parabola. The time delay before one or more fluxoids enter the SQUID after application of a step increase in I_b is of potential interest, however.

As I_b is raised slowly from zero, ϕ will advance from zero, always staying in the first local minimum given by $dV/d\phi = 0$. Thus ϕ is that value which solves

$$\phi + \beta_o \sin\phi = \beta_b, \qquad (B.2)$$

When $d^2V/d^2\phi = 0$ at the minimum, the particle will spill out, corresponding to the entrance of one (or more) fluxoids into the SQUID. Thus, fluxoid entry occurs when $\cos\phi = -1/\beta_0$ and Eq. (B.2) are satisfied simultaneously. The critical or threshold current for this to occur is given by

$$\beta_b^c = \phi_c + \beta_0 \sin\phi_c = \cos^{-1}(-\beta_0^{-1}) + (\beta_0^2 - 1)^{1/2}. \tag{B.3}$$

Suppose that when this current is reached, it is suddenly stepped to $I_b^c\,(1+\delta_0)$. If we then expand $\sin\phi$ about its initial value $\sin\phi_c$, retaining only the linear term in $\phi - \phi_c$, we find from the generalization of Eq. (6) to the SQUID,

$$\beta_b^2\,\delta_0 = LC\,\ddot{\phi} + \frac{L}{R}\,\dot{\phi}\ . \tag{B.4}$$

The term with ϕ has dropped out, leaving the same form of equation as in Section IV for the junction not shunted by inductance. If we assert, as there, that the turn-on delay time can be approximated by the time required for the phase to advance by one-half radian, we get

$$\tau_D = \omega_p^{-1}(\delta_0 f)^{-1/2}, \tag{B.5}$$

where $f = \beta_b^c/\beta_0 = 1 + \pi/(2\beta_0) + (2\beta_0^2)^{-1}$. The approximate equality here results from expanding the right side of Eq. (B.3) in powers of β_0^{-1}, and is an excellent approximation even at the lowest value of β_0 (unity) for which the system particle can be trapped away from the bottom of the parabola. Equation (B.5) should be compared with Eq. (18), which it generalizes.

Numerical simulations show that Eq. (B.5) is quite a good approximation to the time for the rising of the first voltage pulse. The effect of the shunt inductance is to shorten the turn-on delay time.

Appendix C

Turn-On Delay in a Two-Junction SQUID

A two-junction SQUID, or interferometer, is depicted in Fig. 19 (a). It is evident that such a device is inherently slower than a single junction, principally because the two junctions will not necessarily act in concert.

There is a trivial exception to this which we shall mention here, because the idea occurs again later. When the interferometer is completely symmetric, and there is no control current I_c, the bias current I_b divides equally between the two halves of the interferometer. The inductances L and damping resistors R_d draw no currents. When I_b is stepped to $2I_o(1+\delta_o)$, one half of this passes through each junction. The junctions act together, and the turn-on delay is given by Eqs. (18), (19), or (23), where ω_p still refers to the single-junction plasma frequency.

Of course, the reason for using a multi-junction interferometer is because the control current allows one to set the switching threshold value of I_b over a range of values, as shown in Fig. 19 (b). When $I_c \neq 0$, the analytical problem is much more difficult than for a single junction. The only published treatment of turn-on delay in a two-junction SQUID at the moment is that of E. P. Harris [52]. We shall here follow Harris' reasoning and give his results.

If the interferometer is heavily damped to suppress the LC resonance effects of the circuit, the interferometer is described approximately by the two equations

$$\frac{L}{R_d}\dot{\phi}_- + \phi_- + \beta_o \sin\phi_- \cos\phi_+ = \beta_c, \qquad (C.1)$$

$$2LC\ddot{\phi}_+ + \frac{L}{R_L}\dot{\phi}_+ + 2\beta_o \sin\phi_+ \cos\phi_- = \beta_b, \qquad (C.2)$$

where $\phi_\pm = \frac{1}{2}(\phi_1 \pm \phi_2)$, and the β's have been defined following Eq. (B.1). One sees from Eqs. (C.1) and (C.2) that if β_c is held constant at or below a threshold value, while β_b is stepped up, then ϕ_+ will first respond; ϕ_- will follow by virtue of the coupling between the two equations. Similarly, if β_b is fixed and β_c is stepped, ϕ_- first responds. Harris considered only the latter case.

The control current is taken as zero for $t < 0$, and I_b is fixed (for all t) at I_{b1}, so that $\phi_-(t < 0) = 0$ from Eq. (C.1). At $t = 0$, I_c is stepped to a value I_{c2}, greater than the threshold value I_{c1}. Equation (C.2) shows then that $\sin\phi_+$ is given approximately by $\beta_{b1}\sec\phi_-/2\beta_o$ until the time at which the latter quantity equals unity. Harris calls this time interval τ_{int} and develops an approximate expression for it, given below. At that time, ϕ_+ begins increasing rapidly, that is, the two junctions begin moving together and the interferometer tends to behave as a single junction. The time for ϕ_+ to advance from $\pi/2$ to $3\pi/2$ is designated τ_{ext}, and the total turn-on delay time of the interferometer is taken to be $\tau_D = \tau_{int} + \tau_{ext}$. For τ_{ext}, Harris simply adopts the single junction result, in which the capacitance is twice the single junction capacitance, and I_o is replaced by I_m, the threshold value of I_b when I_c has its final value I_{c2} (see Fig. 19 b). Harris's approximate expression for τ_{int} is $\tau_o + \tau_1$ where

$$\omega_o \tau_o = \frac{1}{B} \ln \left(\frac{I_{c2}}{\Delta I_c} \right) + \frac{I_o}{\Delta I_c} \left(\phi_1 - \frac{I_{c1}}{I_o} \right) , \qquad (C.3)$$

$$\omega_o \tau_1 = \frac{I_o}{\Delta I_c} \left[\cos^{-1} \left(\frac{I_{b2}}{2I_o} \right) - \phi_1 \right], \qquad (C.4)$$

$$I_{b2} = I_{b1} - 2 \bar{\phi}_o \phi_1 (2R_L C + \tau_o)/(R_L \tau_o^2) , \qquad (C.5)$$

$$B = \beta_o^{-1} + \left[1 - \left(\frac{I_{b1}}{2I_o} \right)^2 \right]^{-1/2} , \qquad (C.6)$$

Also, $\phi_1 = \cos^{-1}(I_{b1}/2I_o)$, $\omega_o = R_d I_o/\bar{\phi}_o$, and $\Delta I_c = I_{c2} - I_{c1}$. Harris states that these formulas agree with the results of numerical simulations to within about 15% for fractional overdrives ranging from 0.1 to 1.5, and for values of R_d ranging from heavy damping to roughly critical damping.

REFERENCES

1. Eberhard Riedel, "Zum Tunneleffekt bei Supraleitern in Mickrowellenfeld," Z. Naturforschung, Vol. 19A, pp. 1634-1635, 1965.
2. N. R. Werthamer, "Nonlinear Self-Coupling of Josephson Radiation in Superconducting Tunnel Junctions," Phys. Rev., Vol. 147, pp. 255-263, July 8, 1966.
3. W. C. Stewart, "Current-Voltage Characteristics of Josephson Junctions," Appl. Phys. Letters, Vol. 12, pp. 277-280, April 15, 1968.
4. D. E. McCumber, "Effect of ac Impedance on dc Voltage-Current Characteristics of Superconductor Weak-Link Junctions," J. Appl. Phys., Vol. 39, pp. 3113-3118, June 1968.
5. S. Basavaiah, J. M. Eldridge, and J. Matisoo, "Tunneling in Lead-Lead Oxide-Lead Junctions," J. Appl. Phys., Vol. 45, pp. 457-464, January 1974.
6. H. H. Zappe, "Josephson Quantum Interference Computer Devices," IEEE Trans. Mag., Vol. MAG-13, pp. 41-47, January 1977.
7. T. A. Fulton and R. C. Dynes, "Switching to Zero Voltage in Josephson Tunnel Junctions, Solid State Comm's. Vol. 9, pp. 1069-1073, 1973; T. A. Fulton, "Punchthrough and the Tunneling Cryotron," Appl. Phys. Letters, Vol. 19, pp. 311-313, November 1, 1971.
8. B. D. Josephson, "Possible New Effects in Superconductive Tunneling," Phys. Letters, Vol. 1, pp. 251-253, July 1962.
9. Sidney Shapiro, "Josephson Currents in Superconducting Tunneling: The Effect of Microwaves and Other Observations," Phys. Rev. Letters, Vol. 11, pp. 80-82, July 15, 1963.
10. P. Russer, "Influence of Microwave Radiation on Current-Voltage Characteristic of Superconducting Weak Links," J. Appl. Phys., Vol. 43, pp. 2008-2010, April 1972.

11. R. L. Kautz, to be published.

12. D. G. McDonald, V. E. Kose, K. M. Evenson, J. S. Wells, and J. D. Cupp, "Harmonic Generation and Submillimeter Wave Mixing With the Josephson Effect," Appl. Phys. Letters, Vol. 15, pp. 121-122, August 15, 1969.

13. D. G. McDonald, K. M. Evenson, J. S. Wells, and J. D. Cupp, "High-Frequency Limit of the Josephson Effect," J. Appl. Phys., Vol. 42, pp. 179-181, January 1971.

14. D. A. Weitz, W. J. Skocpol, and M. Tinkham, "High-Frequency Behavior of "Ideal" Superconducting Point Contacts," Phys. Rev. Letters, Vol. 40, pp. 253-256, January 23, 1978; "Far-Infrared Frequency Dependence of the ac Josephson Effect in Niobium Point Contacts," Phys. Rev., Vol. B18, pp. 3282-3292, October 1, 1978.

15. M. Tinkham, M. Octavio, and W. J. Skocpol, "Heating effects in high frequency metallic Josephson devices: Voltage limit, bolometric mixing, and noise," J. Appl. Phys., Vol. 48, pp. 1311-1320, March 1977.

16. D. G. McDonald, F. R. Petersen, J. D. Cupp, B. L. Danielson, and E. G. Johnson, "Josephson junctions at 45 times the energy-gap frequency," Appl. Phys. Letters, Vol. 24, pp. 335-337, April 1, 1974.

17. D. A. Weitz, W. J. Skocpol, and M. Tinkham, "Niobium point-contact Josephson-junction behavior at 604 GHz," Appl. Phys. Letters, Vol. 31, pp. 227-229, August 1, 1977.

18. C. A. Hamilton and Sidney Shapiro, "Experimental Demonstration of the Riedel Peak," Phys. Rev. Letters, Vol. 26, pp. 426-428, February 22, 1971.

19. S. A. Buckner, T. F. Finnegan, and D. N. Langenberg, "Riedel Singularity in Sn-Sn-Oxide-Sn Josephson Tunnel Junctions," Phys. Rev. Letters, Vol. 28, pp. 150-154, January 17, 1972.

20. H. H. Zappe, and B. S. Landman, "Experimental investigation of resonances in low-Q Josephson interferometric devices," J. Appl. Phys., Vol. 49, pp. 4149-4154, July 1978.

21. J. Matisoo, "Subnanosecond Pair-Tunneling to Single-particle Tunneling Transitions in Josephson Junctions," Appl. Phys. Letters, Vol. 9, pp. 167-168, August 15, 1966.

22. W. Jutzi, Th. O. Mohr, M. Gasser, and H. P. Gschwind, "Josephson Junctions with 1 μm Dimensions and with Picosecond Switching Times," Electronics Letters, Vol. 8, pp. 589-591, 1972.

23. T. R. Gheewala, "A 30 ps Josephson Current Injection Logic (CIL) Family," IEEE J. Solid State Circuits, Vol. SC-14, pp. 787-793, October 1979.

24. Hans H. Zappe, "A subnanosecond Josephson Tunneling Memory Cell with Nondestructive Readout," IEEE J. Solid State Circuits, Vol. SC-10, pp. 12-19, February 1975.

25. D. J. Herrell, "A Josephson Tunneling Logic Adder," IEEE Trans.-Mag., Vol. MAG-10, pp. 864-867, September 1974.

26. C. A. Hamilton, F. L. Lloyd, R. L. Peterson, and J. R. Andrews, "A Superconducting Sampler for Josephson Logic Circuits," Appl. Phys. Letters, Vol. 35, pp. 718-719, November 1, 1979.

27. C. A. Hamilton, "A Sampling Circuit and Method Therefor", U. S. Patent Application Serial No. 853,354, (1977 pending).

28. Sadeg M. Faris, "Generation and Measurement of Ultrashort Current Pulses with Josephson Devices," to be published.

29. David B. Tuckerman, "A Josephson Ultrahigh Resolution Sampling System," to be published.

30. A. J. Dahn, A. Denenstein, T. F. Finnegan, D. N. Langenberg, and D. J. Scalapino, "Study of the Josephson Plasma Resonance," Phys. Rev. Letters, Vol. 20, pp. 859-863, April 15, 1968.

31. A. V. Svidzinskii and V. A. Slyusarev, "Contribution to the Theory of Tunneling in Superconductors," Sov. Phys. JETP, Vol. 24, pp. 120-123, January 1967.

32. A. I. Larkin and Yu. N. Ovchinnikov, "Tunnel Effect Between Superconductors in an Alternating Field," Sov. Phys. JETP, Vol. 24, pp. 1035-1040, May 1967.

33. Richard E. Harris, "Cosine and other terms in the Josephson tunneling current," Phys. Rev., Vol. B10, pp. 84-94, July 1, 1974.

34. Richard E. Harris, "Josephson tunneling current in the presence of a time-dependent voltage," Phys. Rev., Vol. B11, pp. 3329-3333, May 1, 1975.

35. T. A. Fulton and D. E. McCumber, "dc Josephson Effect for Strong-Coupling Superconductors," Phys. Rev., Vol. 175, pp. 585-586, November 1968.

36. D. M. Ginsberg, Richard E. Harris, and R. C. Dynes,"Strong-coupling correction to the low-frequency electrical conductivity of superconductors and Josephson junctions," Phys. Rev., Vol. B14, pp. 990-992, August 1, 1976. Richard E. Harris, R. C. Dynes, and D. M. Ginsberg, "Strong-coupling correction to the jump in the quasi-particle current of a superconducting tunnel junction," Phys. Rev., Vol. B14, pp. 993-995, August 1, 1976.

37. D. G. McDonald, E. G. Johnson, and R. E. Harris, "Modeling Josephson junctions," Phys. Rev., Vol. B13, pp. 1028-1031, February 1, 1976.

38. S. Shapiro, P. H. Smith, J. Nicol, J. L. Miles, and P. F. Strong, "Superconductivity and Electron Tunneling," IBM J. Res. Dev., Vol. 6, pp. 34-43, January 1962.

39. A. B. Zorin and K. K. Likharev, "Current-voltage characteristics of low capacitance Josephson junctions," Sov. J. Low Temp. Phys., Vol. 3, pp. 70-71, February 3, 1977.

40. W. A. Schlup, "Solution of the Werthamer Equation at Finite Temperatures," Phys. Rev., Vol. B18, pp. 6132-6138, December 1978.

41. D. G. McDonald and R. L. Peterson, "Design of a Josephson-Junction Picosecond Pulser," J. Appl. Phys., Vol. 48, pp. 5366-5369, December 1977.

42. Richard E. Harris, "Intrinsic Response Time of a Josephson Tunnel Junction," Phys. Rev., Vol. B13, pp. 3818-3821, May 1976.

43. S. Basavaiah and R. F. Broom, "Characteristics of In-Line Josephson Tunneling Gates," IEEE Trans. Mag., Vol. MAG-11, pp. 759-762, March 1975.

44. Vinay Ambegaokar and Alexis Baratoff, "Tunneling Between Superconductors," Phys. Rev. Letters, Vol. 10, pp. 486-489, June 1, 1963; Erratum, Phys. Rev. Letters, Vol. 11, p. 104, July 15, 1963.

45. J. H. Greiner, C. J. Kircher, and I. Ames, "Fabrication Process for Josephson Integrated Circutis," IBM J. Res. Dev., to be published.

46. John M. Baker, C. J. Kircher, and J. W. Matthews, "Structure of Tunnel Barrier Oxide for Pb Alloy Josephson Junctions," IBM J. Res. Dev., to be published.

47. Jerome M. Eldridge and Juri Matisoo, "Fabrication of Variable Current Density Josephson Junctions," U. S. Patent No. 3,816,173, June 11, 1974.

48. T. R. Gheewala, "Design of 2.5 μm Josephson Current Injection Logic," IBM J. Res. Dev., March 1980.

49. J. Niemeyer and V. Kose, "Observation of large dc supercurrents at nonzero voltages in Josephson tunnel junctions," Appl. Phys. Letters, Vol. 29, pp. 380-382, September 15, 1976.

50. R. F. Broom, W. Jutzi, and Th. O. Mohr, "A 1.4 mil^2 Memory Cell With Josehpson Junctions," IEEE Trans. Mag., Vol. MAG-11, pp. 755-758, March 1975.

51. Steven B. Kaplan, "Acoustic Matching of Superconducting Films to Substrates," J. Low Temp. Phys., Vol. 37, pp. 343-365, 1979.

52. E. P. Harris, "Turn-On Delay of Josephson Interferometer Logic Devices," IEEE Trans. Mag., Vol. MAG-15, pp. 562-565, January 1, 1979.

53. H. H. Zappe, "Minimum Current and Related Topics in Josephson Tunnel Junction Devices," J. Appl. Phys., Vol. 44, pp. 1371-1377, March 1973.

54. R. L. Peterson and D. G. McDonald, "Picosecond Pulses From Josephson Junctions: Phenomenological and Microscopic Analyses," IEEE Trans. Mag., Vol. MAG-13, pp. 887-890, January 1977.

55. D. B. Sullivan and J. E. Zimmerman, "Mechanical Analogs of Time Dependent Josephson Phenomena," Amer. J. Phys., Vol. 39, pp. 1504-1517, December 1971.

56. Sang H. Dhong and T. Van Duzer, "The Minimum-Width Control-Current Pulse for Josephson Logic Gates," to be published.

57. W. Anacker, "Josephson tunneling devices - A new technology with potential for high-performance computers," AFIPS Conference Proceedings: Fall Joint Computer Conference, Vol. 41, pp. 1269-1278, Decmeber 1972.

58. J. C. Swihart, "Field Solution for a Thin-Film Superconducting Strip Transmission Line," J. Appl. Phys., Vol. 32, pp. 461-469, March 1961.

59. R. L. Kautz, "Picosecond Pulses on Superconducting Striplines," J. Appl. Phys., Vol. 49, pp. 308-314, January 1978.

60. R. L. Kautz, "Miniaturization of Normal State and Superconducting Striplines," NBS J. Res., Vol. 84, pp. 247-259, May 1979.

61. Richard E. Harris, "Numerical evaluation of the response of a Josephson tunnel junction in an arbitrary circuit," J. Appl. Phys., Vol. 48, pp. 5188-5190, December 1977.

62. R. L. Peterson and R. I. Gayley, "Multiple Magnetic Flux Entry into SQUIDs: A General Way of Examining the cosϕ Conductance," Phys. Rev. Vol. B18, pp. 1198-1206, August 1, 1978.

Figure Captions

Fig. 1. Experimental results for the induced dc in a Josephson junction with applied radiation at 891 and 805 GHz. Spectral features appear at 1.84 and 1.66 mV, corresponding in Eq. (3) to Josephson oscillations at the frequencies of the applied radiation. The feature at 0.18 mV is not due to applied radiation but corresponds to the difference frequency of the applied signals.

Fig. 2. (a) Sampling circuit for measuring the risetime of a signal I_s. A sampling oscilloscope in a servo loop is used to automatically measure the time at which the signal plus the bias cause J1 to switch. I_s is reproduced by plotting the bias versus switching time. (b) Measured waveform, using the above technique, of the switching transition of a Josephson junction.

Fig. 3. Sampling circuit for measuring an arbitrary signal waveform I_s. A sharp pulse of amplitude I_{p1} is obtained by differentiating, in an RC network, the switching transition waveform of junction J1. This pulse and the unknown signal I_s are applied to a detector junction J2 which, through I_{b2}, is then adjusted to the threshold for switching. The resulting value of I_{b2} is the essential information needed for determining the value of I_s at the time the pulse occurs. The entire signal waveform is measured by sweeping the time at which the pulse occurs.

Fig. 4. Schematic representation of the RCSJ model. (a) The "J" symbol represents the supercurrent path which has current $I_0 \sin\phi$. C_J is the intrinsic junction capacitance and R may be either the voltage dependent resistance R_J or a parallel combination of R_J with an external shunt resistance. (b) The voltage dependent resistance R_J has three segments. Below the energy gap voltage V_g the resistance is R_1. Above V_g is a low resistance region which is followed by a higher resistance designated as R_N, the junction normal state resistance. R_J is an approximation to the quasiparticle I-V characteristic of the microscopic model.

Fig. 5. Results of the microscopic theory of Josephson junctions. The illustrated functions reveal the frequency dependence of the supercurrent and the voltage dependence of the quasiparticle current as described in the text.

Fig. 6. Theoretical impulse response of a tunnel junction without capacitance. The current calculated from the microscopic model is illustrated for a voltage impulse applied at time zero. The amplitude of the impulse was adjusted to produce a phase shift of $\pi/2$.

Fig. 7. Macroscopic properties of small Pb alloy Josephson junctions. The critical current density j_c, the time constant $R_N C_J$, the plasma frequency ω_0, and the Josephson penetration depth λ_J are shown as functions of tunneling barrier thickness d.

Fig. 8. The potential energy washboard. (a) The potential energy of Eq. (17), normalized to ω_p^2, is plotted against $\phi/2\pi$ for $I_b = I_o$. (b) Comparison of potential energies for three values of I_b/I_o: top curve, 0.9; middle curve, 1.0; bottom curve, 1.1. The circles on the upper and middle curves shows the initial position and potential energy of the system "particle". The circle on the lower curve lies at 1/2 radian beyond $\pi/2$.

Fig. 9. Switching curve (from simulations) for a current biased junction, stepped from $I_b = I_o$ to 1.01 I_o, illustrating both the turn-on delay and rise time portions. $I_o = 0.0796$ mA, $C_J = 1.0$ pF, $V_g = 2.5$ mV, $R_1 = 200\ \Omega$, $R_L = \infty$. The method used for determining τ_D from the switching curve is shown. The 10-90% voltage levels on the risetime portion are also indicated. For weak coupling $R_N = \pi V_g/4I_o = 24.7\ \Omega$, so $R_N C_J = 24.7$ ps. Compare with τ_R (10-90%).

Fig. 10. Turn-on delay as determined from Eq. (18) (upper curve), Eq. (19) (lower curve), and from simulations (circles). The junction parameters are those of Fig. 9. I_b is stepped from I_o.

Fig. 11. One period of the voltage across the load resistance of the microwave driven pulser with an applied frequency of 10 GHz. The microscopic theory of junctions was used to calculate this waveform. The resulting pulse width is 2.2 ps with the following circuit parameters, $R_N C_J = 3.24$ ps, $R_N/R_L = 4$.

Fig. 12. Calculated detector responses for four different applied pulse widths. The applied current pulses are shown at the top of each column of illustration with the corresponding detector responses arranged below. The detector properties and the applied pulse heights ($i_{pl} = 0.5$) are the same in all cases. The response of the junction voltage V and the phase ϕ (radians) are illustrated for bias levels just above threshold (labeled A) and for just below threshold (labeled B). For the four columns, reading from left to right, the pulse widths are: 324, 32.4, 3.24, and 0.324 ps; and the bias levels above and below threshold are: 0.500215, 0.500214; 0.502139, 0.502138; 0.53905, 0.53904; 0.95528, 0.95527 mA. The detector properties are $I_o = 1$ mA, $R_N = 1.578\ \Omega$, $R_1/R_N = 5$, $C_J = 2.05$ pF.

Fig. 13. (a) Circuit diagram for simulations of detector response. I_p is a current source for a Gaussian pulse and I_b is the constant bias supply. The X symbol represents the Josephson junction, which is described by the RCSJ model. (b) Calculations of detector threshold bias $i_b(Th)$ as a function of pulse width W. For all points in this graph the pulse height is $i_{pl} = 0.5$. The circles, connected by a solid line, represent data from the RCSJ model, the squares are calculations from the impulse response Eq. (34), and the triangles are calculations using the square pulse approximations Eq. (39). The maximum threshold current for $i_{pl} = 0.5$ in 1.5, the value closely approached by the impulse approximation at the narrowest pulse widths. The detector parameters are the same as for Fig. 12.

Fig. 14. Response of an idealized linear detector. (a) $I_p(t)$ is the current to the detector. This current has the form of two identical triangular pulses with delay time τ between them. (b) Threshold bias of the detector $I_d(Th)$ plotted versus τ, showing the "image" of the pulses of (a).

Fig. 15. Pulse width measurement simulations. (a) Time dependence of a lightly damped plasma oscillation excited by a single pulse of width W = 4.72 ps, with its center arriving at the detector at time zero. (b) - (f) Interference patterns. These patterns are graphs of the threshold bias as a function of delay time between the arrival of identical pulses at the detector. In all cases the pulse amplitude $i_{pl} = 0.33$. The broadly structured interference pattern of (b) is a reflection of the plasma oscillations in (a). For illustrations (b) - (d) the detector characteristics are unchanged; the applied pulse widths have the values 4.72, 9.54, and 19.0 ps, respectively.

The illustrated values of $1/2W_o$ are the half widths of the "image" of the applied pulses. The junction parameters are $I_o = 1$ mA, $R_N = 1.412\ \Omega$, $R_1/R_N = 17$, $C_J = 10.1$ pF, and $\omega_p = 0.548 \times 10^{12} s^{-1}$. For the illustrations (e) and (f) the plasma frequency of the detector has been increased. The applied pulse widths are 4.72 and 9.43 ps, respectively. The junction parameters are $I_o = 1$ mA, $R_N = 1.4.2\ \Omega$, $R_1/R_N = 17$, $C_J = 1.63$ pF, and $\omega_p = 1.37 \times 10^{12} s^{-1}$.

Fig. 16. Theoretical attenuation (solid line) and phase velocity (dashed line) for an example superconducting stripline at 4.2 K and for the same stripline in the normal state at 9.2 K. The example stripline consists of a 0.4 μm thick Nb ground plane, a 0.1 μm layer of Nb_2O_5 dielectric (assumed lossless), and a 0.4 μm thick Pb alloy strip (assumed wide compared to the dielectric thickness).

Fig. 17. Simulated pulse propagation on the example stripline described in Fig. 16. The histories of two pulses are shown in (a) and (b), respectively, by plotting the pulse shape at various distances L along the line. The pulses are originally Gaussian shaped, at L = 0, with W = 2.4 ps in (a) and 1.2 ps in (b).

Fig. 18. The two kernels I_J and I_{qp0} in the time domain formulation of the microscopic theory.

Fig. 19. (a) Two-junction interferometer, showing damping resistors R_d and a load resistor R_L. Each X represents the junction depicted in Fig. 4 (a). (b) Sketch of a typical threshold curve for a two-junction interferometer, showing control stepped from 0 to I_{c2}, at bias current I_{b1}.

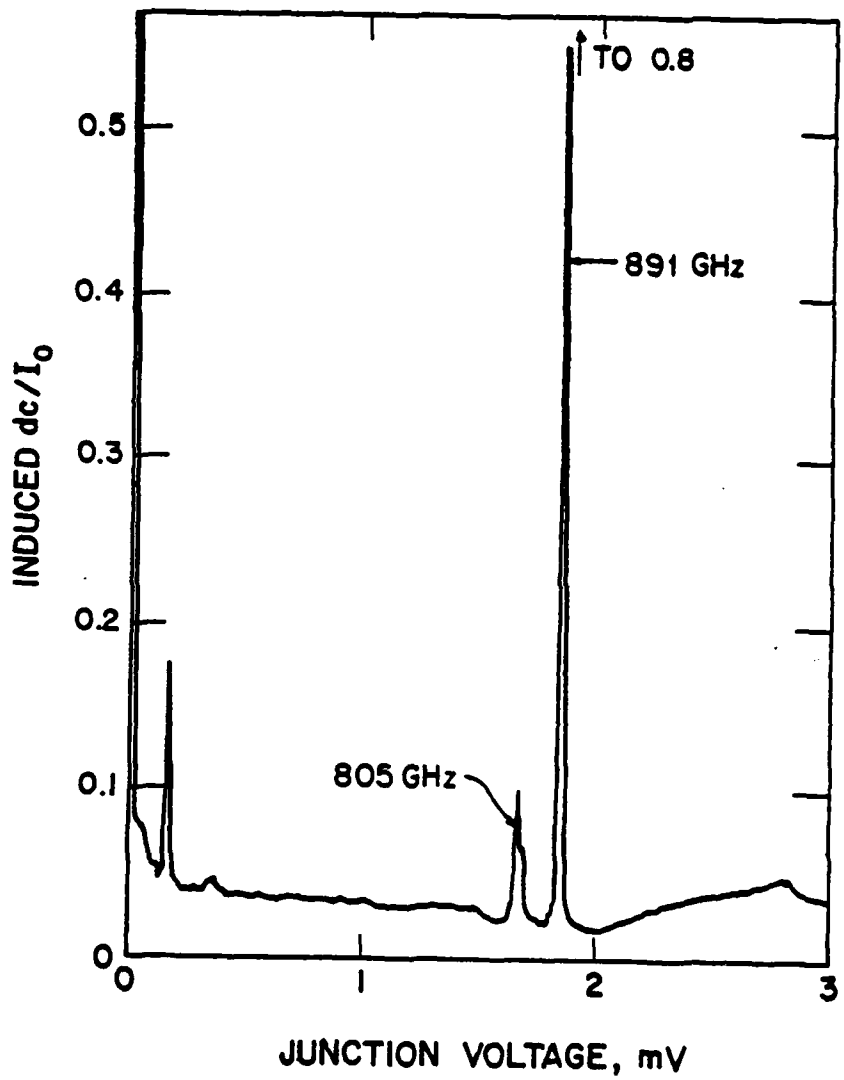
TO 0.8
0.5
0.4
891 GHz
0.3
0.2
0.1
805 GHz
0
0
1
2
3
INDUCED dc/I_o
JUNCTION VOLTAGE, mV

Fig 1

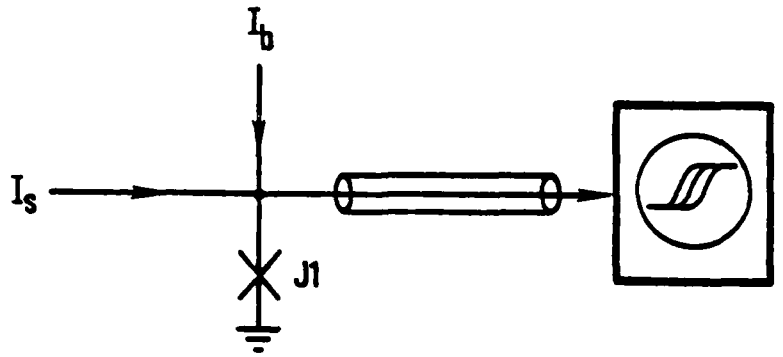

(a)

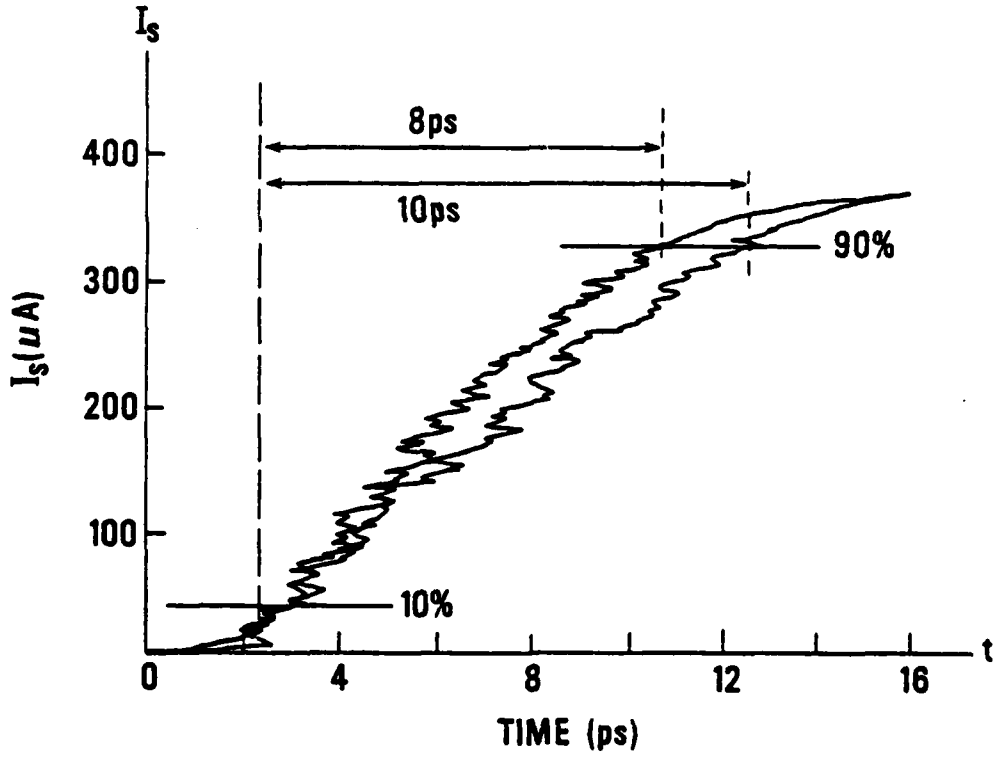

(b)

Fig 2

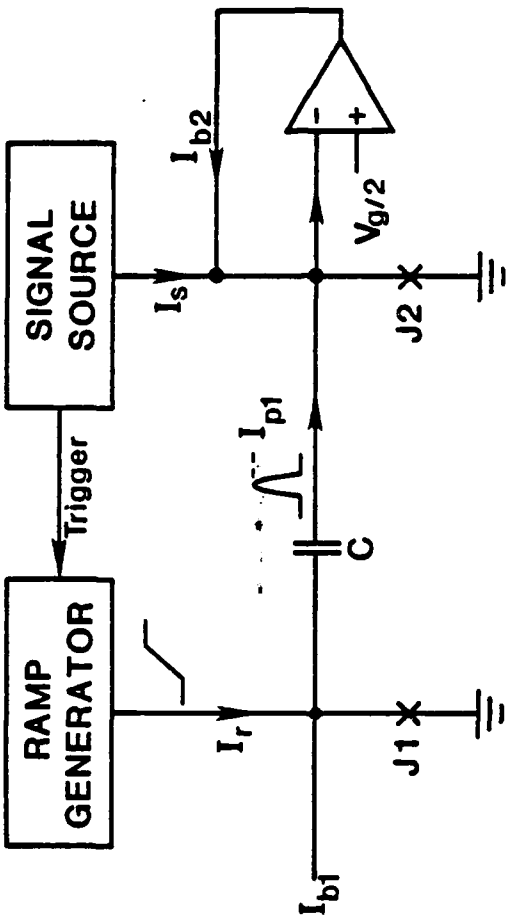
SIGNAL SOURCE
RAMP GENERATOR
Trigger
I_{b2}
I_s
$V_{g/2}$
J2
I_{p1}
C
I_r
J1
I_{b1}

Fig 3

(a)

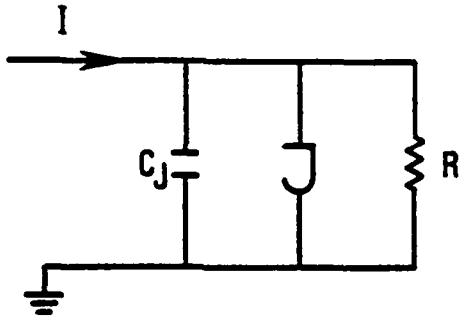

(b)

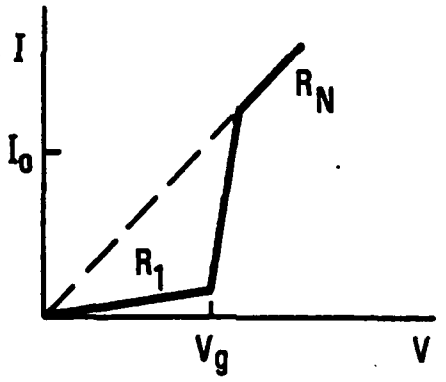

fig 4

$\left(\frac{eR_N}{2\Delta}\right) I$
2
1
0
0
1
2
3
$\frac{\hbar\omega}{2\Delta}$
I_N
-Re I_J
Im I_{qp}

Fig 5

Fig 1

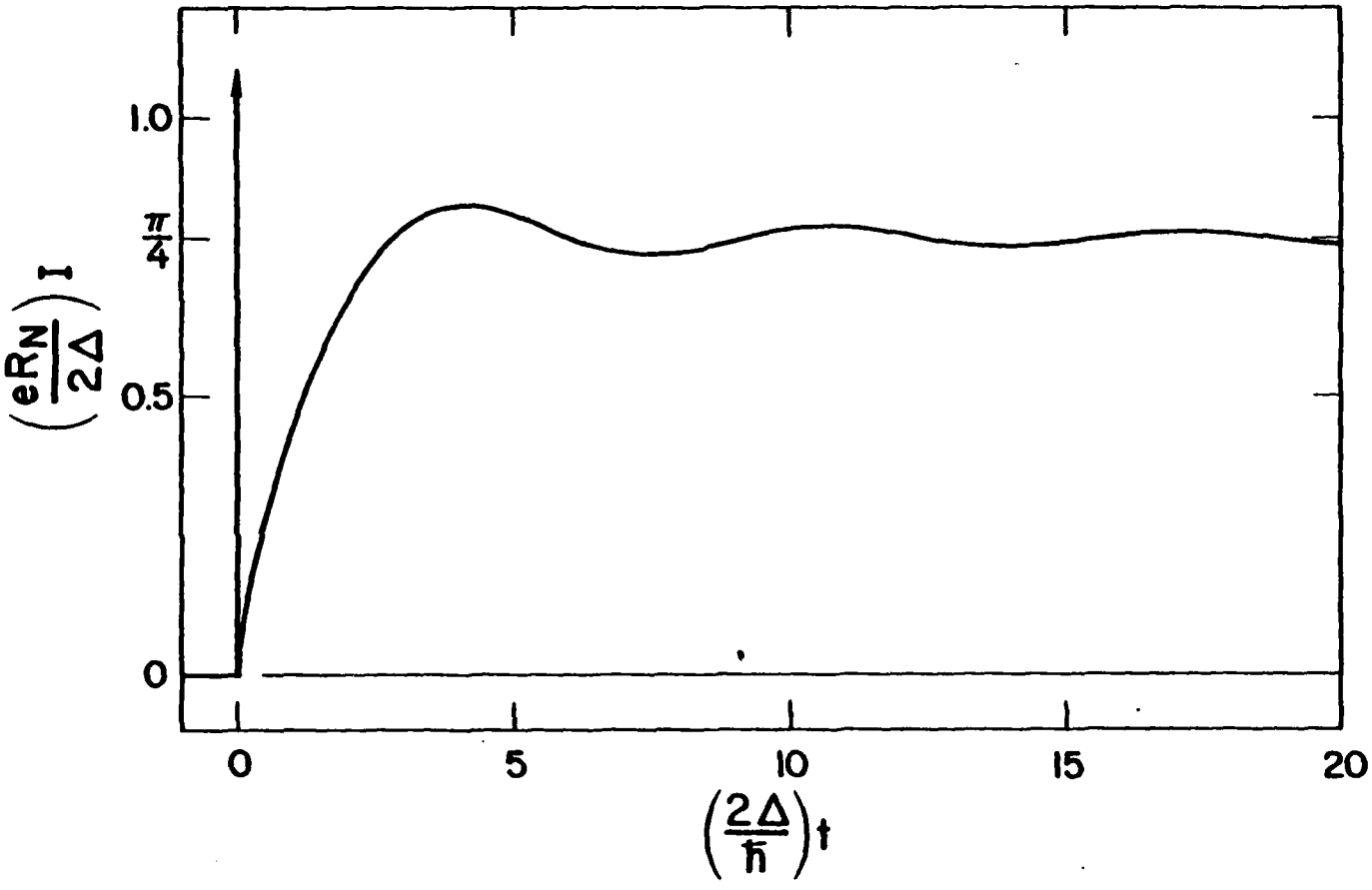
1.0
π/4
0.5
0
$\left(\frac{eR_N}{2\Delta}\right) I$
0
5
10
15
20
$\left(\frac{2\Delta}{\hbar}\right) t$

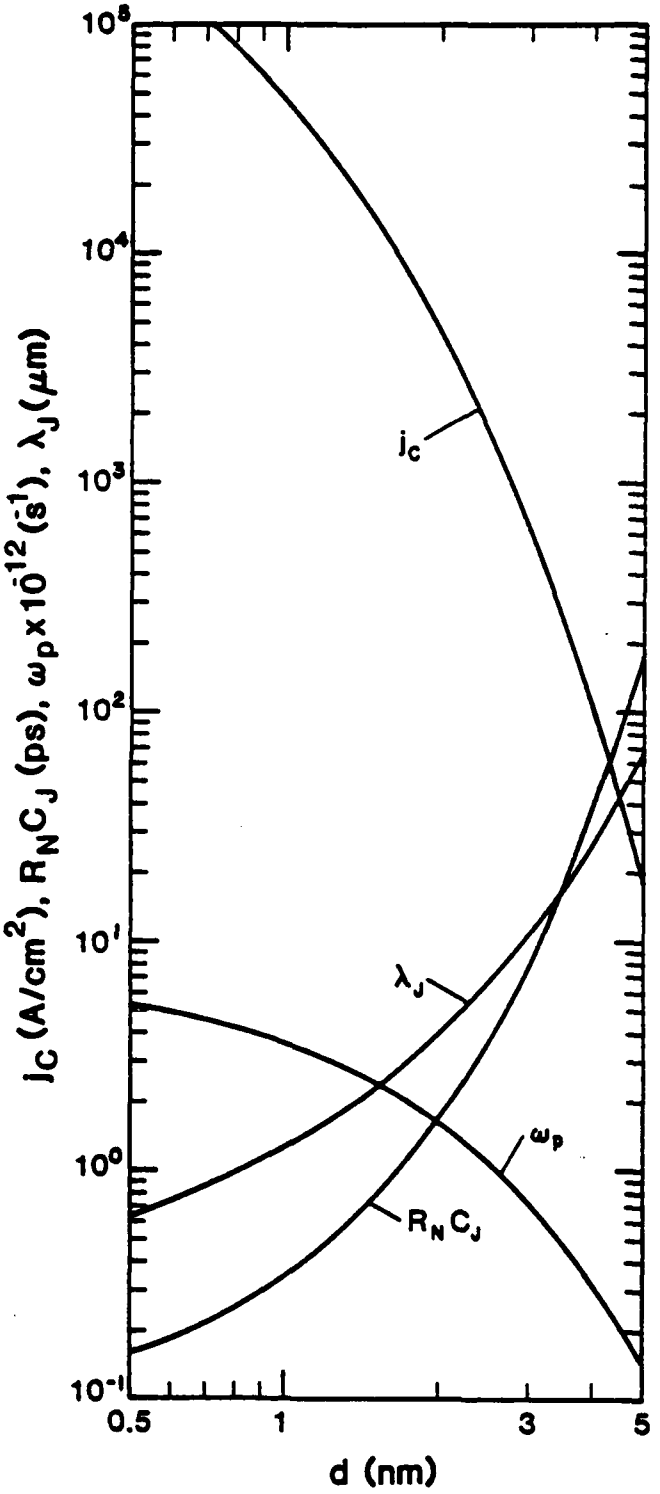
10^8
10^4
10^3
10^2
10^1
10^0
10^{-1}
j_c
λ_J
ω_p
$R_N C_J$
0.5
1
3
5
d (nm)
j_C (A/cm^2), $R_N C_J$ (ps), $\omega_p \times 10^{-12}$ (s^{-1}), λ_J (μm)

Fig 7.

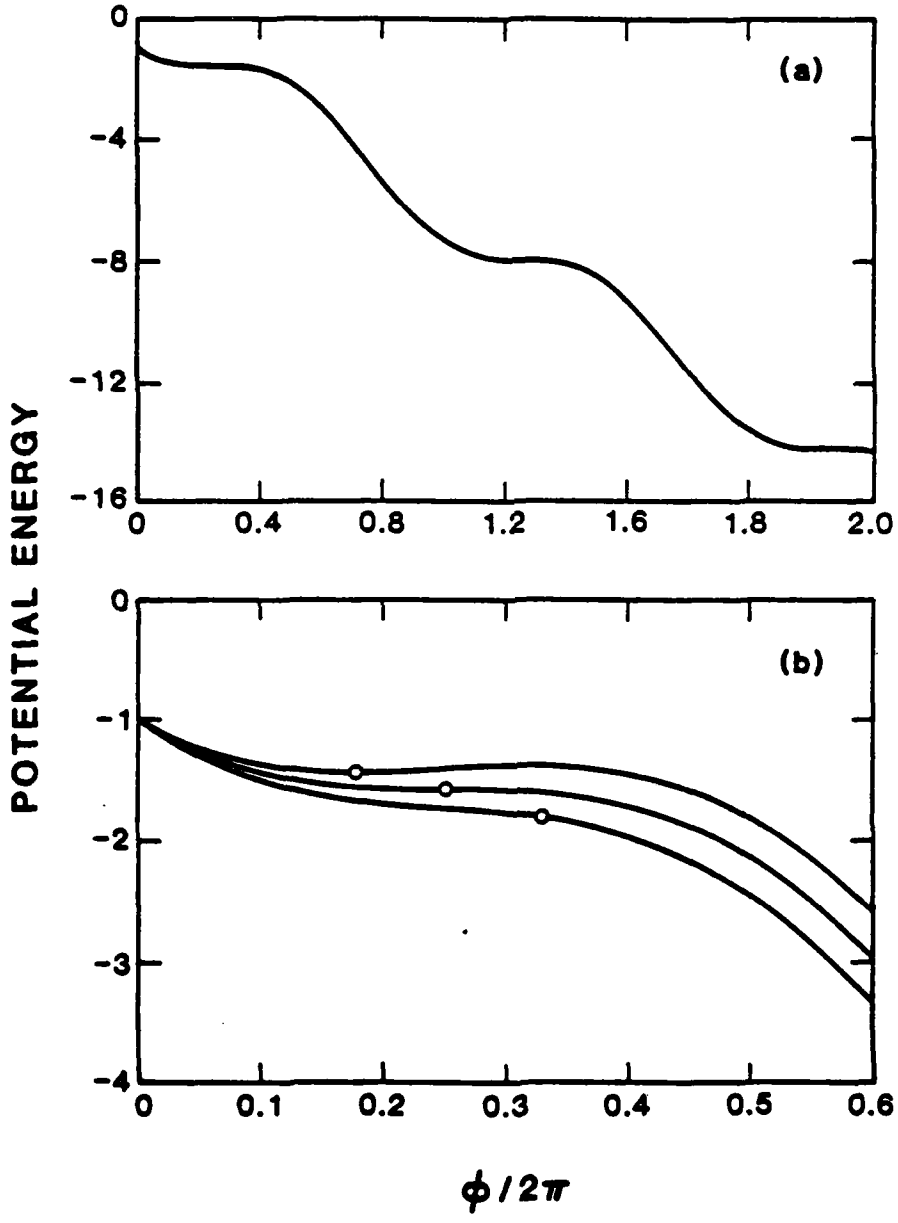
POTENTIAL ENERGY
(a)
0
-4
-8
-12
-16
0
0.4
0.8
1.2
1.6
1.8
2.0
(b)
0
-1
-2
-3
-4
0
0.1
0.2
0.3
0.4
0.5
0.6
φ/2π

Fig 8

fig 9

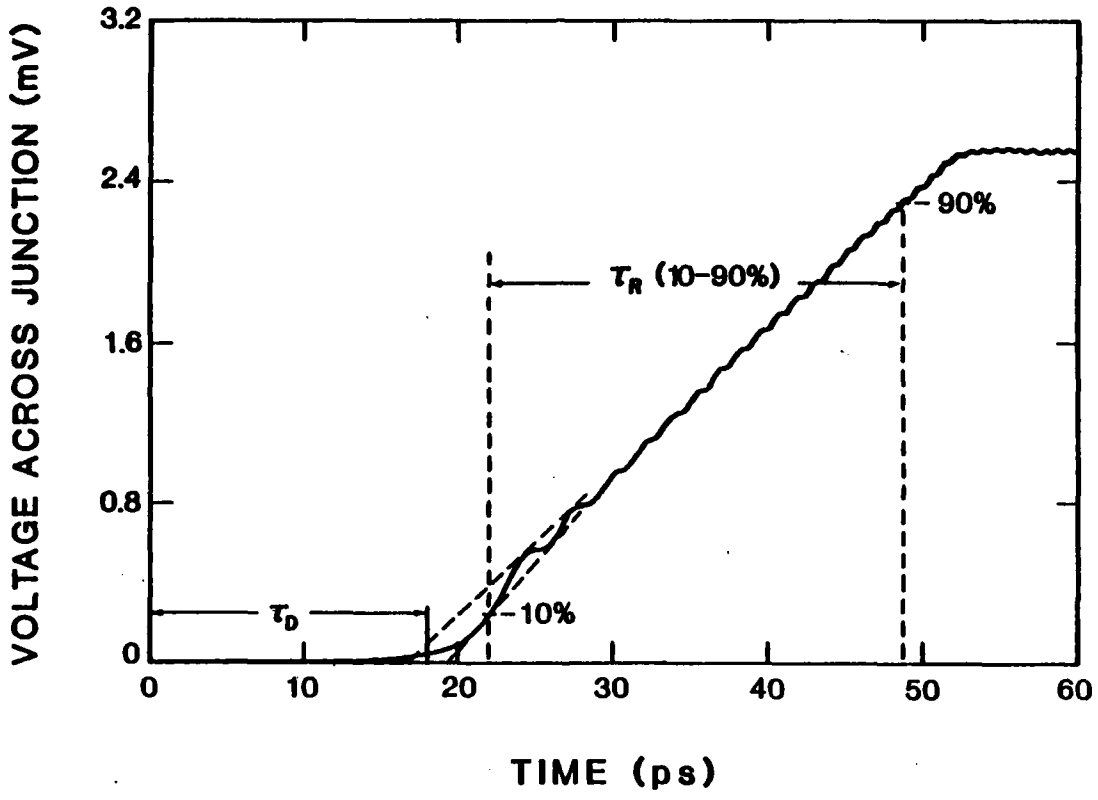
VOLTAGE ACROSS JUNCTION (mV)
3.2
2.4
1.6
0.8
0
0
10
20
30
40
50
60
TIME (ps)
τ_R (10–90%)
90%
τ_D
10%

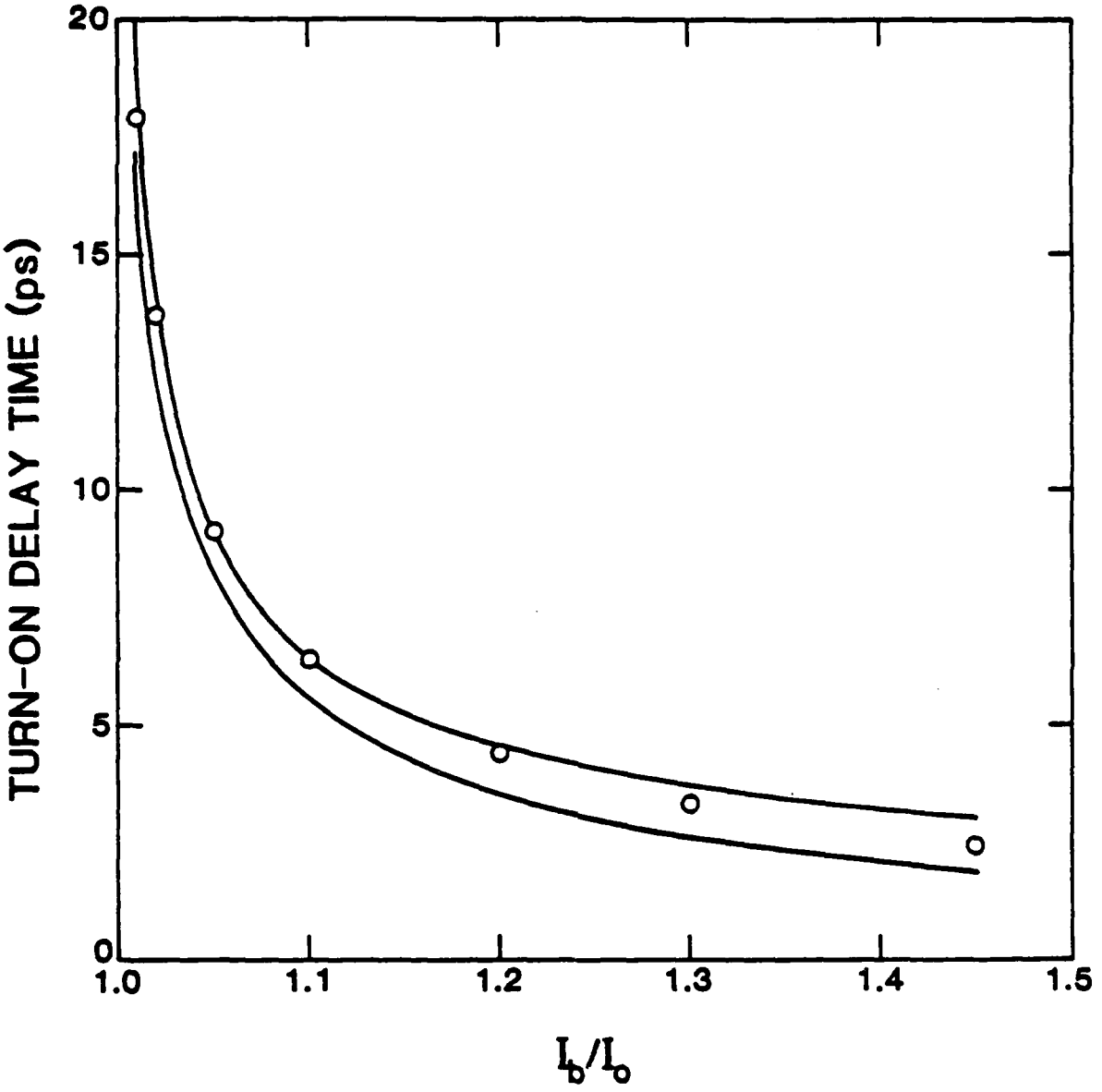

Fig 10

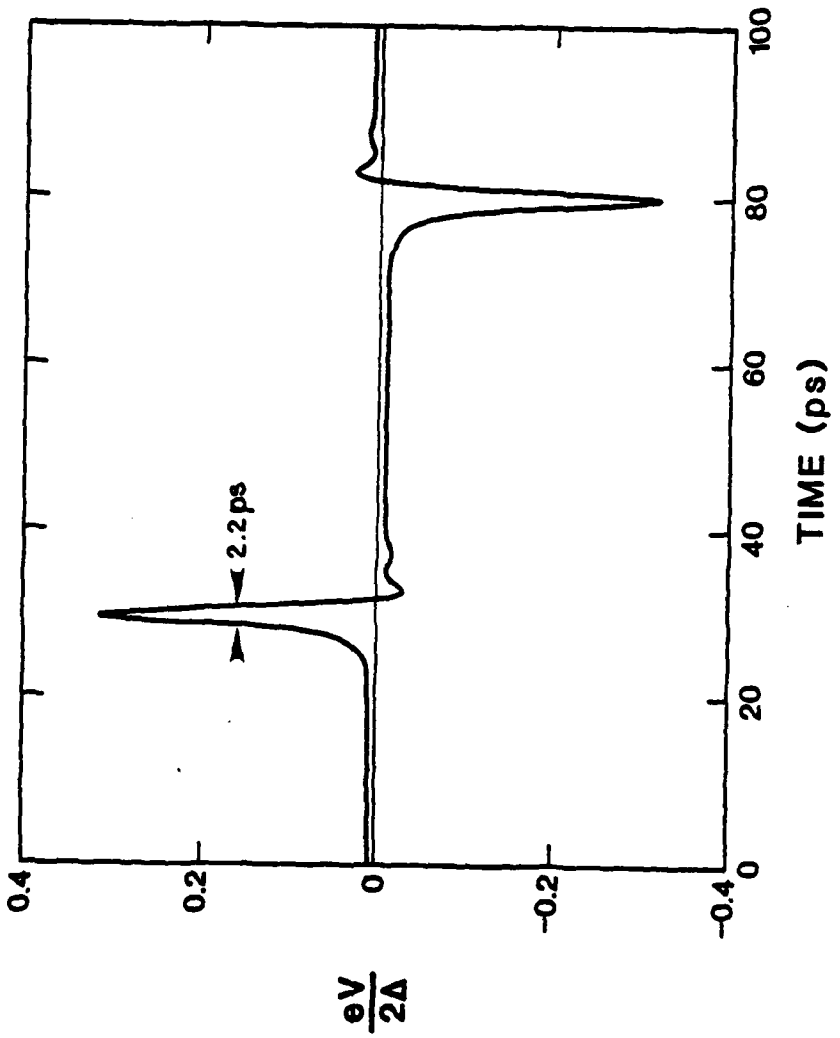

Fig 11

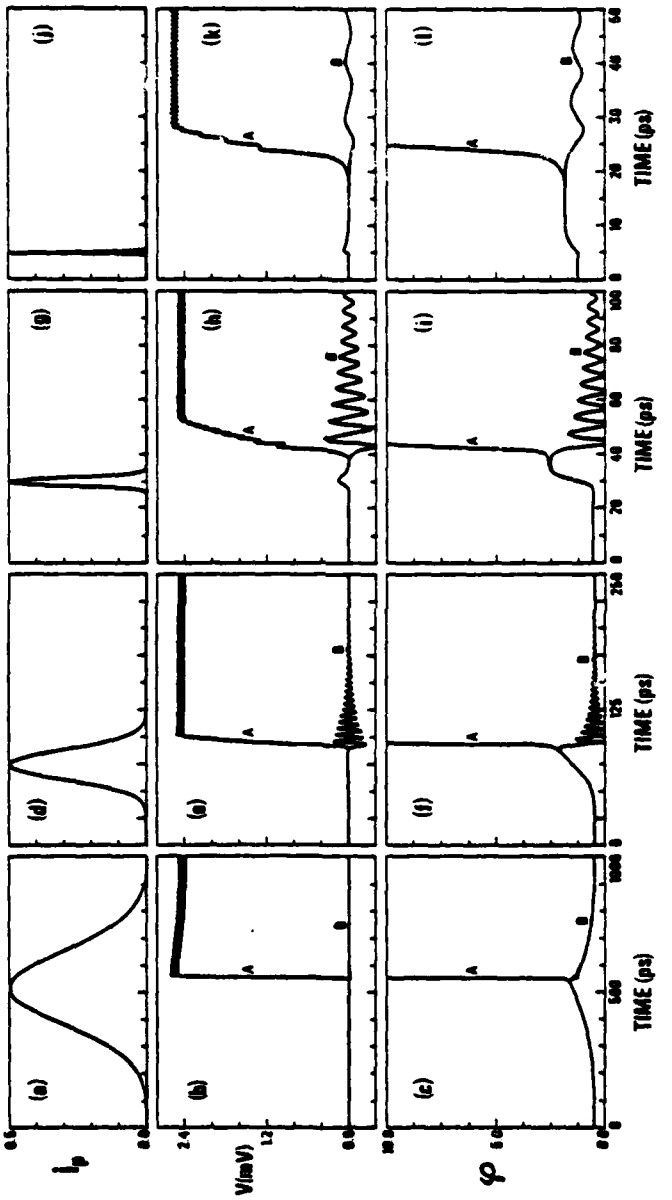

Fig 12

Fig 13

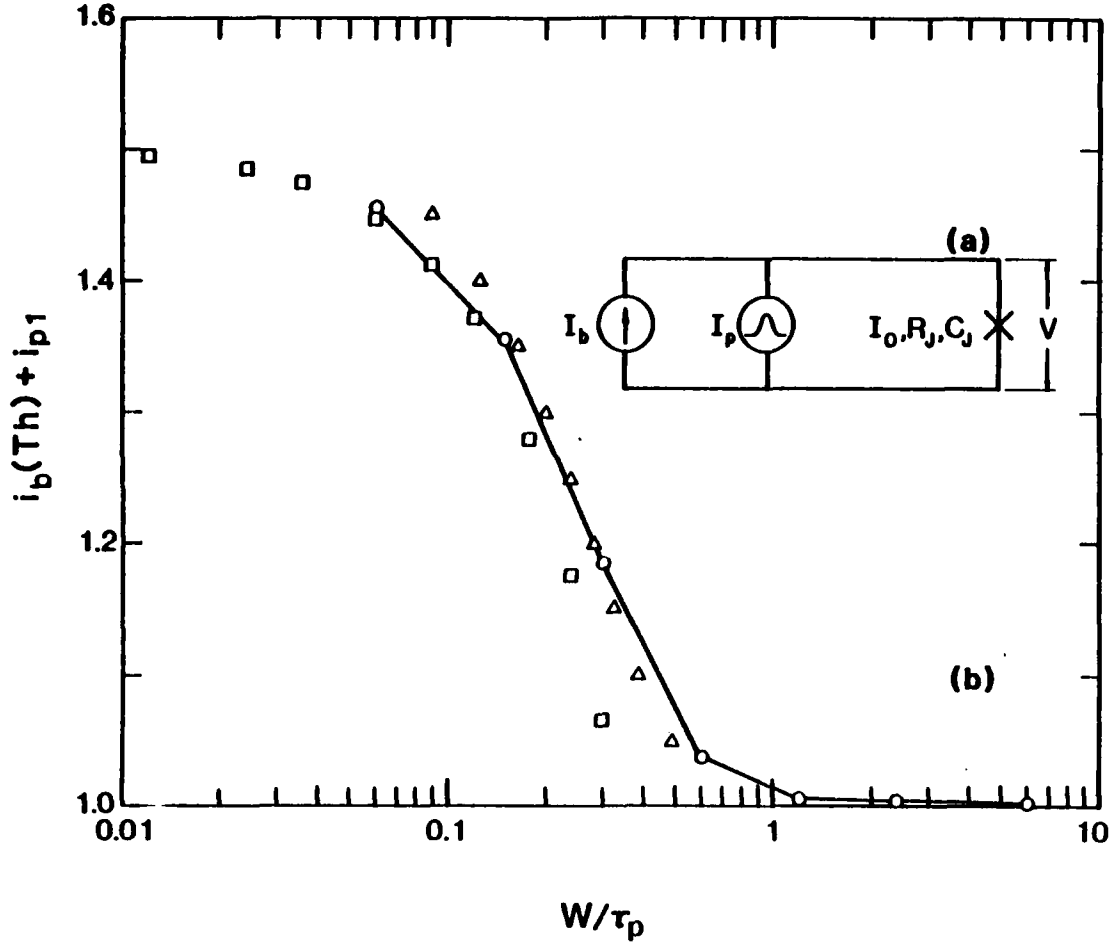

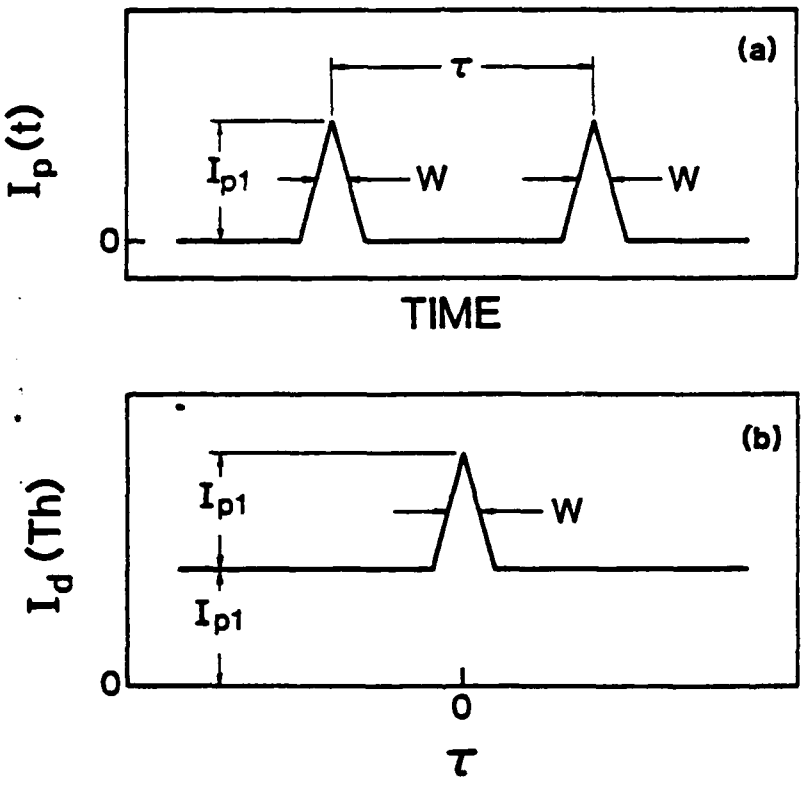

Fig 14

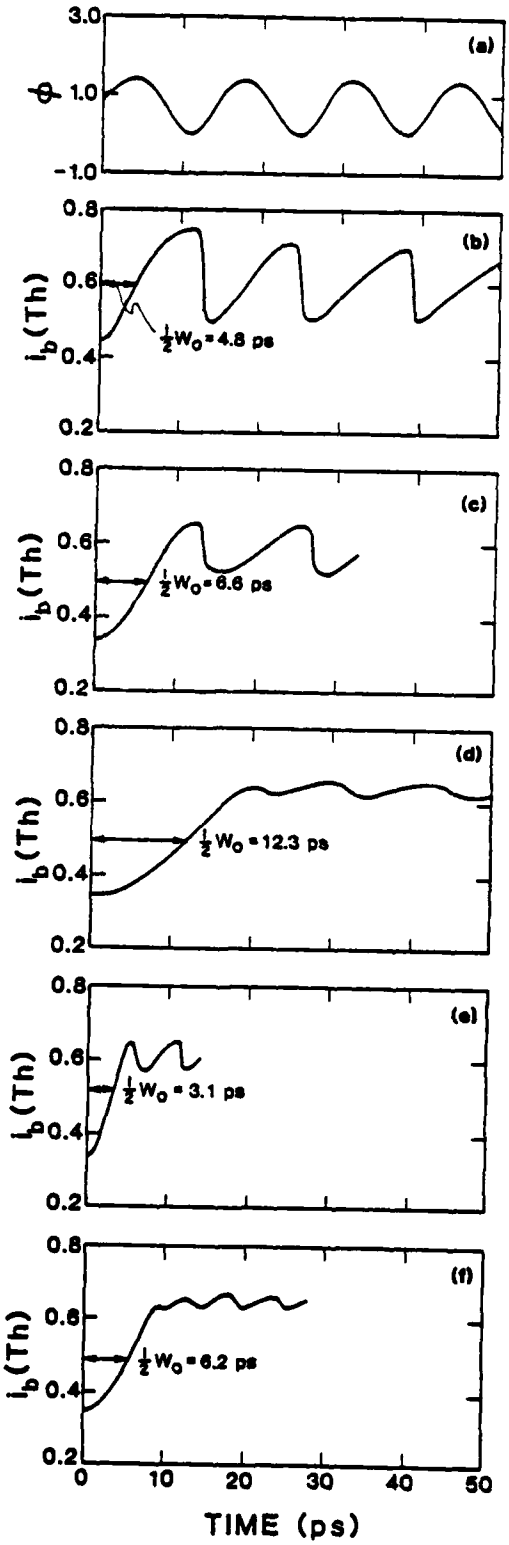
3.0
1.0
-1.0
ϕ
(a)
0.8
0.6
0.4
0.2
i_b(Th)
(b)
$\frac{1}{2}W_o$ = 4.8 ps
(c)
$\frac{1}{2}W_o$ = 6.6 ps
(d)
$\frac{1}{2}W_o$ = 12.3 ps
(e)
$\frac{1}{2}W_o$ = 3.1 ps
(f)
$\frac{1}{2}W_o$ = 6.2 ps
0
10
20
30
40
50
TIME (ps)

Fig 15

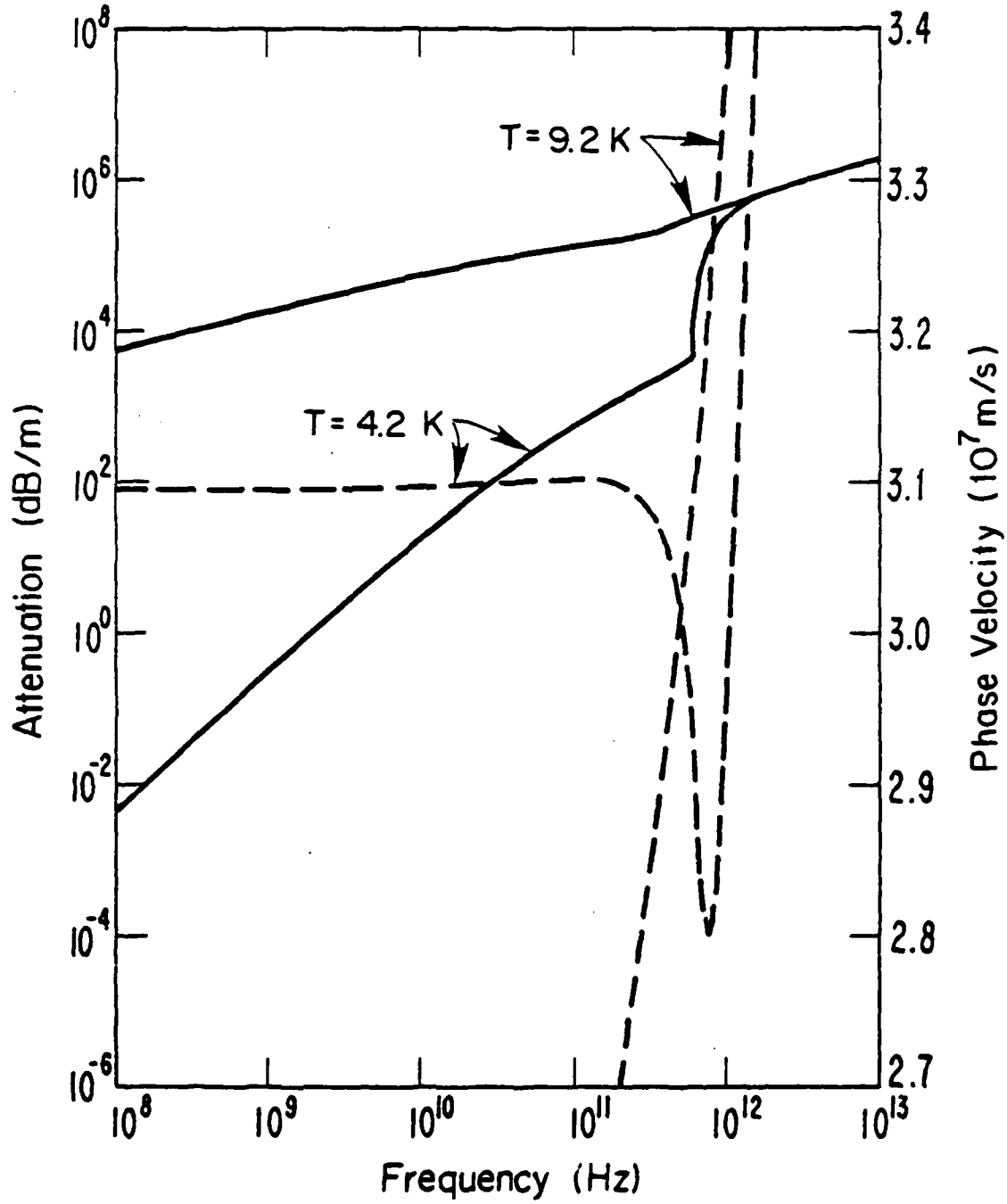
T = 9.2 K
T = 4.2 K
Attenuation (dB/m)
Phase Velocity (10^7 m/s)
Frequency (Hz)
10^8
10^6
10^4
10^2
10^0
10^{-2}
10^{-4}
10^{-6}
3.4
3.3
3.2
3.1
3.0
2.9
2.8
2.7
10^8
10^9
10^{10}
10^{11}
10^{12}
10^{13}

Fig 16

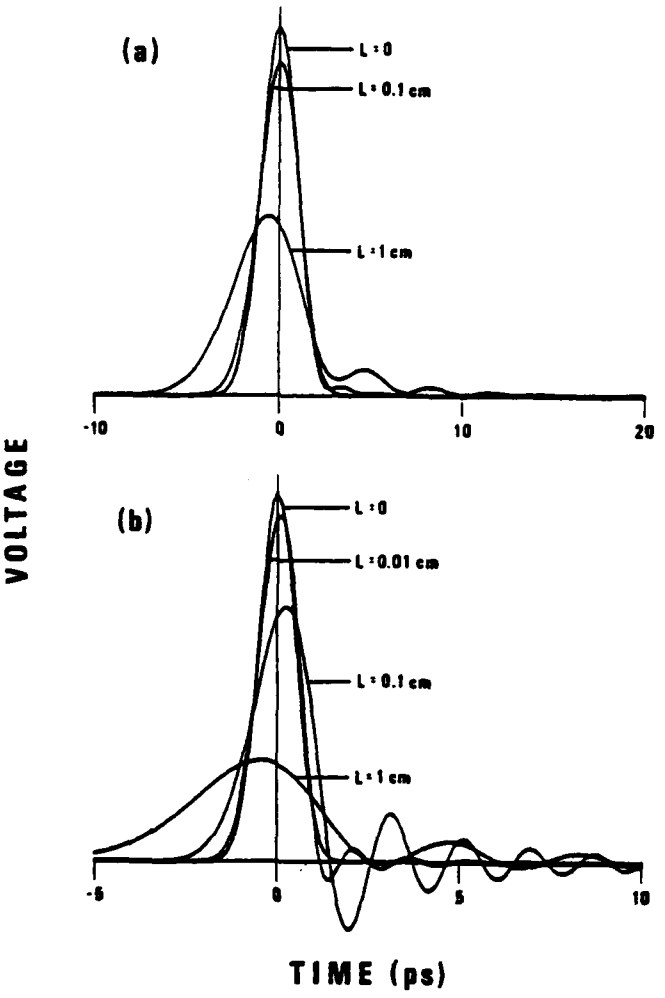
(a)
L = 0
L = 0.1 cm
L = 1 cm
-10
0
10
20
(b)
L = 0
L = 0.01 cm
L = 0.1 cm
L = 1 cm
-5
0
5
10
VOLTAGE
TIME (ps)

Fig 17

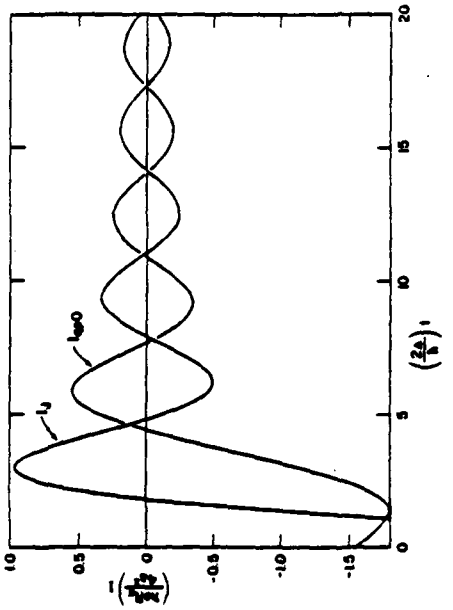
1.0
0.5
0
-0.5
-1.0
-1.5
0
5
10
15
20
$\left(\frac{2a}{\lambda}\right)_1$
J_1
J_{1e0}
$J_1\left(\frac{2a}{\lambda}\right)$

Fig 18

(a)

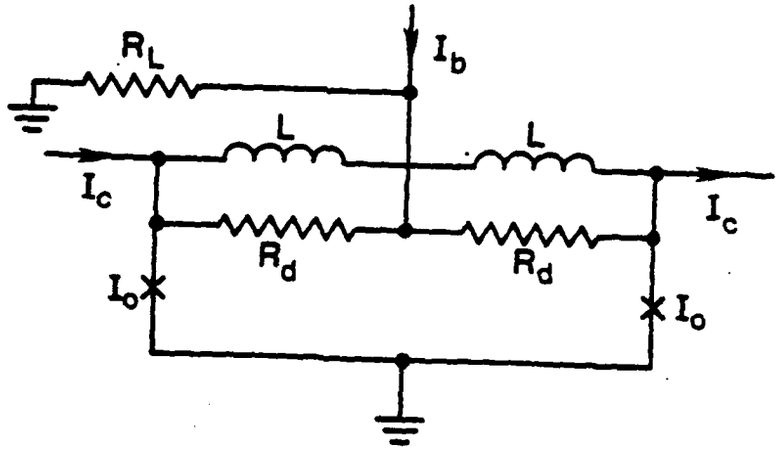

(b)

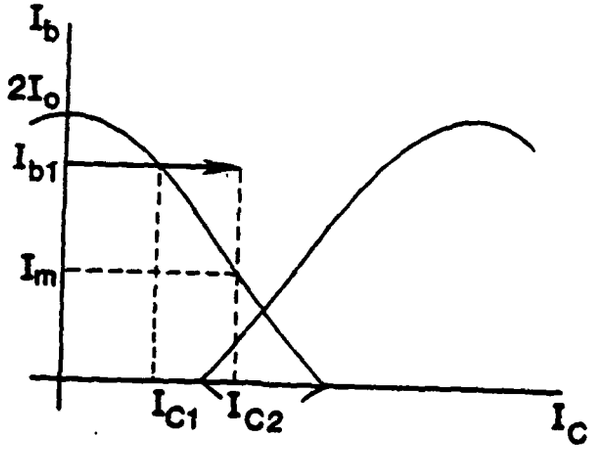

Fig 19.

Conversion gain in mm-wave quasiparticle heterodyne mixers

T.-M. Shen and P. L. Richards
Department of Physics, University of California, Berkeley, California 94720
R. E. Harris and F. L. Lloyd
National Bureau of Standards, Boulder, Colorado 80303

(Received 4 February 1980; accepted for publication 27 February 1980)

We report the observation of heterodyne mixing in superconductor-insulator-superconductor tunnel junctions with significant conversion gain and with a noise temperature comparable to the photon noise limit. (Double sideband $L^{-1} = 1.40 \pm 0.14$, $T_M \lesssim 1.5$ K at 36 GHz.) The mixing arises from the strong nonlinearity in the quasiparticle tunneling currents at voltages comparable to the full energy gap. Gain is observed when the onset of quasiparticle current is sufficiently sharp that quantum effects are important. The observed gain is in good quantitative agreement with calculations based on the work of Tucker. It should make possible the construction of photon-noise-limited microwave heterodyne receivers.

PACS numbers: 07.62. + s, 74.50. + r

Applications such as radio astronomy and space communications require coherent millimeter-wave receivers with noise temperatures that approach the photon noise limit $T_R = h\nu/k$. The largest double sideband (DSB) conversion efficiency possible[1] from a classical resistive mixer is $L^{-1} = 1.0$. Therefore both a very quiet mixer *and* a large improvement in intermediate frequency (IF) amplifier noise would be required to achieve this goal with a classical mixer. In this letter we report the first observation of quasiparticle mixing with significant conversion gain and the first microwave mixing experiment to reach the photon noise limit.

Mixing due to the quasiparticle currents in a superconductor-insulator-superconductor (SIS) tunnel junction[2,3] is not correctly described by classical theory when the corner on the quasiparticle I-V curve occurs within the voltage range $h\nu/e$. Evidence for photon-assisted tunneling, observed in the form of bumps separated by $h\nu/e$ on the bias voltage dependence of the IF signal,[2] shows the necessity of a quantum-mechanical treatment. Tucker has recently used the full quantum tunneling theory[4] to calculate the performance of an ideal SIS junction operated as a three-port mixer.[5] He predicts a new physical phenomenon of great technological importance: quiet mixing ($T_M \sim h\nu/k$) with large conversion gain. This prediction suggests that SIS quasiparticle heterodyne receivers can reach the photon noise limit.

Lead alloy SIS junctions are convenient for mixing experiments because of their immunity to thermal cycling and the availability of lithographic techniques for producing junctions with small areas. The onset of quasiparticle tunneling in these junctions, however, is usually smeared significantly over the voltage range of 0.15 mV which is equal to $h\nu/e$ at our operating frequency of 36 GHz. For our experiments we have used Pb–Bi (29 wt. % Bi) junctions processed to minimize this effect.[6] The resulting I-V curve for a typical $3 \times 3\,\mu$m junction with a normal resistance of 21 Ω is shown in Fig. 1(a).

Mixer experiments were carried out using a measurement system which was designed for the quantitative evaluation of mixer parameters,[2] rather than for use as a low-noise receiver. The junction was deposited on a $0.28 \times 1.0 \times 19$ mm Si strip which was placed in the E-field direction across a full-height KA-band microwave waveguide. An adjustable stub $\frac{1}{4}\lambda_g$ in front of the junction and a plunger behind it formed the low-temperature rf impedance matching struc-

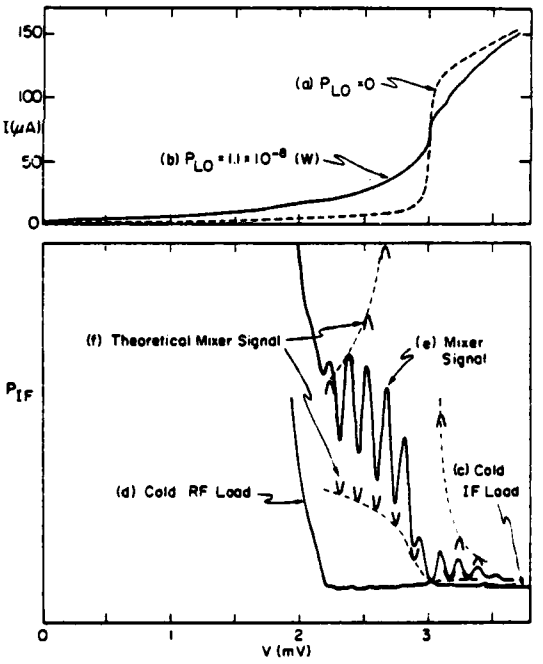

FIG. 1. Static I-V curves are shown in the upper plot for a junction at 1.5 K (a) without P_{LO} and (b) with P_{LO}. Plots of IF output power in the frequency range from 30 to 80 MHz are shown in the lower portion of the figure as a function of junction bias voltage. Point (c) was obtained with a 50-Ω 1.5-K load in place of the mixer, curve (d) with a matched 1.5-K load in front of the mixer, and curve (e) with a calibrated 36-GHz signal applied to the mixer from an oscillator. Values of mixer noise temperature were deduced from (c) and (d), and conversion efficiency from (e). Curve (f) shows the oscillations in the mixer output calculated from quantum three-port Y-mixer theory with no free parameter. Below ~2.1 mV Josephson (pair tunneling) currents degrade mixer performance. In this region the mixer has high conversion efficiency, but also large noise.

 0003-6951/80/090777-03$00.50

ture. Radio frequency leakage was minimized by the use of choke structures on the plunger, stub adjustment, and IF ports. Signal and LO power from carefully calibrated 36 GHz oscillators were combined in a 10-dB directional coupler and introduced into the cryostat through a section of stainless-steel waveguide. Noise from the oscillators and from room-temperature objects was reduced by the use of a 19.4-dB cold attenuator at the entrance to the mixer. The combined loss of the waveguide and the attenuator was deduced from measurements of their transmittance as a function of the height of the helium in the cryostat. Three identical 50-Ω stainless-steel IF cables were installed in the cryostat. One was terminated with a short circuit to measure IF cable loss, one was terminated in a 50-Ω cold load to provide a noise source for calibrating the IF amplifier train, and one was connected to the mixer. A directional coupler was used to inject a signal into the mixer output to evaluate its coupling to the IF system. Measurements were made in the IF frequency band of 30–80 MHz using a string of transistor amplifiers with $T_{IF} = 50$ K, followed by a spectrum analyzer.

The static I-V curve of a typical Pb–Bi junction is shown without LO drive in Fig. 1(a) and with the LO power, stub, and plunger settings which maximize the conversion efficiency in 1(b). Photon-assisted tunneling steps are weakly seen on the I-V curve measured with LO drive. These steps appear as very pronounced bumps on the plot of mixer signal versus bias voltage in Fig. 1(e). Measured parameters for mixers made from very similar junctions are given in Table I. The stub and plunger settings and the bias levels were chosen to maximize the mixer signal (and therefore the conversion efficiency). When the stub and plunger were adjusted in such a way that the conversion efficiency was the same in both sidebands, the overall single-sideband (SSB) conversion efficiency referred to the entrance of the mixer block was observed to be as large as $L^{-1} = 0.55 \pm 0.05$. When corrected for the IF cable transmittance (0.89), and the IF mismatch (0.90 ± 0.02), the best mixer conversion efficiency was estimated to be $L^{-1} = 0.70 \pm 0.07$ SSB or 1.40 ± 0.14 DSB. The observed values of L^{-1} are a factor ~ 4 larger than those previously measured in the same mixer mount with a junction that was operating close to the classical limit.[2] The obsevation of a DSB conversion efficiency greater than 1.0 is unambiguous evidence for conversion gain. Despite the low IF frequency, some image rejection could be obtained by operating with the stub close to the position at which its impedance is singular. Mixer conversion efficiencies as large as 0.91 (SSB) were observed in this mode of operation, as shown in Table I.

TABLE I. Properties of two SIS mixers with normal state resistances of 22 Ω, operated at 1.5 K. The noise temperatures and conversion efficiencies are referred to a single sideband. Values of conversion efficiency are given separately for upper (above) and lower (below) sidebands. The second listed mixer has been optimized for SSB performance. The experimental errors are given as 50% confidence limits.

P_{LO} (10^{-9} W)	L^{-1} (Overall experiment)	L^{-1} (Mixer experiment)	T_M (Experiment) (K)
12.2	$\begin{matrix}0.55\\0.55\end{matrix} \pm 0.05$	$\begin{matrix}0.70\\0.70\end{matrix} \pm 0.07$	<3
13.2	$\begin{matrix}0.40 \pm 0.04\\0.71 \pm 0.07\end{matrix}$	$\begin{matrix}0.51 \pm 0.05\\0.91 \pm 0.09\end{matrix}$	$\begin{matrix}<9\\<5\end{matrix}$

Because the nonlinearity of the I-V curve extends over a narrow range, small values of LO power are used, and the mixer can be saturated by relatively small amounts of signal power. For a signal of 3×10^{-11} W ($\simeq 0.3\%$ of P_{LO}) the IF power was 3% less than the value expected if there were no saturation. Measurements of mixer parameters were made with low enough power that saturation was not important. In a typical heterodyne application with a 1-GHz signal bandwidth B, the room-temperature noise $P = kTB = 4 \times 10^{-12}$ W would not be sufficient to saturate the mixer. Rectification (direct detection) of this noise would cause a very small (1 part in 10^4) change in the dc bias current.[7]

Because the onset of quasiparticle tunneling is still significantly rounded in the junctions used for our experiments, Tucker's idealized calculation of mixer properties is not directly applicable. We have extended the calculations so that the imaginary and real parts of the junction response are obtained from the measured static I-V curve and its Kramers-Kronig transform.[8] Predictions of conversion efficiency and noise as a function of bias voltage were then computed for a three-port Y-mixer model which assumes that all harmonic frequencies are shorted by the junction capacitance. One useful feature of our experiments is that the shape of the I-V curve measured with various values of LO power is quite sensitive to the setting of the stub and plunger. This effect was utilized to deduce the rf source impedance Z_s. The junction capacitance was regared as part of this source impedance. The value of $Z_s = 14.1 + j1.4\ \Omega$, determined by fitting the model to I-V curves measured with constant available LO power, was in good agreement with standard cavity theory and was used in the calculations of mixer performance. Some evidence for inadequacy of the three-port model was provided by this procedure. The quality of the fit was less good for the junctions used here than for other junctions with larger capacitance. The IF load impedance for our matched FET amplifier was 50 Ω (real).

The predictions of quantum three-port Y-mixer theory with no free parameters are shown in Fig. 1. The calculated mixer signal as a function of bias voltage with constant rf source impedance shows the same oscillations that appear in the experimental data. To avoid confusion, only parts of each oscillation are plotted as Fig. 1(f). The agreement with the experimental mixer output shown in Fig. 1(e) is very good where the experimental output is high, but diverges rapidly as the bias voltage approaches 3 mV. We can understand this striking result in terms of the rapidly increasing first-harmonic content of the LO waveform as the bias is increased toward 3 mV. In three-port Y-mixer theory these harmonics are rigorously shorted, and so do not degrade the conversion efficiency. In the experiment, the junction capacitance is not completely effective in shorting the harmonics, so a significant fraction of the signal power is converted to harmonic frequencies.

This interpretation is confirmed by preliminary five-port Y-mixer model calculations in which the junction is assumed to be terminated by its own capacitance at the first-harmonic frequency. The value of the reactive element, $(j2\omega C)^{-1} = -j5\ \Omega$, was determined by a second-order fitting to the experimental I-V curve with LO power. It is within a factor ~ 2 of the value estimated from the Josephson critical current density. Preliminary calculations using the five-port Y-mixer model indicate that the conversion efficiency for fundamental mixing is reduced from the prediction of the three-port model. The divergence in the conversion efficiency shown at ~ 2.8 mV in Fig. 1(f) is no longer predicted. The predictions of the five-port model are within a factor ~ 2 of the experimental coversion efficiency at all voltages. It appears likely from these results that the SIS junction will be a very efficient first-harmonic mixer if it is biased near the point of approximate symmetry of the I-V curve near 3 mV.

We have every reason to believe that the predicted gain mechansim has been observed and that larger gain can be obtained from junctions with sharper corners on their I-V curves, and/or from junctions operated at higher frequencies. Some insight into the conversion gain can be obtained if we observe that the conversion efficiency is proportional to the dynamic resistance of the junction with LO applied. Direct calculations using our three-port mixer model show that the large oscillations in L^{-1} arise primarily from the effects of the photon assisted tunneling steps on the dynamic resistance. In particular, gain occurs where the I-V curve is nearly horizontal so that this resistance is large. In the extreme quantum limit, regions of negative resistance are predicted which give infinite gain or oscillations. This association of conversion gain with rf-induced steps on the I-V curve is very similar to the situation previously observed in point-contact Josephson effect mixers.[9]

Because of the increase in conversion efficiency, it has been possible to improve on our previous measurements of SIS mixer noise temperature. The values given in Table I are much lower than the upper limits obtained previously using the same experimental techniques.[2] The lowest observed mixer noise $T_M < 1.5$ K (DSB) is equal to the photon noise limit $h\nu/k = 1.7$ K within the experimental uncertainty of approximately ± 2 K. The contribution to this noise from the LO has been computed from the quantum theory.[4,5] We obtain the value 1.4 K from the three-port Y-mixer model for the mixer shown in Fig. 1.

We are grateful to J.R. Tucker for showing us his calculations prior to publication. A portion of this research was supported by the U.S. Office of Naval Research.

[1]H.C. Torry and C.A. Whitmer, *Crystal Rectifiers*, MIT Radiat. Lab. Ser. Vol. 15 (McGraw-Hill, New York, 1948), pp. 130–135, 406–415.
[2]P.L. Richards, T.M. Shen, R.E. Harris, and F.L. Lloyd, Appl. Phys. Lett. **34**, 345 (1979).
[3]G.J. Dolan, T.G. Phillips, and D.P. Woody, Appl. Phys. Lett. **34**, 347 (1979).
[4]J.R. Tucker, IEEE J. Quantum Electron. **QE-15**, 1234 (1979).
[5]J.R. Tucker, Appl. Phys. Lett. **36**, 477 (1980).
[6]J.H. Greiner, C.J. Kircher, and I. Ames, IBM J. Res. Dev. (to be published).
[7]P.L. Richards, T.-M. Shen, R.E. Harris, and F.L. Lloyd, Appl. Phys. Lett. **36**, 480 (1980).
[8]R.E. Harris, Phys. Rev. B **10**, 84 (1974); **11**, 3329 (1975).
[9]Y. Taur, J.H. Claassen, and P.L. Richards, Appl. Phys. Lett. **24**, 101 (1974).

Large growth-induced anisotropy to preferential occupation of the iron sites in garnets

L. C. Luther, R. C. LeCraw, E. M. Gyorgy, and S. L. Blank
Bell Laboratories, Murray Hill, New Jersey 07974

(Received 26 December 1979; accepted for publication 26 February 1980)

Large growth-induced anisotropies (K_u) arising from the preferential occupation of Ir^{4+} on octahedral sites have been measured. For YIG with approximately 0.2 Ir atoms per garnet formula unit and Mg^{2+} as a charge compensator, values of $K_u = +4.5 \times 10^5$ ergs/cm^3 have been obtained. The induced anisotropy is proportional to the Ir^{4+} present as deduced from the optical absorption.

PACS numbers: 61.50.Cj

Preferential occupation of the rare earths on dodecahedral sites is well known to produce a uniaxial (actually orthorhombic) anisotropy in iron garnets. In fact, most of the bubble technology depends on this mechanism. In this letter we report on the preferential occupation of 4*d* and 5*d* ions on the iron (octahedral and tetrahedral) sites. With Ir^{4+} and Mg^{2+} substituted for Fe^{3+} in YIG we have obtained a growth-induced uniaxial anisotropy as large as 4.5×10^5 ergs/cm^3 for (111) films. This may be compared with 3×10^5 ergs/cm^3, the largest growth-induced K_u reported thus far for the garnets.[1] The composition of this garnet was $Sm_{1.2}Lu_{1.8}Fe_5O_{12}$.

 0003-6951/80/090779-03$00.50

A superconducting sampler for Josephson logic circuits

C. A. Hamilton, F. L. Lloyd, R. L. Peterson, and J. R. Andrews
Electromagnetic Technology Division, National Bureau of Standards, Boulder, Colorado 80303

(Received 9 July 1979; accepted for publication 20 August 1979)

A method is described for automating a technique which is used to sample transition duration (rise time) in superconducting logic circuits. The method is based on measuring the time at which a biased Josephson junction switches under the influence of an applied signal. The system transition duration is limited primarily by time jitter which is estimated to be 7 ps. Transition durations of as little as 9 ps have been observed.

PACS numbers: 74.50. + r

The characterization of Josephson logic circuits often requires the measurement of very fast low-level signals. Such measurements are difficult to perform because of the loss of bandwidth for signal transmission to room temperature. Also, standard sampling oscilloscopes have transition durations (rise time) of about 20 ps whereas high current density Josephson devices switch in times less than 10 ps. It is therefore desirable to provide for high-speed measurements directly on the superconducting logic chip. This may be accomplished by using a biased Josephson detector as an amplitude discriminator for the signal to be measured.[1,2] This detector will switch to the voltage state when the signal plus the bias exceed the detector critical current. Since the bias and the critical current are known, the signal level at the time the detector switches can be determined. Thus, by measuring the delay in the detector output as a function of bias, rising edges on the signal may be mapped out. This has commonly been done[1,2] by recording traces of the detector output for a number of values of bias. The signal may then be computed point by point. This method is somewhat tedious and may yield erroneous results if the time base used drifts during the measurements. Since time-base drift may be as much as several ps/min, it is a serious problem for ultrafast measurements.

Typical sampling oscilloscopes used to record the detector waveform have an external time-base input which may be used to specify the sampling time. By driving this input from the sampled voltage, the sampling time can be locked to the steepest portion of the detector output waveform. The time-base input, therefore, is a measure of the detector switching time. The signal waveform is thus reproduced by sweeping the bias and recording the bias versus the time-base input. This method yields the signal waveform directly and in a time short enough to minimize drift problems.

Figure 1 shows in more detail how this is accomplished. The superconducting integrated circuit is shown in the dashed box. It consists of a first junction $J1$ which serves to produce a very fast signal transition which is then sampled by the second detector junction $J2$. The sequence is as follows: a tunnel diode step generator operating at 60 kHz applies a repetitive 200-ps transition duration step to junction $J1$. When its critical current I_{c1} is exceeded, $J1$ switches to its energy gap (2.5 mV) in a time determined primarily by its critical current and capacitance. This applies a signal current I_s through the 8-Ω resistor to junction $J2$. $J2$ will switch when the current I_s plus the bias current I_b exceeds I_{c2}. The output of $J2$ is transmitted to room temperature and sampled at time t. The sampled voltage is compared with a reference level, typically 1 mV, by applying the reference as an offset voltage to the sampling head amplifier. The difference signal from the sampling head amplifier is integrated by inverting amplifier A1 and used to drive the sampling time base input. Thus, if the sampled voltage is below the reference level, the integrator output increases, advancing the sampling time to the point where the signal equals the reference. If the sampled voltage is greater than the reference, the sampling time is decreased in the same way. This servo loop thus causes the sampling time to lock to the point at which the rising edge of the $J2$ transition crosses the reference level. The time base input is therefore a measure of the time at which $J2$ switches, i.e., the time at which I_s equals $I_{c2} - I_b$. As I_b is slowly swept by the ramp generator ($\sim$30-s sweep time), the X-Y recorder, which plots $-I_b$ versus sampling time, will trace out the rising portion of the transition in I_{c2}. Since the sampling rate (60 kHz) is much greater than the servo loop frequency response, noise and time jitter in the sampling system are averaged. The 600-ps delay line on the IC chip provides isolation to separate the $J2$ transition from cross talk between input and output lines at the chip mount. The timing network and analog switch pull the bias to zero between samples to reset the junctions to the zero voltage state.

The advantage of this method lies in the fact that it can measure transition durations which are substantially faster than the transition duration of either the chip mount ($\sim$50 ps) or the sampling scope ($\sim$20 ps). The measurable transi-

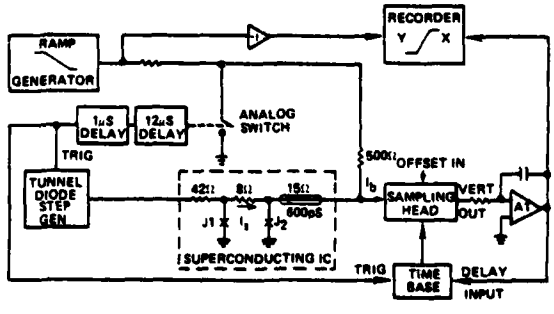

FIG. 1. Block diagram of the transition duration measurement system utilizing a Josephson junction as an amplitude discriminator.

 0003-6951/79/210718-02$00.50

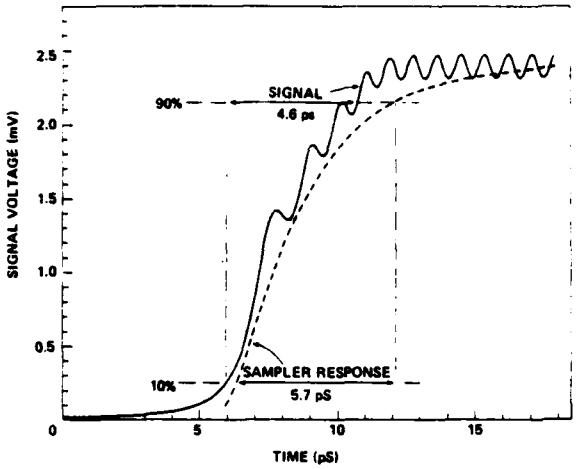

FIG. 2. Simulation of the signal voltage waveform (solid curve) and its reconstruction (dashed curve) based on the use of a second junction as a sampling device. The time scale of the reconstructed curve has been arbitrarily shifted to bring the two curves together. The simulation parameters are $I_{c1} = 2.9$ mA, $C_1 = 4.8$ pF, $I_{c2} = 1.45$ mA, $C_2 = 2.4$ pF. The input is a 1-mV/ps ramp.

tion duration is limited primarily by the jitter in the sampling system. The accuracy of the recorded waveform is also subject to the assumption that the detector junction waveform is constant and that its delay depends only on the instant at which its critical current is exceeded. These assumptions will break down at sufficiently high speeds. The most significant error results from the fact that the turn-on delay[3] of $J2$ is a function of overdrive. Thus for low bias values (signal near maximum), the $J2$ transition has some additional delay. This has the effect of making the recorded waveform slightly slower than the actual signal.

Figure 2 is the result of a simulation of our circuit. The solid curve is the computed signal voltage produced by $J1$. The dashed curve is the computed result which the above described method would produce in the absence of jitter. The error caused by variable turn-on delay is evident in the increased separation of the two curves near the signal maximum. The fine structure caused by Josephson oscillations is also washed out. The critical current density of both junctions is 4200 A/cm^2, giving them an estimated $R_N C$ time of

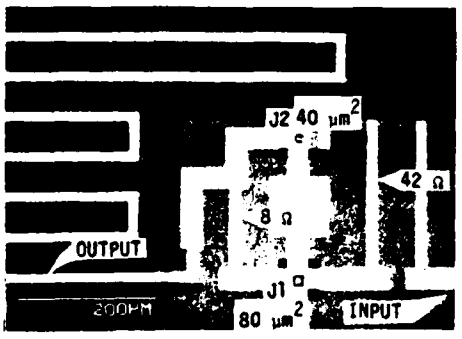

FIG. 3. Photograph of the superconducting integrated circuit.

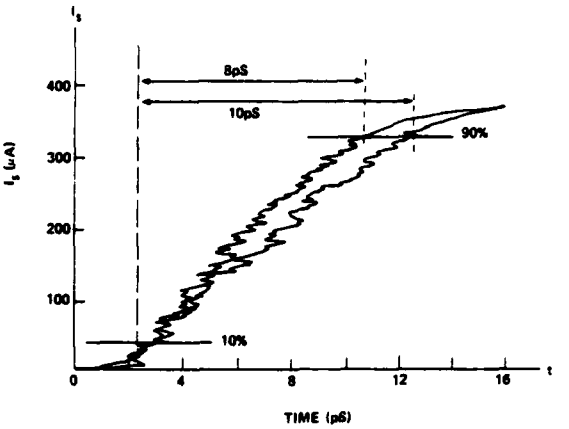

FIG. 4. Recorded transition duration of the signal current I_s for a junction with critical current density of 4200 A/cm^2.

2 ps (R_N is the junction normal state resistance).[4] The effect of jitter is roughly equivalent to passing the signal through a low-pass filter of rise time equal to the jitter width.

Figure 3 is a photograph of the integrated circuit used in this experiment. It is a seven-level circuit which uses a lead alloy process similar to that described in Ref. 5. The junction areas are approximately 40 and 80 μm^2 as indicated. The microstripline showing at the left is a small portion of the line used to obtain 600 ps of delay in the output signal. The parameters used in the simulation of Fig. 2 are taken from measurements on this circuit.

Figure 4 is the experimental transition duration data recorded for this circuit. The two traces, recorded about one minute apart, are for increasing and decreasing bias. They are different because the sampling time drift decreases the apparent transition duration in one case and increases it in the other. Assuming constant drift, the correct transition duration (10%–90%) will be the average, or about 9 ps. This result represents the combination of the signal transition duration estimated to be about 5 ps and the jitter limited system response of about 7 ps.

A second experiment was performed in which the switching transition of $J1$ was intentionally rolled off by an on-chip RC filter. In this case the recorded waveform was the expected exponential rise. The time constant (3.7 ns) matched the filter to the accuracy with which the filter components were known (30%).

It is important to note that the very fast switching speed reported here is only one part of the delay which occurs in logic circuits. Gheewala[6] has used a chain of gates to measure logic delays of as little as 13 ps.

This work is supported by the Office of Naval Research under Contract No. N00014-79-F-0020.

[1]Hans H. Zappe, IEEE J. Solid State Circuits, SC-10, 12–19 (1975).
[2]D.J. Herrell, IEEE Trans-Magn. MAG-10, 864–867 (1974).
[3]E.P. Harris, IEEE Trans-Magn. MAG-15, 562 (1979).
[4]This RC time is accurate to about a factor of 2 and was taken from R.E. Harris and C.A. Hamilton, AIP Conf. Proc. 44, 448–458 (1978).
[5]J. Greiner, S. Basavaiah, and I. Ames, J. Vac. Sci. Technol. 11, 81–84 (1974).
[6]T.R. Gheewala, Appl. Phys. Lett. 34, 670 (1979).

DISTRIBUTION LIST

FOR

TECHNICAL REPORTS

CONTRACT NUMBER N00014-80-0017[illegible]

	ADDRESSEE	NUMBER OF COPIES
1.	Office of Naval Research, Code 427 800 North Quincy Street Arlington, Virginia 22217	4
2.	Office of Naval Research Branch Office 1030 East Green Street Pasadena, California 91106	1
3.	The Aerospace Corporation Post Office Box 92957 Los Angeles, California 90009 Attn: A. Silver	1
4.	IBM Corporation 18100 Frederick Pike Gaithersburg, Maryland 20760 Attn: B. Troutman	1
5.	TRW Defense Space Systems Group One Space Park Redondo Beach, California 90278 Attn: D. Claxton	1
6.	University of California Electronics Research Laboratory Berkeley, California 94720 Attn: T. Van Duzer	1
7.	Naval Research Laboratory, Code 2026 4555 Overlook Avenue, S. W. Washington, D. C. 20375	1
8.	Naval Research Laboratory, Code 6854 4555 Overlook Avenue, S. W. Washington, D. C. 20375	1
9.	Data Acquisition Research Tektronix P. O. Box 500 Beaverton, Oregon 97077 Attn: Jon Birck	1

10. University of California — 1
Lawrence Livermore Laboratory
Livermore, California 94550
Attn: Joe Balch

11. Hewlett-Packard — 1
1501 Page Mill Road
Palo Alto, California 94304
Attn: Tom Hornak

12. Texas Instruments, Inc. — 1
P. O. Box 5936
Dallas, Texas 75222
Attn: William Wiseman

13. National Bureau of Standards — 4
Boulder, Colorado 80303
Attn: D. Sullivan

14. Defense Documentation Center — 12
Cameron Station Bldg. 5
Alexandria, Virginia 22314

15. A. G. E. D. — 1
9th Floor
201 Varick Street
New York, New York 10014

16. Office of Naval Research, Code 6854 — 1
800 North Quincy Street
Arlington, Virginia 22217